UNIVERSITÀ DEGLI STUDI DI TORINO

FACOLTÀ DI SCIENZE MATEMATICHE, FISICHE E NATURALI
CORSO DI LAUREA MAGISTRALE IN FISICA

Tesi di Laurea Magistrale in Fisica

STUDY OF THE NOISE IN THE ELECTROMAGNETIC CALORIMETER

AND

ANALYSIS OF THE INVARIANT MASS SPECTRUM OF THE $\Upsilon(nS)\gamma$

IN THE CMS EXPERIMENT AT LHC

Candidato: Federica Tarsitano

Relatore: Dott. Stefano Argirò
Correlatrice: Dott.ssa Maria Margherita Obertino
Controrelatore: Prof. Ezio Menichetti

Anno Accademico 2013/2014

Federica Tarsitano: *Study of the noise in the Electromagnetic Calorimeter and Analysis of the invariant mass spectrum of the* $\Upsilon(nS)\gamma$ *in the CMS Experiment at LHC,* © July 2014

[..]purpureus veluti cum flos succisus aratro
languescit moriens lassove papavera collo
demisere caput, pluvia cum forte gravantur.

— Virgilio, Eneide - Libro IX - vv. 435-437

Dedicated to the loving memory of Sonia Nastri.

1990 – 2009

ABSTRACT

The CMS experiment at LHC features a general-purpose high performance detector designed to fulfil a physics program of wide scope.

Two analyses are here described: the first part refers to the study of the noise in the Electromagnetic Calorimeter (ECAL), while the second part, focused on Quarkonium physics, reports a study of the radiative decay of bottomonium, aimed in particular at the measurement of the mass of the $\chi_b(3P)$ state.

The estimation of the noise in ECAL has been obtained by analyzing the fluctuations of the signal in the circa 70000 scintillating crystals of which the detector is composed. The study of the noise and of its behaviour in time is essential for the future operation of the detector and it is functional to the determination of the thresholds for one of the calibration method being used to equalise the response of the channels. This method is called the $\phi - simmetry$ method, and it is based on the assumptions that channels placed at the same pseudorapidity receive equal fluxes of particles.

Radiative decays of bottomonium are studied by detecting $\Upsilon(nS) + \gamma$ final states, where n=1,2.. The study is aimed at the precise measurement of the mass of the last addition to the bottomonium spectrum, the $\chi_b(3P)$, discovered by the ATLAS experiment in 2012. Photons are detected using conversions in the CMS silicon tracker detector, which allows excellent energy resolution. A simultaneous fit to the $\Upsilon(1S) + \gamma$ and $\Upsilon(2S) + \gamma$ spectrum has been performed. Furthermore, during the optimization of the fit to the $\Upsilon(1S) + \gamma$ spectrum, an excess around a mass value of 10.08 GeV has been observed. In summary the analysis improved the knowledge of the recently discovered $\chi_b(3P)$ and revealed a possible new interesting component in the bottomonium spectrum.

"O frati," dissi, "che per cento milia
perigli siete giunti a l'occidente,
a questa tanto picciola vigilia

d'i nostri sensi ch'è del rimanente
non vogliate negar l'esperïenza,
di retro al sol, del mondo sanza gente.

Considerate la vostra semenza:
fatti non foste a viver come bruti,
ma per seguir virtute e canoscenza".

Dante Alighieri, La Divina Commedia,
Inferno, Canto XXVI - vv. 112-120

ACKNOWLEDGMENTS

I would like to thank all people who helped me during my studies and my thesis work, each of them was inspirational, supportive and patient.

Thanks to my supervisor, Stefano Argirò, for guide the direction of the work with careful and instructive comments.

My sincere thanks also goes to Margherita Obertino, who provided encouraging and constructive feedback.

I would like to express my heartfelt gratitude to Professor Ezio Menichetti, whose expertise, understanding and patience added considerably to my course and graduate experience.

I would also like to thank Nadia Pastrone, for welcoming me in the CMS Torino Group and always been extremely supportive.

I must acknowledge all my friends in CMS Torino group, for being there to listen and giving precious support and suggestions. In particular thank you to Umberto Tamponi, Alessandro Degano, Giacomo Ortona, Luca Pacher, Stefano Casasso, Gian Luca Pinna Angioni.

A special thanks goes to professors who didn't follow my thesis work, but were inspirational during my University courses: thank you to Prof. Mauro Anselmino and to Prof. Massimo Masera.

And last, but not least, to my family, thank you for love end for constantly supporting me.

CONTENTS

LIST OF FIGURES

LIST OF TABLES

ACRONYMS

CERN Conseil Européen pour la Recherche Nucléaire
LHC Large Hadron Collider
CMS Compact Muon Solenoid
ALICE A Large Hadron Collider Experiment
ATLAS A Toroidal LHC Apparatus
LHCb Large Hadron Collider beauty
ECAL Electromagnetic CALorimeter
HCAL Hadron CALorimeter

Part I

INTRODUCTION

1

INTRODUCTION

The Compact Muon Solenoid (CMS) Experiment at LHC is a general-purpose detector, conceived for the conduction of studies and researches in various and several fields in physics. Its experimental device, designed to detect p-p collisions at a center-of-mass energy of 14 TeV, is formed by detectors organized in a multi-layers configuration, typical of the collider experiments.

The main purposes of the CMS Experiment include the studies of the properties of the Higgs Boson and the search for new physics beyond the Standard Model, such as supersymmetry and extradimensions. Optimizing the operations of the detectors means recreating the conditions to make precise measurements and extend the actual studies to other fields.
In this thesis work two aspects are presented: the first concerns the study of the noise in the Electromagnetic Calorimeter, in order to support the calibration procedure with the ϕ-*symmetry* method; the second is related to the possibility of extending the researches to the Heavy-Flavours Physics, focusing particular attention to the bottomonium spectroscopy, thanks to the excellent performances of the CMS Silicon Tracker and the Muon Chambers.

The Electromagnetic Calorimeter, composed of about 70000 lead-tungstate ($PbWO_4$) crystals, is a fast detector, with high granularity and a good rediation hardness. The granularity of ECAL is geometrically organized in a configuration which provides for the identification of each crystal or channel with a pair of coordinates (η, ϕ); in Ecal Barrel, for example, groups of 360 crystals are schematically contained in a ring, identified by the coordinate η which runs from 1 to 85 in each side of the calorimeter, while ϕ runs from 1 to 360. The estimation of the noise and its temporal evolution are obtained through the analysis of the signal coming from the single channels. This study is essential for the near future operations on the detector and it is particularly related to the determination of the energy thresholds for the ϕ-symmetry calibration method, based on the assumption that all the crystals sited at the same pseudrapidity receive an equal flux of particles.

Studies about quarkonium states can produce useful indications about the models describing the production of the heavy-flavours, such as the Color Singlet Model (CSM) and the Non Relativistic QCD

(NRQCD). Quarkonium states can be also studied using phenomenological models and classified, similarly to the hydrogen atom, according to spectroscopical properties: the radial quantum number (n), the eigenvalue of the radial angular momentum (L), the eigenvalue of the spin (S) and the total angular momentum quantum number (J).
Particular attention is oriented to the $\chi_b(3P)$, discovered by the ATLAS experiment in 2012: it is a triplet of states $\chi_{bj}(3P)$, where j=0,1,2 and the third radial excitation of the P-wave triplet formed by the $\chi_b(nP)$, where n=1,2,3. The $\chi_b(3P)$ is reconstructed through its radiative decays $\chi_b(3P) \to \Upsilon(1S)\gamma$ and $\chi_b(3P) \to \Upsilon(2S)\gamma$, where $\Upsilon(kS) \to \mu^+\mu^-$, with k=1,2. The photon from the radiative decay is identified through e^+e^- conversions in the Beam Pipe and in Silicon Tracker, more advisable than the reconstruction through calorimetric measurements thanks to the excellent spatial resolution offered by the CMS tracker.
The determination of the mass of the $\chi_b(3P)$ is obtained with a simultaneous fit to the invariant mass spectrum of the $\Upsilon(1S)\gamma$ and $\Upsilon(2S)\gamma$: from this procedure rises that the measure can be done with a resolution which is better than the one obtained by the ATLAS and the LHCb experiments.
To obtain the best S/B ratio the simultaneous fit is realized after the optimization of the single fits to the Υ(1S) and Υ(2S): this strategy allows the observation of an excess of invariant mass around 10.08 GeV, whose nature is still object of investigation.

The presented double analysis represents a test of the performance of the CMS detector and also offers an experimental way to confirm and eventually extend the actual knownledge concerning the bottomonium spectrum.

Part II

THE LARGE HADRON COLLIDER AND THE CMS EXPERIMENT AT CERN

2

THE LARGE HADRON COLLIDER AT CERN

The Large Hadron Collider (LHC) is the world's largest and most powerful particle accelerator. It first started up on 10 September 2008, and remains the latest addition to CERN's accelerator complex. The LHC consists of a 27 km ring of superconducting magnets with a number of accelerating structures to boost the energy of the particles along the way. It accelerates and collides protons, and also heavy lead ions. Inside the accelerator, two high-energy particle beams travel in opposite directions in separated ultrahigh vacuum beam pipes and are guided around the rings by a strong magnetic field maintained by superconducting electromagnets. The beams are made to collide at four points where the two rings of the machine intersect; these four locations host the detectors of the main experiments at LHC: ATLAS, CMS, ALICE and LHCb. When two beams collide at LHC, the energy of the collision is the sum of the energies of the two beams. During its first three years, since the beginning of 2010 until the spring of 2013, the LHC ran at a center of mass energy of 7 to 8 TeV delivering particle collisions to its four major experiments. With the large amount of data provided by the LHC during this first period, the ATLAS and CMS experiments were able to announce the discovery of the Higgs boson on 4 July 2012, paving the way for the award of the 2013 Nobel Prize in physics to theorists François Englert and Peter Higgs [4] [5]. The machine has been following a long technical stop to prepare for running at almost double the energy of Run 1 in early 2015: the objective is to run the physics programme at 13 TeV. By providing collisions at energies never reached in a particle accelerator before, the LHC will open a new window for potential discovery, allowing further studies on the Higgs boson and potentially addressing unsolved mysteries such as dark matter.

2.1 THE CERN ACCELERATOR COMPLEX

The accelerator complex at CERN is a succession of machines with increasingly higher energies. Each machine injects the beam into the next one, which takes over to bring the beam to an even higher energy, and so on. In the LHC, the last element of this chain, each particle beam is accelerated up to the nominal energy. In addition, most of the other accelerators in the chain have their own experimental halls, where the beams are used for experiments at lower energies.

The acceleration process is the result of the combined work of all the machines in the CERN accelerator complex: the Proton Synchrotron Booster (PSB), the Proton Synchrotron (PS), the Super Proton Synchrotron (SPS) and, finally, the LHC

ACCELERATION OF PROTONS The process to accelerate protons through the accelerator complex at CERN is represented in Figure 1 and described as follows. Hydrogen atoms are taken from a bottle of hydrogen gas; an electric field is used to strip them off their orbital electrons to yield protons. Protons are injected into the PS Booster (PSB) at an energy of 50 MeV from Linac2. The booster accelerates them to 1.4 GeV. The beam is then fed to the Proton Synchrotron (PS) where it is accelerated to 25 GeV. Protons are then sent to the Super Proton Synchrotron (SPS) where they are accelerated to 450 GeV. They are finally transferred to the LHC (both in a clockwise and an anticlockwise direction, the filling time is 4'20" per LHC ring) where they are accelerated for 20 minutes to their nominal energy. Beams will circulate for many hours inside the LHC beam pipes under normal operating conditions.

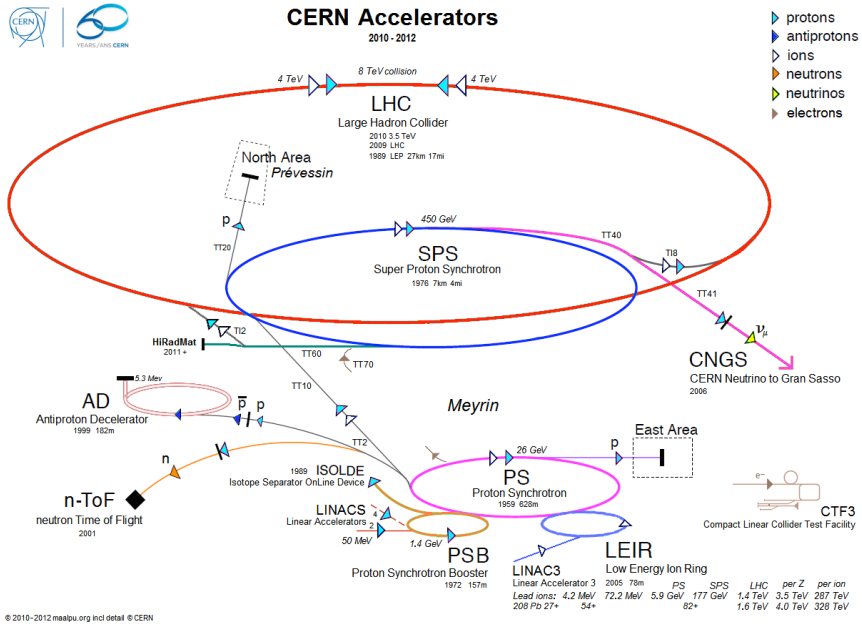

Figure 1: The Cern Accelerator Complex.

ACCELERATION OF LEAD IONS Lead ions are produced from a highly purified lead sample heated to a temperature of about 500°C. The lead vapour is ionized by an electron current. Many different charge states are produced with a maximum around Pb^{29+}. These ions are selected and accelerated to 4.2 MeV/u (energy per nucleon) before passing through a carbon foil, which strips most of them to Pb^{54+}. The Pb^{54+} beam is accumulated, then accelerated to 72 MeV/u in the Low Energy Ion Ring (LEIR), which transfers them to the PS. The PS accelerates the beam to 5.9 GeV/u and sends it to the SPS after first passing it through a second foil where it is fully stripped to Pb^{82+}. The SPS accelerates it to 177 GeV/u, then sends it to the LHC, which accelerates it to 2.76 TeV/u.

The vacuum and superconducting magnet tecnologies are fundamental for the acceleration and collisions of particles and ions

The beam pipes are vacuum tube, with a pressure of 10^{-13} atm (ultra-high vacuum), in order to avoid collisions with gas molecules. Moreover, particles are manipulated using electromagnetic devices: dipole magnets to keep them in their nearly circular orbits, quadrupole magnets to focus the beam, and accelerating cavities, which are electromagnetic resonators that accelerate particles and then keep them at a constant energy by compensating for energy losses.

2.2 LHC: LAYOUT AND PROPERTIES

SUPERCONDUCTING ELECTROMAGNETS The electromagnets contribute to optimizing the trajectory of the particles. They use a current of 11.850 Amperes to produce the field, and a superconducting coil allows the high currents to flow without losing any energy to electrical resistance. Magnets with main functions are dipoles and quadrupoles. Dipole magnets, one of the most complex parts of the LHC, are used to bend the paths of the particles. There are 1232 main dipoles, each 15 metres long and weighing in at 35 tonnes. When particles are bunched together, they are more likely to collide in greater numbers when they reach the LHC detectors. Quadrupoles help to keep the particles in a tight beam. They have four magnetic poles arranged symmetrically around the beam pipe to squeeze the beam either vertically or horizontally. The large variety of magnets in the LHC gives a total of about 9600 magnets. It includes also sextupoles, octupoles, decapoles, etc. which correct for small imperfections in the magnetic field at the extremities of the dipoles.

CAVITIES Radiofrequency (RF) cavities are metallic chambers that contain an electromagnetic field. They can be structured like beads on a string, where the beads are the cavities and the string is the beam pipe of the particle accelerator. The RF cavities are modeled to a specific size and shape so that electromagnetic waves become resonant and build up inside the cavity. Charged particles passing through the cavity feel the overall force and direction of the resulting electromagnetic field, which transfers energy to push them forwards along the accelerator. Top energy is reached in around 15 minutes, the bunches having passed the cavities around 1 million times. Each RF cavity is tuned to oscillate at 400 MHz. The 16 RF cavities on the LHC are housed in four cylindrical refrigerators called *cryomodules*, two per beam, which keep the RF cavities working in a superconducting state, without losing energy to electrical resistance.
To be more precise, to operate in a such superconducting state, the cavities require a temperature of 4.5 K (-268.7°C), while the LHC magnets use superfluid helium at 1.9 K or -271.3°C.

THE MACHINE The LHC is not a perfect circle. It is made of eight *arcs* and eight *insertions*. The arcs contain dipole magnets, with 154 in each arc. An insertion consists of a long straight section, whose layout depends on its specific use, as shown in Figure 2: physics (beam collisions within an experiment), injection, beam dumping, beam cleaning.

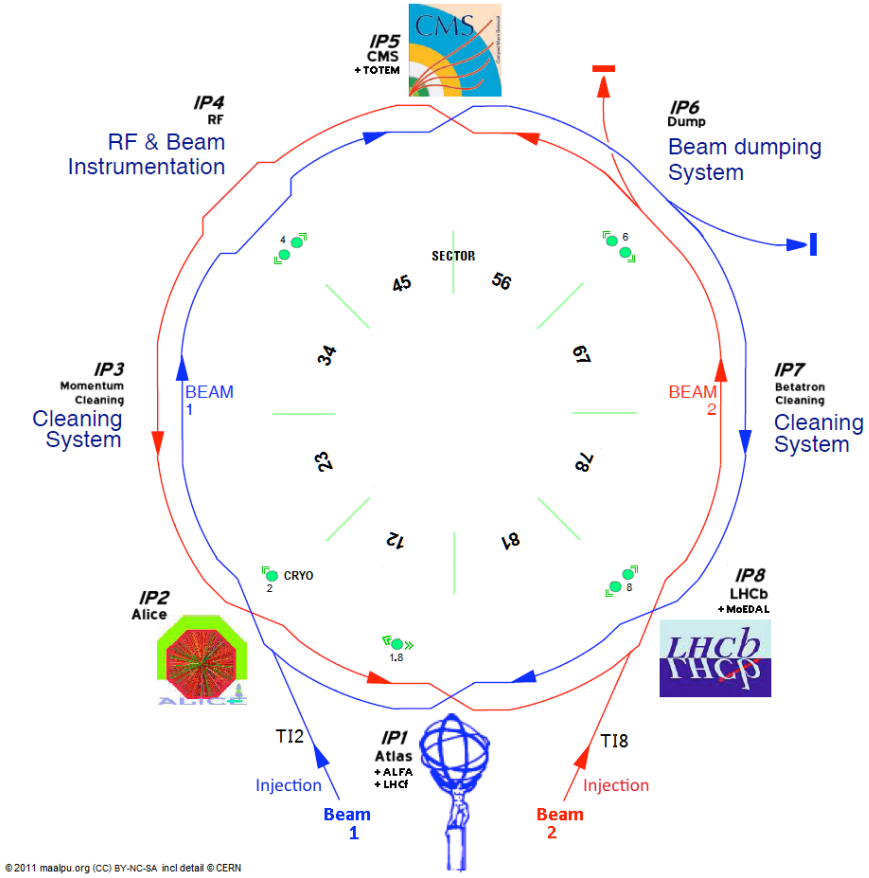

Figure 2: The LHC Layout.

The experimental insertions are located at Intersection Points (IP) 1, 5, 2 and 8; the IP2 and IP8 also contain the injection systems for the Beam 1 and the Beam 2, respectively. The remaining four straight sections do not have beam crossings. Insertions 3 and 7 each contain two collimation systems. IP4 contains two RF systems. The straight section at point 6 contains the beam dump insertion where the two beams are extracted from the machine using a combination of deflecting magnets, called *kicker magnets*. The main experiments at LHC are installed in four huge underground caverns built around the four collision points of the LHC beams: ATLAS at IP1, ALICE at IP2, CMS at IP5 and LHCb at IP8. Details about them are described in Section 2.3.

LUMINOSITY Accelerators are built to study processes whose probability varies with collision energy, and which are often rare. This means that the beam energy and the number of interesting collisions are very important parameters.

Luminosity at LHC: definition and meaning

More specifically, in a collider such as the LHC the probability for a particular process varies with the luminosity, a quantity that depends on the number of particles in each bunch, the frequency of complete turns around the ring, the number of bunches and the beam cross-section. What is needed the most is to squeeze the maximum number of particles into the smallest amount of space around the interaction region. The number of events per second generated in the LHC collisions is given by:

$$N_{event} = L\sigma_{event}, \tag{1}$$

where σ_{event} is the cross section for the event under study and L the machine luminosity. The latter depends only from the beam parameters and can be written for a Gaussian beam distribution as:

$$L = \frac{N_b^2 n_b f_{rev} \gamma_r}{4\pi\epsilon_n \beta^*} F, \tag{2}$$

where N_b is the number of particles per bunch, n_b the number of bunches per beam, f_{rev} the revolution frequency, γ_r the relativistic gamma factor, ϵ_n the normalized transverse beam emittance, β^* the beta function at the collision point anf F the geometric luminosity reduction factor due to the crossing angle at the IP:

$$F = 1/\sqrt{1 + \left(\frac{\theta_c \sigma_z}{2\sigma^*}\right)^2}, \tag{3}$$

where θ_c is the full crossing angle at the IP, σ_z the RMS bunch length and σ^* the transverse RMS beam size at the IP [1].

The LHC has two high luminosity experiments, ATLAS and CMS, aiming at a peak luminosity of $L = 10^{34} cm s^{-2}\ s^{-1}$. LHCb for B-physics is aiming at a luminosity of $L = 10^{34} cm\ s^{-2} s^{-1}$, while for the experiment ALICE in Pb-Pb ion operations $L = 10^{27} cm\ s^{-2} s^{-1}$.

Every experiment keeps track of both delivered and recorded luminosity. The delivered luminosity refers to the luminosity delivered to the experiment by the LHC. The recorded luminosity includes only the luminosity actually logged by the experiment. Ideally, the amount of luminosity recorded should be the same as the amount delivered, but in some cases the detector is unable to take data, either because its data acquisition chain is busy or because one or more of its detector subsystems is temporarily unavailable.

For instance the luminosity delivered to the CMS experiment during stable beams for p-p collisions was 44.2 pb^{-1} in 2010 ($\sqrt{s} = 7$ TeV), 6.1 fb^{-1} in 2011 ($\sqrt{s} = 7$ TeV) and 23.3 fb^{-1} in 2012 ($\sqrt{s} = 8$ TeV), as shown in Figure 3. The difference between the luminosity deliverd to and recorded by CMS in 2012 is about 7%, as shown in Figure 4 [6].

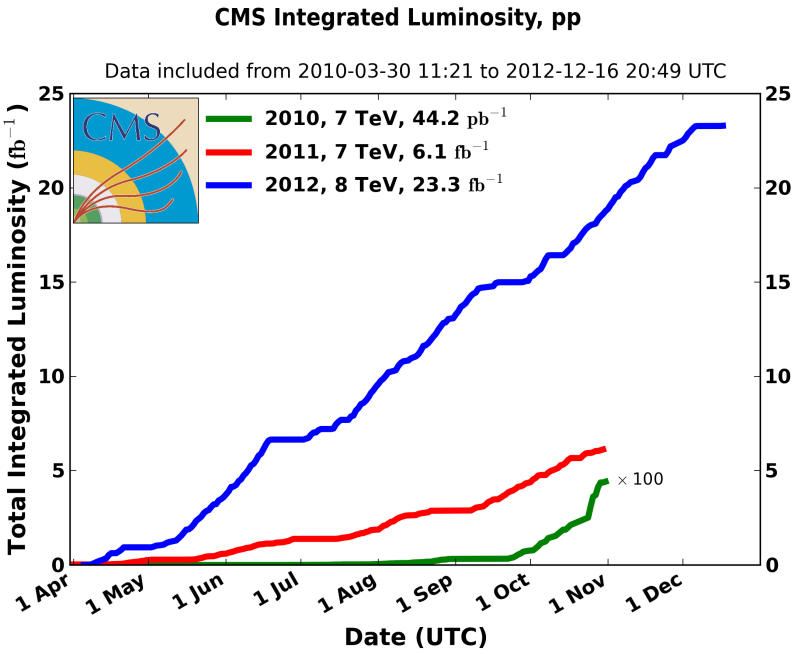

Figure 3: Delivered Luminosity versus time for 2010, 2011, 2012 (p-p data only).

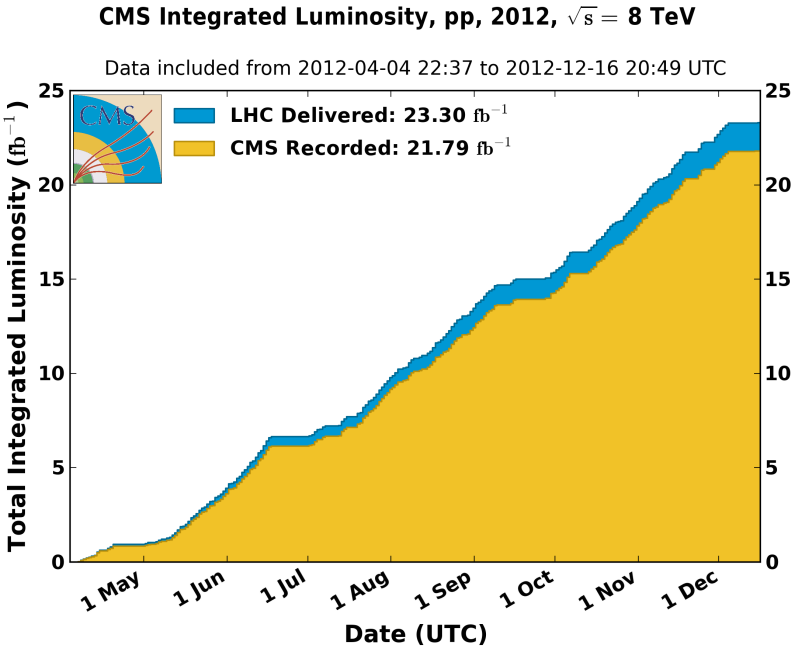

Figure 4: Total Integrated Luminosity in 2012 .

LHC PROPERTIES AND PERFORMANCE: SUMMARY The Table 1 shows the most important parameters describing the characteristics of the Large Hadrom Collider: they refer to the dimensions of the

ring, to the properties of magnets and cavities, to the beam and the luminosity.

QUANTITY	VALUE
Circumference	26,659 m
Dipole operating temperature	1.9 K (-271.3°C)
Number of magnets	9,593
Number of main dipoles	1232
Number of main quadrupoles	392
Number of RF cavities	8 per beam
Nominal energy, protons	7 TeV
Number energy, ions	2.76 TeV/u (*)
Peak magnetic dipole field	8.33 T
Min. distance between bunches	$\sim 7m$
Design luminosity	$10^{34}cm^{-2}s^{-1}$
N. of bunches per proton beam	2808
N. of protons per bunch (at start)	$1.1x10^{11}$
Number of turns per second	11,245
Number of collisions per second	600 million

Table 1: Main characteristics for the LHC

2.3 THE EXPERIMENTS AT LHC

A brief description of the major experiments at the LHC follows.

- A Toroidal LHC Apparatus (ATLAS) investigates a wide range of physics, from the search for the Higgs boson to extradimensions and dark matter. At 46 m long, 25 m high and 25 m wide, the 7000-tonne ATLAS detector is the largest volume particle detector ever constructed. Its major components are the Inner Detector, the Liquid-Argon (LAr) Electromagnetic Calorimeter and the Hadron Calorimeter surrounded by the Muon Spectrometer, the Magnet System and, for the data acquisition and computing, the Trigger System. The Magnet System consists in a central solenoid (CS) providing the Inner Detector with magnetic field, surrounded by three large air-core toroids generating the magnetic field for the muon spectrometer [2]. The layout of the ATLAS detector is shown in Figure 5.

- A Large Hadron Collider Experiment (ALICE) studies the physics of strongly interacting matter at extreme energy densities, where

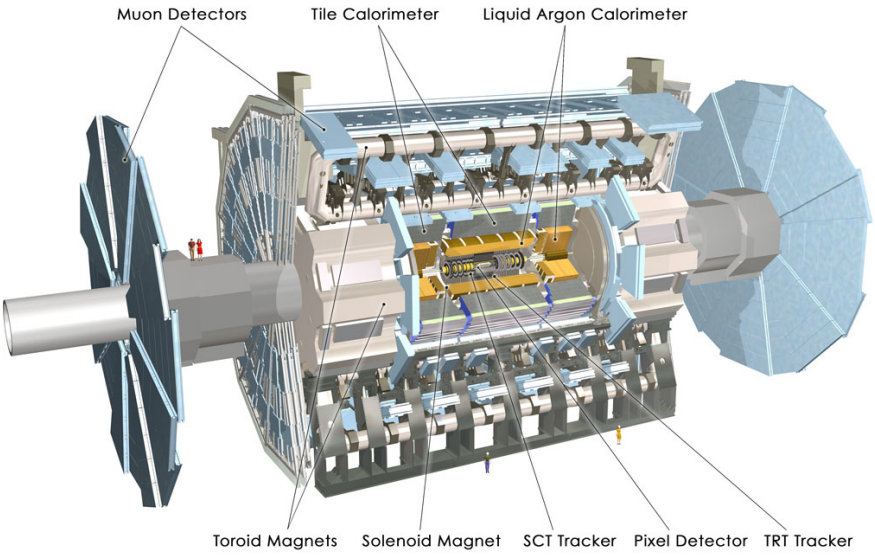

Figure 5: Layout of the ATLAS detector.

the formation of a new phase of matter, the quark-gluon plasma, is expected. The existence of such a phase and its properties are key issues in QCD for the understanding of confinement and of chiral-symmetry restoration. For this purpose ALICE carries out a comprehensive study of the hadrons, electrons, muons and photons produced in the collision of heavy nuclei. The tracking system, the calorimeters and the muon system are distinguishable in Figure 6, which shows the layout of the detector.

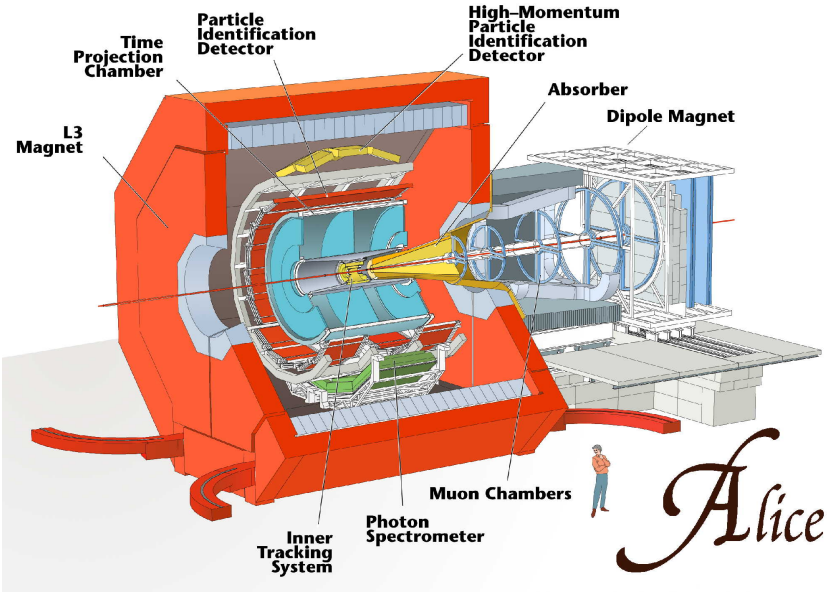

Figure 6: Layout of the ALICE detector.

- The Compact Muon Solenoid experiment (CMS) is a general-purpose detector, designed to investigate many topics in physics, such as the search for the Higgs boson, extradimensions, and particles that could make up dark matter. Although it has the same scientific goals as the ATLAS experiment, it uses different technical solutions and a different magnet-system design. The CMS detector is built around a huge solenoid magnet. This takes the form of a cylindrical coil of superconducting cable that generates a field of 4 tesla. The field is confined by a steel *yoke* that forms the bulk of the 12,500-tonne weight of the detector. An unusual feature of the CMS detector is that instead of being built in-situ like the other giant detectors of the LHC experiments, it was constructed in 15 sections at ground level before being lowered into an underground cavern near Cessy in France and reassembled. The complete detector is 21 metres long, 15 metres wide and 15 metres high; its design and components are shown in Figure 7.

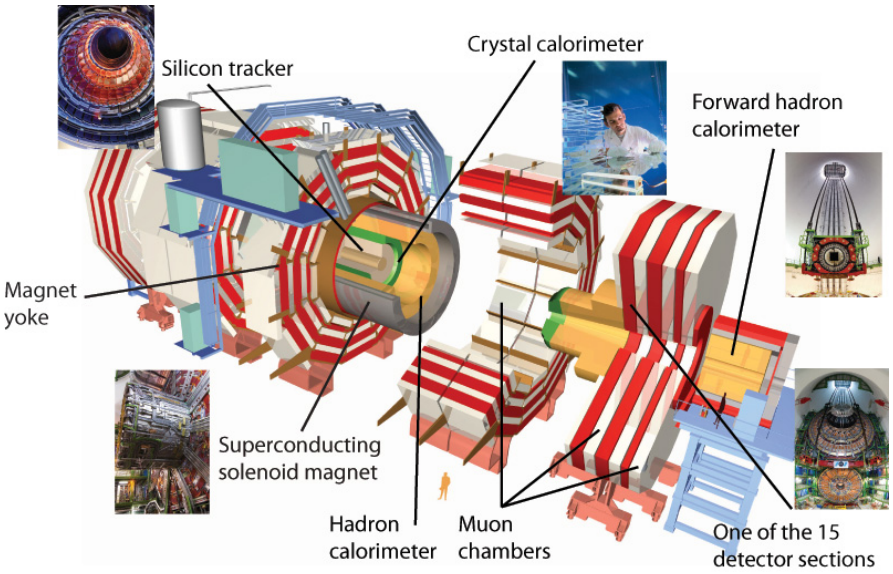

Figure 7: Layout of the CMS detector.

- The Large Hadron Collider beauty (LHCb) specializes in investigating the differences between matter and antimatter by studying a type of particle called *beauty quark*, or *b quark*. To be more precise the experiment records the decay of particles containing b and anti-b quarks, collectively known as B mesons. The experiment's 4,500 tonne detector is specifically designed to filter out these particles and the products of their decay. Rather than flying out in all directions, B mesons formed by the colliding proton beams (and the particles they decay into) stay close to

the line of the beam pipe, and this is reflected in the design of the detector. Other LHC experiments surround the entire collision point with layers of sub-detectors, but in the LHCb detector the first subdetector is mounted close to the collision point, with the others following one behind the other over a length of 20 metres. The layout is shown in Figure 8.

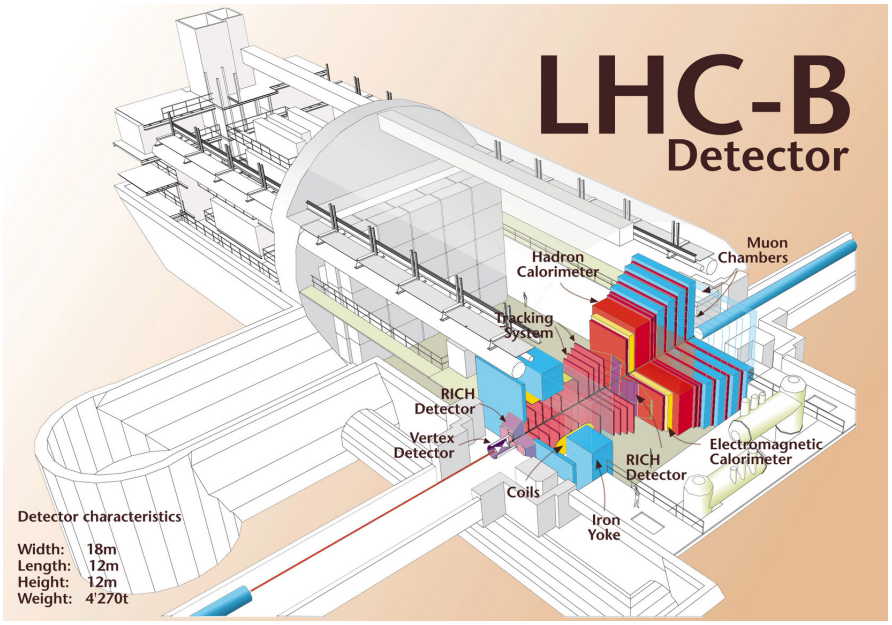

Figure 8: Layout of the LHCb detector.

OTHER EXPERIMENTS AT LHC The Large Hadron Collider hosts other three experiments: the TOTal Elastic and diffractive cross section Measurement (TOTEM), the Large Hadron Collider forward (LHCf) and the Monopole and Exotics Detector at the Large Hadron Collider (MoEDAL) experiments.

TOTEM physics programme is focused on the in-depth study of the proton's structure by looking at elastic scattering over a large range of momentum transfer. Many details of the processes that are closely linked to proton structure and low-energy QCD remain poorly understood, so TOTEM investigates a comprehensive menu of diffractive processes, the latter partly in co-operation with the CMS experiment, which is located at the same interaction point (IP5) on the LHC.

LHCf is the smallest one of the LHC experiments. It is installed on the accelerator ring near the ATLAS experiment region. The aim of this experiment is the study of the neutral particles (neutral pions, gammas and neutrons) production cross sections in the very forward region of proton-proton and nucleus-nucleus interactions. This study can give important informations for understanding the development of the atmospheric showers induced by very high energy cosmic rays

hitting the Earth atmosphere. In particular two main problems can be addressed by LHCf results: the first is the uncertainty of cosmic-ray spectrum composition between 10^{15} eV and 10^{19} eV; the latter is the interpretation of data around and beyond 10^{20} eV on the basis of GZK cutoff. Both these items are crucial for understanding the origin of cosmic rays.

The MoEDAL detector is deployed around the same intersection region as the LHCb detector. The goal of MoEDAL is to directly search for the Magnetic Monopole or Dyon; it is also looking for highly ionizing Stable (or pseudo-stable) Massive Particles (SMPs), predicted by theories beyond the Standard Model.

3

THE CMS EXPERIMENT AT LHC

The CMS experiment at CERN is a general-purpose experiment located at the Intersection Point IP5 of LHC. Its physics goals concern the search for the Higggs Boson and the study of the related properties, the search for supersimmetric particles, for new massive vector bosons, the study of extradimensions, studies about Heavy-ion physics.

3.1 THE PHYSICS OF CMS

HIGGS BOSON The electroweak symmetry breaking machanism is invoked by the Standard Model (SM), as well as in many other theories beyond the Standard Model like Supersymmetry, in order to explain the origin of the mass of elementary particles. It predicts the existence of the Higgs boson, which has been observed by CMS and ATLAS experiments in 2012. Further studies on the Higgs Boson will be conducted starting from 2015.

SUPERSYMMETRY AND DARK MATTER Supersymmetry (SUSY) theories are able to solve many problems of the SM and could provide a way to unify the electromagnetic, weak and strong forces. SUSY theories predict the existence of an higher broken symmetry which sets the correspondence between any SM particle with a super-partner (sparticle), which has same charge but different spin. The lightest neutral sparticle is one of the most promising candidate to form the dark matter, of which most of the Universe is made but could not be detected so far. CMS looks for signatures of sparticles, considered to be much heavier of the SM partners.

EXTRA DIMENSIONS The idea nderlying string theory is the idea that fundamental particles are not really like points or dots, but rather small loops of vibrating strings. All the different particles and forces are just different oscillation modes of a unique type of string. The theory also implies that besides the familiar three–dimensional world and the fourth dimension of time, there are six additional unseen spatial dimensions. In detecting them, one option would be to find evidence of another host of particles that can only exist if there are more dimensions. Theories that postulate these extradimensions predict that, like an atom having a low energy ground state and then more energetic states, there must be heavier versions of standard particles recurring at higher and higher energies as they navigate

smaller dimensions. These have been called *Kaluza-Klein recurrences* and would have exactly the same properties as standard particles (and so be visible to the detector) but at a greater mass. If CMS were to find a Z-like particle (the Z boson being one of the carriers of the electroweak force) at 2 TeV for instance, this might suggest the presence of extra dimensions.
Another way to find evidence for string theory is through the disappearance of gravitons, the hypothesised carriers of gravity, into these other dimensions. The particle might be carried away without a trace, but it would leave behind an imbalance in momentum and energy. This is why the detector must be as *hermetic* as possible, that is, it must be able to catch, to the extent possible, every particle emerging from the collisions, so can be deduced that particles have genuinely disappeared, and have not just been missed by the detector.
Finally, another speculative way of revealing extra dimensions would be through the production of *Micro Quantum Black Holes*; if they do appear they would disintegrate extremely rapidly, in around 10-27 seconds, as they decay into Standard Model or SUSY particles, producing many jets and leptons.

MATTER - ANTIMATTER ASYMMETRY At the origin of the Universe, matter and antimatter should have been created in equal amounts, but the Universe today is dominated by the matter. A clue to the answer into this question may be provided by the phenomenon of Charge-Parity (CP) violation, discovered over four decades ago. CP violation implies that there is a small difference in the rates at which certain particles decay and the corresponding rates at which their antiparticles decay. One such particle is the B meson and its antiparticle, which can both decay into two muons and a different meson made of charm quarks, which in turn decays further to form two pions. This decay presents a fairly simple signature for the experiment to detect. Whether the decayed particle was the B meson or its antiparticle can be established by looking at the type of muon produced by the decay of the opposite b quark in the event, and so one can be to able to compare the rates of the two.

STANDARD MODEL The LHC also allows studies of QCD, electroweak and flavour physics. Precision studies can give indications for physics beyond the SM, providing complementary information with respect to direct searches. As an example, extensive tests of QCD through the measurement of the production of jets and direct photons with transverse energies up to 3–4 TeV and from cross-section measurements which fall by 11 orders of magnitude. Top quarks can be produced at the LHC with a rate measured in Hz, thus the opportunity to test the SM couplings and spin of the top quark is available provided good identification of b-jets in the decays is possible.

Searches for flavour changing neutral currents, lepton flavour violation through $\tau \to 3\mu$ or $\tau \to \mu\gamma$, measurements of $B_s^0 \to \mu\mu$, measurements of triple- and quartic-gauge couplings, etc. can open a window onto new physics. Finally, in association with TOTEM, CMS is able to cover the full range of diffractive physics as well.

HEAVY-ION PHYSICS Very strongly interacting nuclear matter is produced in high energy heavy-ion collisions. The most striking experimental signatures of the produced matter are the suppression of high p_T particles (jet quenching) and the strong elliptical flow approaching the hydrodynamic limit. The heavy-ion program investigates these fenomena, plus the quarkonium production; this requires large-acceptance, high-resolution calorimeters and tracking devices, as well as a flexible trigger.

3.2 COORDINATE CONVENTIONS

The coordinate system adopted by CMS has the origin centered at the nominal collision point inside the experiment, the y-axis pointing vertically upward, and the x-axis pointing radially inward toward the center of the LHC. Thus, the z-axis points along the beam direction toward the Jura mountains from LHC Point 5. The azimuthal angle ϕ is measured from the x-axis in the xy plane. The polar angle θ is measured from the z-axis. Pseudorapidity is defined as:

$$\eta = -\ln\left[\tan(\theta/2)\right]. \tag{4}$$

Thus, the momentum and energy measured transverse to the beam direction, denoted by p_T and E_T, respectively, are computed from the x and y components. The imbalance of energy measured in the transverse plane is denoted by E_T^{miss}.

In particular the transverse momentum is defined as follows:

$$p_T = \sqrt{p_x^2 + p_y^2}. \tag{5}$$

This decomposition is useful in hadron collider experiments, where the energy of the collision partons is unknown: in fact a fraction of the proton energy is carried by the proton remnants which are scattered at small angles and, remaining in the beam pipe, are not detected. The speed of the interacton point is also unknown, so another variable with good transformation properties under Lorentz boosts as the p_T, which is invariable, is used: it is the rapidity (y), defined as

$$y = \frac{1}{2}\ln\frac{E + p_z}{E - p_z}, \tag{6}$$

which transforms with a simple additive law. For ultra-relativistic particles, under the condition $E \simeq |\vec{p}|$, the rapidity can be approximated by the pseudorapidity, defined above.

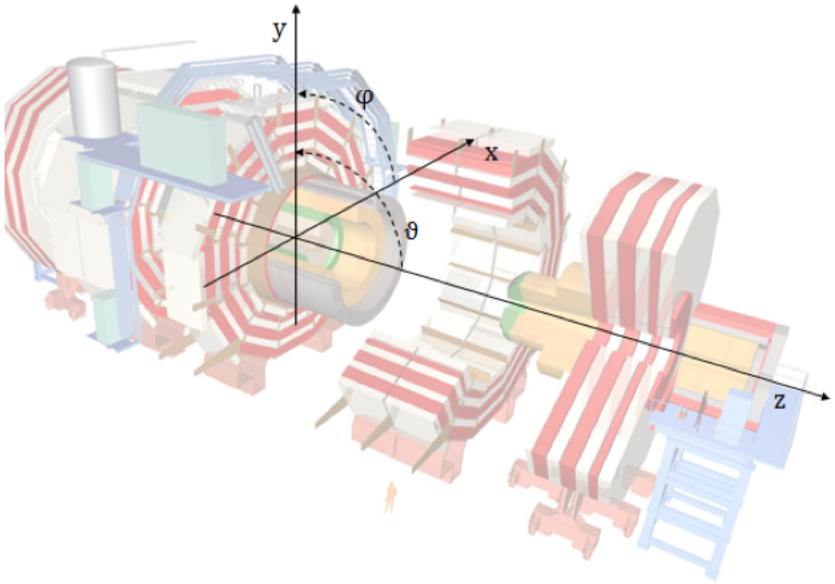

Figure 9: CMS reference system.

3.3 DETECTOR REQUIREMENTS AND LAYOUT

The detector requirements for CMS to meet the goals of the LHC physics programme can be summarized as follows:

- a high performance system to detect and measure muons;
- a high quality central tracking system to give accurate momentum measurements, supported by efficient triggering and offline tagging of τ's and $b-jets$ and requiring pixel detectors close to the interaction region;
- a high resolution electromagnetic calorimeter to detect and measure electrons and photons;
- a hadron calorimeter with a large hermetic geometric coverage and fine lateral segmentation, designed to entirely surround the collision and prevent particles from escaping.

The design of CMS meets these requirements. The main distinguishing features of CMS are a high-field solenoid, a full silicon-based inner tracking system, and a fully active scintillating crystals-based electromagnetic calorimeter, as shown in Figure 10.

The overall layout of CMS is shown in Figure 11: the detector has a cylindrical structure, so that it can be divided into a barrel region and two endcap regions. At the heart of CMS sits a 13-m-long, 5.9 m inner diameter, 4 T superconducting solenoid. In order to achieve good momentum resolution within a compact spectrometer without making stringent demands on muon-chamber resolution and alignment,

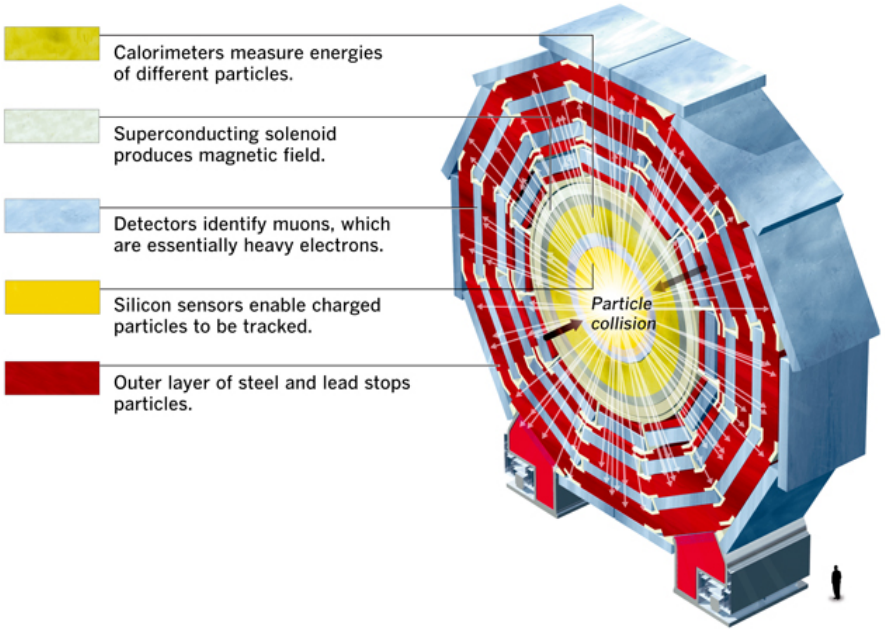

Figure 10: Various properties of particles are measured in the layers of the detector as they fly away from collisions.

a high magnetic field was chosen. The return field is large enough to saturate 1.5 m of iron, allowing 4 *muon stations* to be integrated to ensure robustness and full geometric coverage. Each muon station consists of several layers of aluminium Drift Tubes (DT) in the barrel region and Cathode Strip Chambers (CSCs) in the endcap region, complemented by Resistive Plate Chambers (RPCs).

The bore of the magnet coil is also large enough to accommodate the inner tracker and the calorimetry inside. The tracking volume is given by a cylinder of length 5.8 m and diameter 2.6 m. In order to deal with high track multiplicities, CMS employs 10 layers of silicon microstrip detectors, which provide the required granularity and precision. In addition, 3 layers of silicon pixel detectors are placed close to the interaction region to improve the measurement of the impact parameter of charged-particle tracks, as well as the position of secondary vertices. The Electromagnetic Calorimeter (ECAL) uses lead tungstate ($PbWO_4$) crystals with coverage in pseudorapidity up to $|\eta| < 3.0$. The scintillation light is detected by Silicon Avalanche Photodiodes (APDs) in the barrel region and Vacuum PhotoTriodes (VPTs) in the endcap region. A preshower system is installed in front of the endcap ECAL for π_0 rejection. The ECAL is surrounded by a brass/scintillator sampling hadron calorimeter with coverage up to $|\eta| < 3.0$. The scintillation light is converted by wavelength-shifting (WLS) fibres embedded in the scintillator tiles and channeled to photodetectors via clear fibres. This light is detected by novel photodetectors (hybrid photodiodes, or HPDs) that can provide gain and oper-

ECAL will be described in more detail in its dedicated Chapter 4.

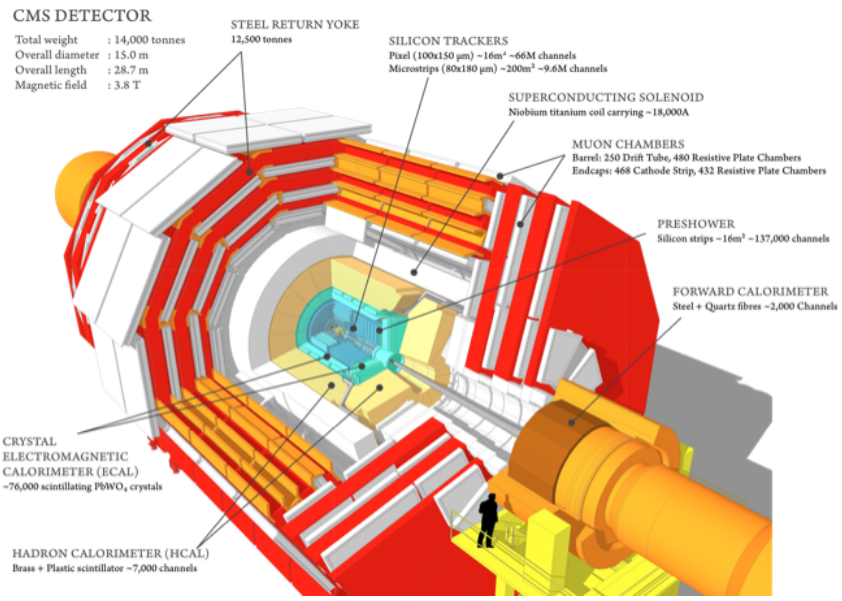

Figure 11: Components of the CMS detector.

ate in high axial magnetic fields. This central calorimetery is complemented by a *tail-catcher* in the barrel region, ensuring that hadronic showers are sampled with nearly 11 hadronic interaction lengths. Coverage up to a pseudorapidity of 5.0 is provided by an iron/quartz-fibre calorimeter. The Cerenkov light emitted in the quartz fibres is detected by photomultipliers. The forward calorimeters ensure full geometric coverage for the measurement of the transverse energy in the event. The overall dimensions of the CMS detector are a length of 21.6 m, a diameter of 14.6 m and a total weight of 12500 tons. The thickness of the detector in radiation length is greater than 25 X_0 for the ECAL, and the thickness in interaction lengths varies from $7 - 11\ \lambda$ for HCAL depending on η.
An overall picture of the detector is shown in Figure 11.

3.3.1 *The magnet*

As already said before, CMS aims to achieve a good momentum resolution ($\Delta p/p = 10\%$), even for momenta up to 1 TeV. The larger the bending power the better the momentum resolution, so even with a not enormous solenoid it's possible to meet this goal obtaining an high axial magnetic field of 4 T with the superconducting technology. This allows to avoid stringent demands on spatial resolution of muon chambers and on tracker alignment. Moreover, thanks to the the axial direction of the field is possible to start measuring the momentum at $r = 0$ (unlike a toroidal configuration), resulting in a more compact

design of the whole spectrometer. In Table 2 the main parameters of the CMS magnet are listed.

Magnetic field	4 T
Inner bore	5.9 m
Length	12.9 m
Number of turns	2168
Current	19.5 kA
Stored energy	2.7 GJ
Total weight	$\simeq$ 1200 tons

Table 2: Main parameters of the CMS magnet

Superconducting magnets were already used in high energy physics successfully (LEP and HERA experiments) but new challenges came out for CMS to reach better performances. CMS solenoid employs high purity aluminium conductors, with a cross section of 64×22 mm^2. To keep the necessary low temperatures (about 4 K) an indirect termosyphon cooling is used together with epoxy resin impregnation.

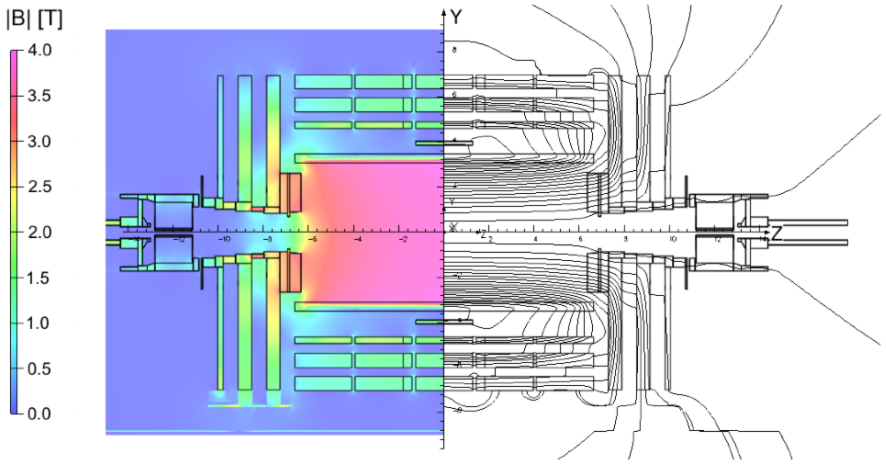

Figure 12: Map of the |B| field (left) and field lines (right) predicted for a longitudinal section of the CMS detector by a magnetic field model at a central magnetic flux density of 3.8 T. Each field line represents a magnetic flux increment of 6 Wb.

3.3.2 *Inner tracking system*

This detector is subdivided into a cylindrical barrel (see Figure 84 in the Appendix A) and two End Caps (see Figure 85 in the Appendix A) to almost hermetically cover the interaction point. By considering the charged particle flux at various radii at high luminosity, three regions can be delineated:

- Closest to the interaction vertex where the particle flux is the highest ($\approx 10^7/\mathrm{satr} \approx 10$ cm), pixel detectors are placed. The size of a pixel is $\approx 100 \times 150\ \mu m^2$, giving an occupancy of about 10^{-4} per pixel per LHC crossing.

- In the intermediate region ($20 < r < 55$ cm), the particle flux is low enough to enable use of silicon microstrip detectors with a minimum cell size of 10 cm $\times$ 80 μm, leading to an occupancy of $\approx 2-3\%$ per LHC crossing.

- In the outermost region ($r > 55$ cm) of the inner tracker, the particle flux has dropped sufficiently to allow use of larger-pitch silicon microstrips with a maximum cell size of 25 cm $\times$ 180 μm, whilst keeping the occupancy to $\approx 1\%$.

Even in heavy-ion (Pb-Pb) running, the occupancy is expected to be at the level of 1% in the pixel detectors and less than 20% in the outer silicon strip detectors, permitting track reconstruction in the high density environment.
The layout of the CMS tracker is shown in Figure 13. Close to the interaction vertex, in the barrel region, there are the three layers of hybrid pixel detectors. In the barrel part there are the silicon microstrip detectors, while the forward region has two pixel and nine microstrip layers in each of the two Endcaps. The barrel part is separated into an Inner and an Outer Barrel. In order to avoid excessively shallow track crossing angles, the Inner Barrel is shorter than the Outer Barrel, and there are an additional 3 Inner Disks in the transition region between the barrel and endcap parts, on each side of the Inner Barrel. The total area of the pixel detector is $\approx 1\ m^2$, whilst that of the silicon strip detectors is 200 m^2, providing coverage up to $|\eta| < 2.4$. The inner tracker comprises 66 million pixels and 9.6 million silicon strips.

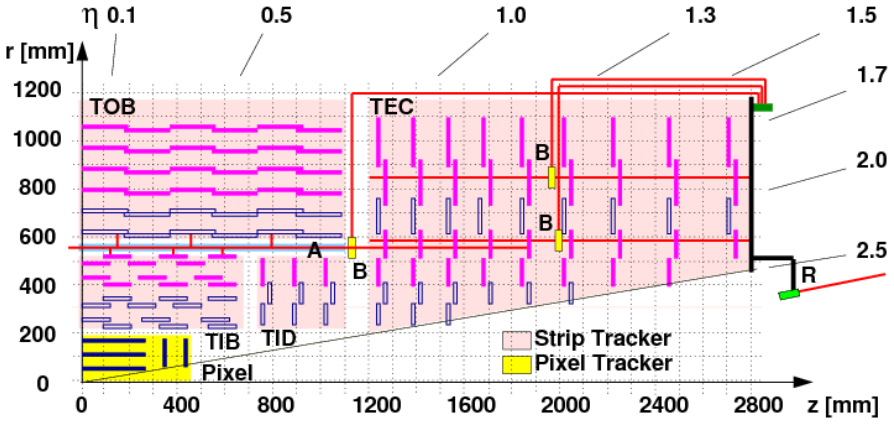

Figure 13: The tracker layout (1/4 of the z view).

STRIP TRACKER The barrel tracker region is divided into two parts: a Tracker Inner Barrel (TIB) and a Tracker Outer Barrel (TOB). The TIB is made of 4 layers and covers up to $|z| < 65$ cm, using silicon sensors with a thickness of 320 μm and a strip pitch which varies from 80 to 120 μm. The first two layers are made with *stereo modules* in order to provide a measurement in both $r - \phi$ and $r - z$ coordinates. A stereo angle of 100 mrad has been chosen. This leads to a single-point resolution of between 23–34 μm in the $r - \phi$ direction and 230 μm in z. The TOB comprises six layers with a half-length of $|z| < 110$ cm. As the radiation levels are smaller in this region, thicker silicon sensors (500 μm) can be used to maintain a good S/N ratio for longer strip length and wider pitch. The strip pitch varies from 120 to 180 μm. Also for the TOB the first two layers provide a stereo measurement in both $r - \phi$ and $r - z$ coordinates. The stereo angle is again 100 mrad and the single-point resolution varies from 35–52 μm in the $r - \phi$ direction and 530 μm in z.

The endcaps are divided into the TEC (Tracker EndCap) and TID (Tracker Inner Disks). Each TEC comprises 9 disks that extend into the region 120 cm $< |z| <$ 280 cm, and each TID comprises 3 small disks that fill the gap between the TIB and the TEC. The TEC and TID modules are arranged in rings, centered on the beam line, and have strips that point towards the beam line, therefore having a variable pitch. The first 2 rings of the TID and the innermost 2 rings and the fifth ring of the TEC have stereo modules. The thickness of the sensors is 320 μm for the TID and the 3 innermost rings of the TEC and 500 μm for the rest of the TEC.

The entire silicon strip detector consists of almost 15,400 modules, which will be mounted on carbon-fibre structures and housed inside a temperature controlled outer support tube. The operating temperature will be around -20 °C.

PIXEL TRACKER The pixel detector consists of three barrel layers with two endcap disks on each side on them, as shown in Figure 14. The three barrel layers are located at mean radii of 4.4 cm, 7.3 cm and 10.2 cm, and have a length of 53 cm. The two end disks, extending from 6 to 15 cm in radius, are placed on each side at $|z| = 34.5$ cm and 46.5 cm, with 6 cm $< r <$ 15 cm. High granularity is mandatory to get good vertex resolution, so $\approx 100 \times 150$ μm^2 pixel area is set either along z and in r plane. The whole inner tracker hosts about 66 million pixels. The spatial resolution of the pixel detector is approximately 10 m and 20 m in r and z coordinate respectively.

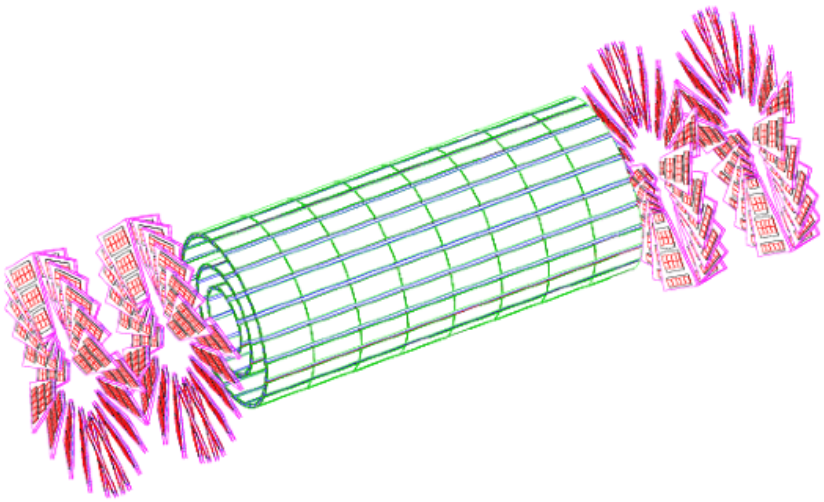

Figure 14: Layout of pixel detectors in the CMS tracker.

3.3.3 *Electromagnetic Calorimeter*

The Electromagnetic Calorimeter (ECAL) is a hermetic, homogeneous calorimeter comprising 61200 lead tungstate ($PbWO_4$) crystals mounted in the central barrel part, and 7324 crystals in each of the two endcaps. CMS has chosen lead tungstate scintillating crystals for its ECAL. These crystals have short radiation ($X_0 = 0.89$ cm) and Moliere (2.2 cm) lengths, are fast (80% of the light is emitted within 25 ns) and radiation hard. However, the relatively low light yield (30 γ/MeV) requires use of photodetectors with intrinsic gain that can operate in a magnetic field. Silicon Avalanche Photodiodes (APDs) are used as photodetectors in the barrel and Vacuum Phototriodes (VPTs) in the endcaps. In addition, the sensitivity of both the crystals and the APD response to temperature changes requires a temperature stability (the goal is 0.1 °C). The use of $PbWO_4$ crystals has thus allowed the design of a compact calorimeter inside the solenoid that is fast, has fine granularity, and is radiation resistant.

The barrel section (EB) has an inner radius of 129 cm. It is structured as 36 identical *supermodules*, each covering half the barrel length and corresponding to a pseudorapidity interval of $0 < \eta < 1.479$. The crystals are quasi-projective (the axes are tilted at 3° with respect to the line from the nominal vertex position) and cover 0.0174 (i.e. 1°) in $\Delta\phi$ and $\Delta\eta$. The crystals have a front face cross-section of $\approx 22 \times 22\ mm^2$ and a length of 230 mm, corresponding to 25.8 X_0.

The endcaps (EE), at a distance of 314 cm from the vertex and covering a pseudorapidity range of $1.479 < \eta < 3.0$, are each structured as two *Dees*, consisting of semi-circular aluminium plates from which are cantilevered structural units of 5×5 crystals, known as *supercrys-*

tals. The basic mechanical unit was envisaged to hold 6×6 crystals. The change was accommodated by a corresponding increase in the lateral size of the crystals. The endcap crystals, like the barrel crystals, off-point from the nominal vertex position, but are arranged in an x-y grid. They are all identical and have a front face cross section of 28.6×28.6 mm^2 and a length of 220 mm ($24.7\ X_0$). A preshower device is placed in front of the crystal calorimeter over much of the endcap pseudorapidity range. The active elements of this device are two planes of Silicon Strip Detectors, with a pitch of 1.9 mm, which lie behind disks of lead absorber at depths of $2\ X_0$ and $3\ X_0$.

ELECTRONICS READOUT The signal coming from the photodetectors goes through a multi-gain preamplifier, when it is amplified and shaped to peak after about 50 ns; then it is sampled and digitized at 40 MHz by a 12-bit ADCs. In the corresponding trigger system, consecutive digitizations within a defined time frame (250 ns) are read out. In order to obtain the amplitude of a digitized pulse, the samples within the time frame are weighted and summed.
The ECAL readout electronics is described in more details in Chapter 4.

3.3.4 *Hadron calorimeter*

The design of the hadron calorimeter (HCAL) is strongly influenced by the choice of magnet parameters since most of the CMS calorimetry is located inside the magnet coil and surrounds the ECAL system. An important requirement of HCAL is to minimize the non-Gaussian tails in the energy resolution and to provide good containment and hermeticity for the E_T^{miss} measurement. Hence, the HCAL design maximizes material inside the magnet coil in terms of interaction lengths. This is complemented by an additional layer of scintillators, referred to as the hadron outer (HO) detector, lining the outside of the coil. Brass has been chosen as absorber material as it has a reasonably short interaction length, is easy to machine and is non-magnetic. Maximizing the amount of absorber before the magnet requires keeping to a minimum the amount of space devoted to the active medium. The tile/fibre technology makes for an ideal choice. It consists of plastic scintillator tiles read out with embedded wavelength-shifting (WLS) fibres. The WLS fibres are spliced to high-attenuation-length clear fibres outside the scintillator that carry the light to the readout system. The photodetection readout is based on multi-channel hybrid photodiodes (HPDs). The absorber structure is assembled by bolting together precisely machined and overlapping brass plates so as to leave space to insert the scintillator plates, which have a thickness of 3.7 mm. The overall assembly enables the HCAL to be built with essentially no uninstrumented cracks or dead areas in ϕ. The gap between

the barrel and the endcap HCAL, through which the services of the ECAL and the inner tracker pass, is inclined at 53° and points away from the centre of the detector.

HADRON OUTER The hadron outer (HO) detector contains scintillators with a thickness of 10 mm, which line the outside of the outer vacuum tank of the coil and cover the region $-1.26 < \eta < 1.26$. The tiles are grouped in 30° -sectors, matching the ϕ segmentation of the DT chambers. They sample the energy from penetrating hadron showers leaking through the rear of the calorimeters and so serve as a *tail-catcher* after the magnet coil. They increase the effective thickness of the hadron calorimetry to over 10 interaction lengths, thus reducing the tails in the energy resolution function. The HO also improves the E_T^{miss} resolution of the calorimeter.

HO is physically located inside the barrel muon system and is hence constrained by the geometry and construction of that system. It is divided into 5 sections along η, called *rings* 2, 1, 0, 1, and 2. The fixed ring-0 has 2 scintillator layers on either side of an iron absorber with a thickness of about 18 cm, at radial distances of 3,850 m and 4,097 m, respectively. The other mobile rings have single layers at a radial distance of 4,097 m. Each ring covers 2.5 m in z. HO scintillators follow the HCAL barrel tower geometry in η and ϕ.

HADRON ENDCAP Each hadron endcap of HCAL consists of 14 η towers with 5° ϕ segmentation, covering the pseudorapidity region $-1.3 < \eta < 3.0$. For the 5 outermost towers (at smaller η) the ϕ segmentation is 5° and the η segmentation is 0.087. For the 8 innermost towers the ϕ segmentation is 10°, whilst the η segmentation varies from 0.09 to 0.35 at the highest η. The total number of HE towers is 2,304.

HADRON FORWARD Coverage between pseudorapidities of 3.0 and 5.0 is provided by the steel/quartz fibre Hadron Forward (HF) calorimeter. Because the neutral component of the hadron shower is preferentially sampled in the HF technology, this design leads to narrower and shorter hadronic showers and hence is ideally suited for the congested environment in the forward region. The front face is located at 11.2 m from the interaction point. The depth of the absorber is 1.65 m. The signal originates from Cerenkov light emitted in the quartz fibres, which is then channeled by the fibres to photomultipliers. The absorber structure is created by machining 1 mm square grooves into steel plates, which are then diffusion welded. The diameter of the quartz fibres is 0.6 mm and they are placed 5 mm apart in a square grid. The quartz fibres, which run parallel to the beam line, have two different lengths (namely 1.43 m and 1.65 m) which are inserted into grooves, creating two effective longitudinal samplings. There are 13

towers in η, all with a size given by $\Delta\eta \approx 0.175$, except for the lowest η tower with $\Delta\eta \approx 0.1$ and the highest η one which has $\mathrm{Delta}\eta \approx 0.3$. The ϕ segmentation of all towers is $10°$, except for the highest η one which has $\Delta\phi = 20°$. This leads to 900 towers and 1800 channels in the 2 HF modules.

3.3.5 *Muon system*

Centrally produced muons are measured 3 times: in the inner tracker, after the coil and in the return flux. Measurement of the momentum of muons using only the muon system is essentially determined by the muon bending angle at the exit of the 4 T coil, taking the interaction point (which will be known to $\approx 20\ \mu m$) as the origin of the muon. The resolution of this measurement (labelled *muon system only* in Figure 15) is dominated by multiple scattering in the material before the first muon station up to p_T values of 200 GeV/c, when the chamber spatial resolution starts to dominate. For low-momentum muons, the best momentum resolution (by an order of magnitude) is given by the resolution obtained in the silicon tracker (*inner tracker only* in Figure 15). However, the muon trajectory beyond the return yoke extrapolates back to the beam-line due to the compensation of the bend before and after the coil when multiple scattering and energy loss can be neglected. This fact can be used to improve the muon momentum resolution at high momentum when combining the inner tracker and muon detector measurements (*full system* in Figure 15).

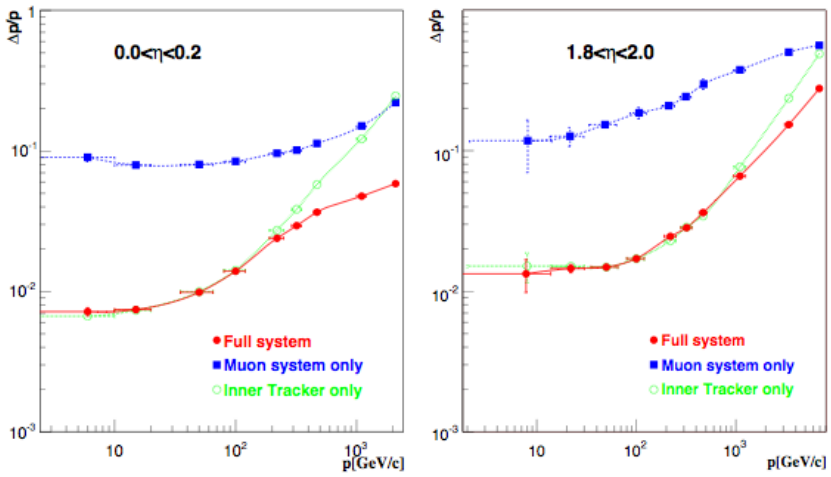

Figure 15: The muon momentum resolution versus p using the muon system only, the inner tracker only, or both (full system).

Three types of gaseous detectors are used to identify and measure muons. The choice of the detector technologies has been driven by the very large surface to be covered and by the different radiation

environments. In the barrel region ($|\eta| < 1.2$), where the neutron induced background is small, the muon rate is low and also the residual magnetic field in the chambers is low, Drift Tube (DT) chambers are used. In the two endcaps, where the muon rate as well as the neutron induced background rate is high, and the magnetic field is also high, Cathode Strip Chambers (CSC) are deployed and cover the region up to $|\eta| < 2.4$. In addition to this, Resistive Plate Chambers (RPC) are used in both the barrel and the endcap regions. These RPCs are operated in avalanche mode to ensure good operation at high rates (up to 10 kHz/cm^2) RPCs provide a fast response with good time resolution but with a coarser position resolution than the DTs or CSCs. RPCs can therefore identify unambiguously the correct bunch crossing. The DTs or CSCs and the RPCs operate within the first level trigger system, providing two independent and complementary sources of information. The complete system results in a robust, precise and flexible trigger device. In the initial stages of the experiment, the RPC system will cover the region $|\eta| < 1.6$.

The layout of one quarter of the CMS muon system for initial low luminosity running is shown in Figure 16. In the Muon Barrel (MB) region, four stations of detectors are arranged in cylinders interleaved with the iron yoke. The segmentation along the beam direction follows the five wheels of the yoke (labeled *YB-2* for the farthest wheel in -z, and *YB+2* for the farthest is +z). In each of the endcaps, the CSCs and RPCs are arranged in four disks perpendicular to the beam, and in concentric rings, three rings in the innermost station, and two in the others. In total, the muon system contains of order 25,000 m^2 of active detection planes, and nearly 1 million electronic channels.

3.3.6 *Trigger and data acquisition*

The CMS Trigger and Data Acquisition (DAQ) System is designed to inspect the detector information at the full beam crossing frequency and to select events of interest; It provide for an early decision followed by an online selection, in order to avoid running the offline code on millions of uninteresting events. To be more precise, the LHC bunch crossing rate of 40 MHz leads to $\approx 10^9$ interactions/sec at the design luminosity. Data from only about 10^2 crossings/sec can be written to archival media; hence, the trigger system has to achieve a rejection factor of nearly 10^6. The CMS trigger and data acquisition system consists of four parts: the Front End Detector electronics (FED), the Level-1 trigger processors (calorimeter, muon, and global), the readout network, and an online event filter system (processor farm) that executes the software for the High-Level Triggers (HLT).

The full online selection is split into two main steps. The first step (Level-1 Trigger) is designed to reduce the rate of events accepted for

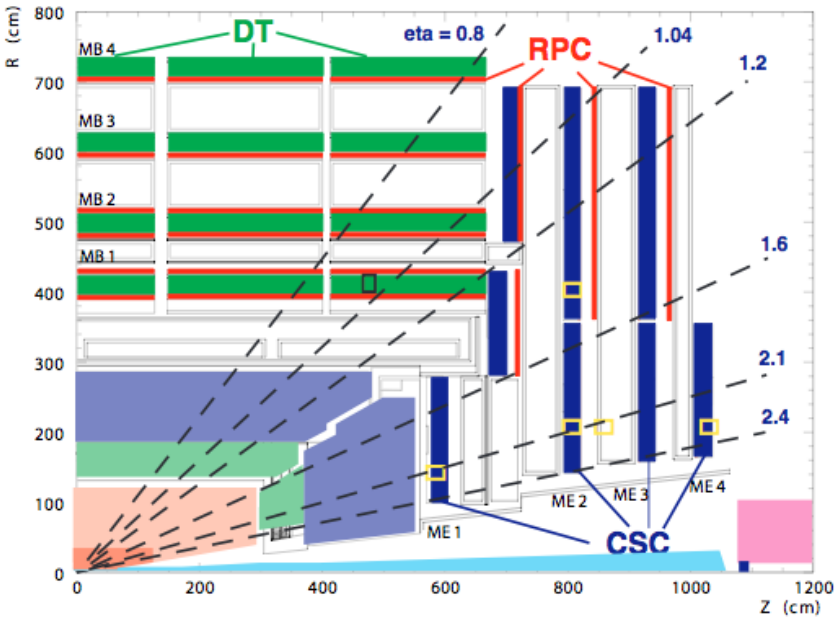

Figure 16: Layout of one quarter of the CMS muon system for initial low luminosity running. The RPC system is limited to $|\eta| < 1.6$ in the endcap, and for the CSC system only the inner ring of the ME4 chambers have been deployed.

further processing to less than 100 kHz. The second step (High-Level Trigger or HLT) is designed to reduce this maximum Level-1 accept rate to a final output rate of 100 Hz. The HLT farm, a computing cluster consisting of large amount of processers, writes the events in primary datasets depending on their trigger history.

LEVEL-1 TRIGGER The size of the LHC detectors and the underground caverns impose a minimum transit time for signals from the front-end electronics to reach the services cavern housing the Level-1 trigger logic and return back to the detector front-end electronics. The total time allocated for the transit and for reaching a decision to keep or discard data from a particular beam crossing is 3.2 μs. During this time, the detector data must be held in buffers while trigger data is collected from the front-end electronics and decisions reached that discard a large fraction of events while retaining the small fraction of interactions of interest (nearly 1 crossing in 1000). Of the total latency, the time allocated to Level-1 trigger calculations is less than 1 μs.

Custom hardware processors form the Level-1 decision. The Level-1 triggers involve the calorimetry and muon systems, as well as some correlation of informations between these systems. The Level-1 decision is based on the presence of *trigger primitive* objects such as photons, electrons, muons, and jets above set E_T or p_T thresholds. It also employs global sums of E_T and E_T^{miss}. Reduced-granularity and

reduced-resolution data are used to form trigger objects. At startup the Level-1 rate is limited to 50 kHz (the design value is 100 kHz). Taking a safety margin of a factor of 3 into account for simulation uncertainties, as well as beam and detector conditions not included in the simulation programs, leads to an estimated rate of 16 kHz. The design value of 100 kHz is set by the average time to transfer full detector information through the readout system.

Much of the logic in the trigger system is contained in custom Application Specific Integrated Circuits (ASICs), semi-custom and gate-array ASICs, Field Programmable Gate Arrays (FP- GAs), Programmable Logic Devices (PLDs), and discrete logic such as Random Access Memories that are used for memory Look-Up Tables (LUTs). Where possible and where the added flexibility offers an advantage and is cost effective, designs incorporate new FPGA technology.

During the Level-1 decision-making period, all the high-resolution data is held in pipelined memories. Commodity computer processors make subsequent decisions using more detailed informations from all of the detectors in more and more sophisticated algorithms that approach the quality of final reconstruction.

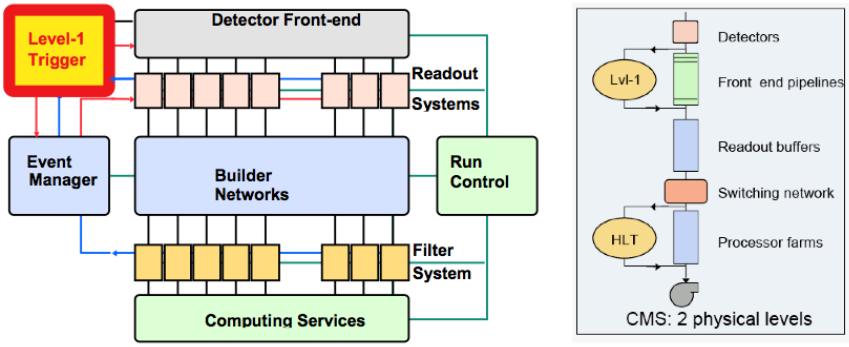

Figure 17: The CMS data acquisition system (left). The Level-1 trigger decision is distributed to the detector front end (top) as well as to off detector readout systems. Builder networks using cross-point switches construct the event record from the event fragments which come from different detector parts. The HLT (Filter System) receives and processes complete events. The CMS Level-1 trigger (right) receives data from the calorimeter and the muon detectors and produces a yes/no decision a fixed number of crossings later (latency). Pipeline memories of depth equal to the trigger latency store the data on the detector until the Level-1 decision arrives.

HIGH-LEVEL TRIGGERS Upon receipt of a Level-1 trigger, after a fixed time interval of about 3.2 µs, the data from the pipelines are transferred to front-end readout buffers. After further signal processing the data are placed in dual-port memories for access by the DAQ system. Each event, with a size of about 1.5 MB (pp interactions), is

contained in several hundred front-end readout buffers. Through the event building *switch*, data from a given event are transferred to a processor. Each processor runs the same high-level trigger (HLT) software code to reduce the Level-1 output rate of 100 kHz to 100 Hz for mass storage.

The use of a processor farm for all selections beyond Level-1 allows maximal benefit to be taken from the evolution of computing technology. Flexibility is maximized since there is complete freedom in the selection of the data to access, as well as in the sophistication of the algorithms.

Various strategies guide the development of the HLT code. Rather than reconstruct all possible objects in an event, whenever possible only those objects and regions of the detector that are actually needed are reconstructed. Events are to be discarded as soon as possible. This leads to the idea of partial reconstruction and to the notion of many virtual trigger levels, e.g., calorimeter and muon information are used, followed by use of the tracker pixel data and finally the use of the full event information (including full tracking).

3.3.7 *Software and computing*

The CMS software and computing systems needs to cover a broad range of activities including the design, evaluation, construction and calibration of the detector; the storage, access, reconstruction and analysis of data; the support of a distributed computing infrastructure for physicists engaged in these tasks. The storage, networking and processing power needed to analyse these data is well in excess of today's facilities and exceed any reasonably projected capabilities of CERN's central computing systems. The CMS computing model is therefore highly distributed, with a primary *Tier-0* centre at CERN being supplemented by Tier-1 and Tier-2 computing centres at national laboratories and universities worldwide. The computing grid technologies are used to facilitate the seamless exploitation of these distributed centres. Close collaboration is maintained with running HEP experiments to learn from their experience and adopt and extend appropriate computing technologies they have developed. The *LHC Computing Grid*, a joint project of the experiments and laboratories, is proceeding towards integration and deployment of grid technologies for LHC. The organization of tiers is shown in Figure 18.

DATA FORMATS Physically, an *Event* is the result of a single readout of the detector electronics and the signals that will (in general) have been generated by particles, tracks, energy deposits, present in a number of bunch crossings. The task of the online Trigger and Data Acquisition System (TriDAS) is to select, out of the millions of events recorded in the detector, the most interesting 100 or so per second,

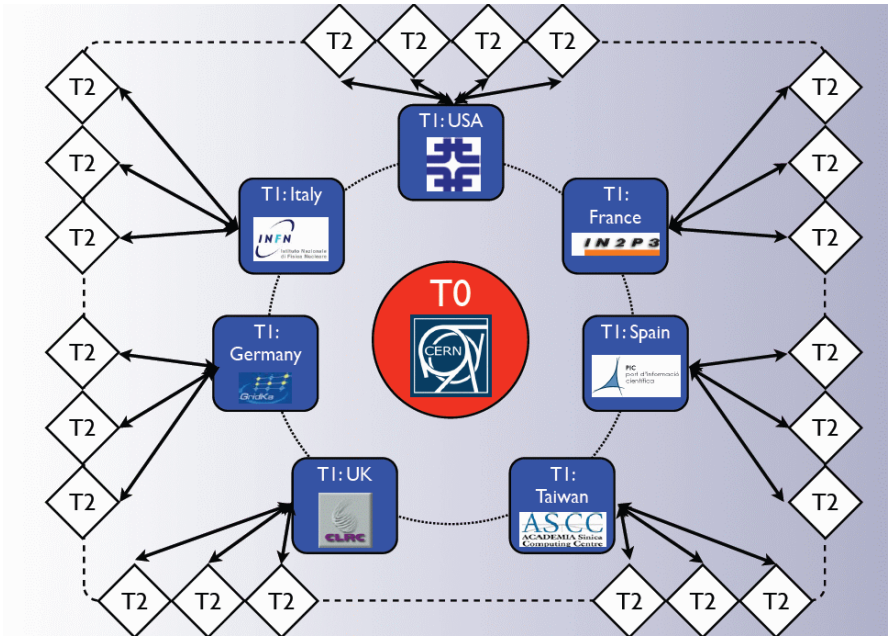

Figure 18: CMS tiers structure.

and then store them for further analysis. An event has to pass two independent sets of tests, or Trigger Levels, in order to qualify. The tests range from simple and of short duration (Level-1) to sophisticated ones requiring significantly more time to run (High Levels 2 and 3, called HLT). In the end, the HLT system creates RAW data events containing the detector data, the level 1 trigger result, the result of the HLT selections (HLT trigger bits) and some of the higher-level objects created during HLT processing.
The term RAW refers to a particular class of data; in fact CMS Data is arranged into a hierarchy of data tiers, each with different uses. The three main data tiers written in CMS are:

- RAW: full event information from the Tier-0 (i.e. from CERN), containing *raw* detector informations (detector element hits, etc); RAW is not used directly for analysis;
- RECO (*RECOnstructed data*): the output from first-pass processing by the Tier-0. This layer contains reconstructed physics objects (primary and secondary vertex, particle identification), but it's still very detailed. RECO can be used for analysis, but is too big for frequent or heavy use when CMS has collected a substantial data sample;
- AOD (*Analysis Object Data*): this is a distilled version of the RECO event information, and is expected to be used for most analyses. More specifically, the AOD data tier contains physics objects: tracks with associated Hits, calorimetric clusters with as-

sociated Hits, vertices, jets and high-level physics objects (electrons, muons, Z boson candidates, and so on). AOD provides a trade-off between event size and complexity of the available information to optimize flexibility and speed for analyses.

The full event data (FEVT) in an Event is the RAW plus the RECO data. The following diagram shows the flow of CMS detector data through the tiers.

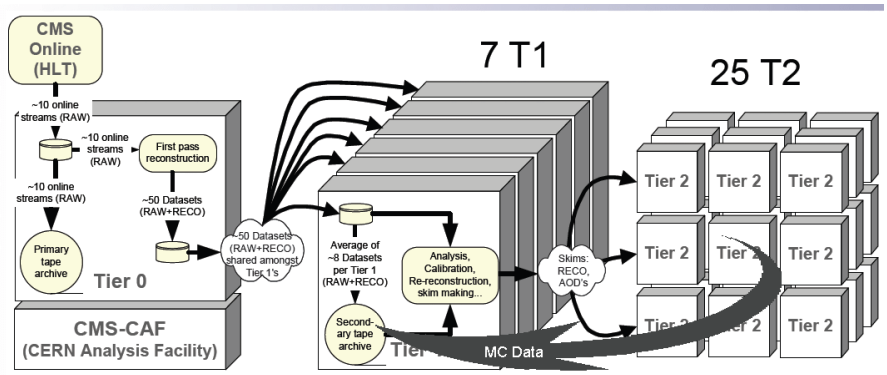

Figure 19: Diagram showing the flow of CMS detector data through the tiers.

Part III

STUDY OF THE NOISE IN THE CMS ECAL

A through understanding of the noise in ECAL is important to provide an accurate reconstruction of the energy oh photons adn electrons in CMS. The performed study of the noise is based upon the flluctuations of the pedestal of all the channels in both the Ecal Barrel and the Ecal Endcap, and it is organized following the symmetry of the detector. This study is also functional to the calibration of the detector with the $\phi - symmetry$ method, which will be important for the startup of the Run II foreseen in 2015.

4

THE CMS ELECTROMAGNETIC CALORIMETER

The CMS Electromagnetic Calorimeter was designed in order to play a significant role in exploiting the physics potential offered by the LHC, concerning the Higgs sector and also a large variety of SM and processes, such as the detection of the $H \to \gamma\gamma$ final state, or other measurements such as cascade decays of gluinos and squarks, important in the studies about supersymmetric particles. The main functions of the calorimeter are to identify and measure precisely the energy of photons and electrons, to measure the energy of jets, and to provide hermetic coverage for measuring missing transverse energy. In addition, good efficiency for electron and photon identification as well as excellent background rejection against hadrons and jets are required. Furthermore a good separation of τ-hadronic decays from normal QCD jets is desired. A large solenoid radius has been chosen to allow the calorimetry to be located inside the solenoid.

ECAL presents important properties: it is compact, with high-granularity and radiation resistant.

The choice of a high-resolution, high-granularity crystals calorimeter increases the ability to observe the physics described above. High density crystals with a small Molière radius allow a very compact electromagnetic calorimeter system: after an intensive initial R&D programme, lead tungstate ($PbWO_4$) crystals were chosen. In fact $PbWO_4$ has a short radiation length and a small Molière radius and it is a fast scintillator.
Figure 20 shows a schematic view of the calorimetry and tracking system.

4.1 LAYOUT AND MECHANICAL DESIGN

The CMS ECAL is a homogeneous and hermetic calorimeter comprising 61200 lead tungstate ($PbWO_4$) scintillating crystals mounted in the barrel (EB), closed by 7324 crystals in each of the two endcaps (EE). A preshower detector (ES), based on lead absorbers equipped with silicon strip sensors, is placed in front of the endcap crystals, to enhance photon identification capabilities. Avalanche photodiodes (APDs) and vacuum phototriodes (VPTs) are used as photodetectors in the EB and EE respectively. The division of ECAL into the three main parts, EB, EE and ES is shown in Figure 21.

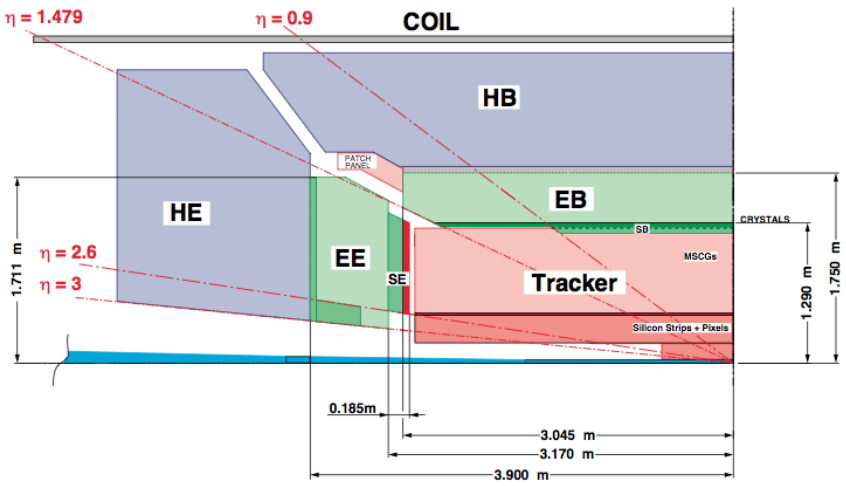

Figure 20: Schematic view of one quadrant of the calorimetry and tracking system.

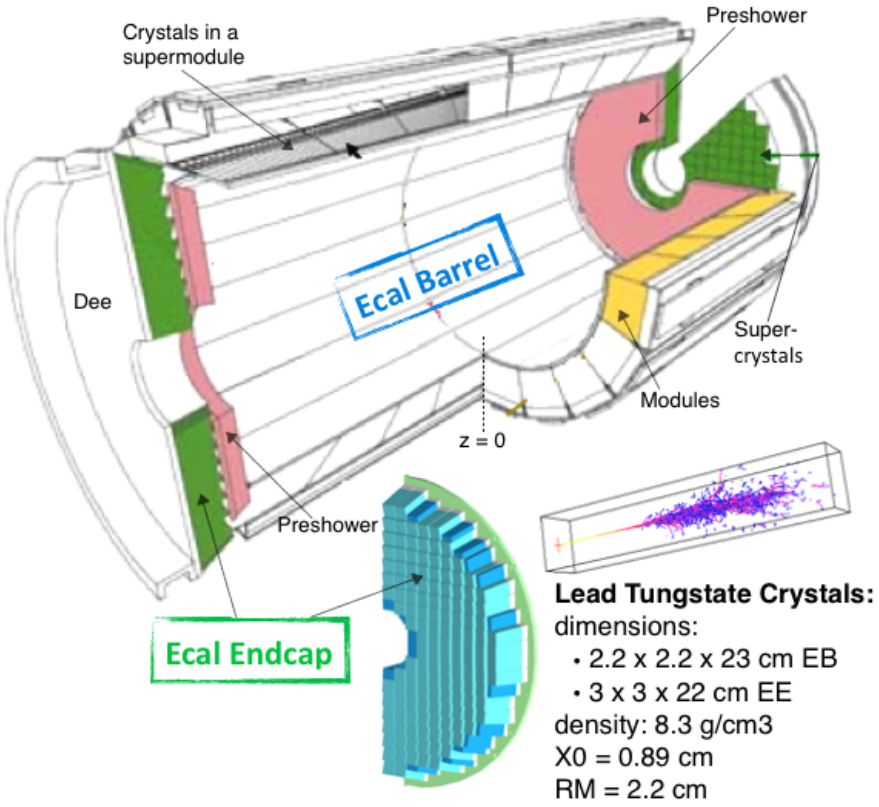

Figure 21: ECAL overall layout.

4.1.1 *ECAL crystals and the* R&D *program*

The lead tungstate crystals forming ECAL are equipped with avalanche photodiodes or vacuum phototriodes and associated electronics oper-

ating in a challenging environment: a magnetic field of 4T, a time of 25 ns between bunch crossings, a radiation dose of $\simeq$ 200 kGy in 10 years and also difficult access to maintenance.
As cited above, after an intensive R&D program lead tungstate crystals were chosen because they offer the best prospects of meeting these demanding requirements. The choice was based on the following considerations:

The working environment of the ECAL crystals is challenging.

- $PbWO_4$ has a short radiation length and a small Molière radius;
- it is a fast scintillator;
- it is relatively easy to produce from readily available raw materials and substantial experience and production capacity already exist in China and Russia.

To be more precise the crystals have a front face of about 22x22 mm^2, which matches well the Molière radius of 22 mm. To limit fluctuations on the longitudinal shower leakage of high-energy electrons and photons, the crystals must have a total thickness of 26 radiation lengths, corresponding to a crystal length of only 23 cm.
A picture of a crystal in ECAL is shown in Appendix A.

Technical properties of the crystals: dimensions and Molière radius; other informations and schemes are shown in Figure 21.

$PbWO_4$ is intrinsically radiation-hard, but non-optimized crystals do suffer from radiation damage. Radiations affect the scintillation mechanism and the uniformity of the light yield along the crystal. Indeed it affects the transparency of the crystals through the formation of color centers and the transport of light is changed by self-absorption of the crystals. This light loss can be monitored by a light-injection system, also called light monitoring system, shown in Figure 22: it is designed to inject light pulses into each crystal to measure the optical transmission. The pulses are distributed via an optical-fibre system. The system is designed to continuously monitor the calorimeter.

The radiation damages in crystals concerning their loss in transparency can be observed considering the reduction in response to the laser monitoring light (see Figure 37).

4.1.2 *The ECAL Barrel*

The barrel part of the ECAL (EB) consists of a cylinder with an average inner radius for crystals of 1290 mm and a pseudorapidity coverage to $|\eta| = 1.479$. It is inserted between the tracker (TRK) and the hadron calorimeter barrel (HB).
The z axis of the ECAL Barrel coincides with the z axis of the CMS detector; it can be divided into two sides, the one with negative values of the z coordinate and the other one with positive values of z. Each side is organized into 85 sections, called *rings*, each identified by the variable η; every single section has a $\phi - granularity$ equal to 360. A crystal in Ecal Barrel is identified with an *id*, which consists of a pair of (η, ϕ) coordinates; the latter is frequently used referring to a specific *channel*.

The η and ϕ granularities are organized in order to identify the single crystals or channels.

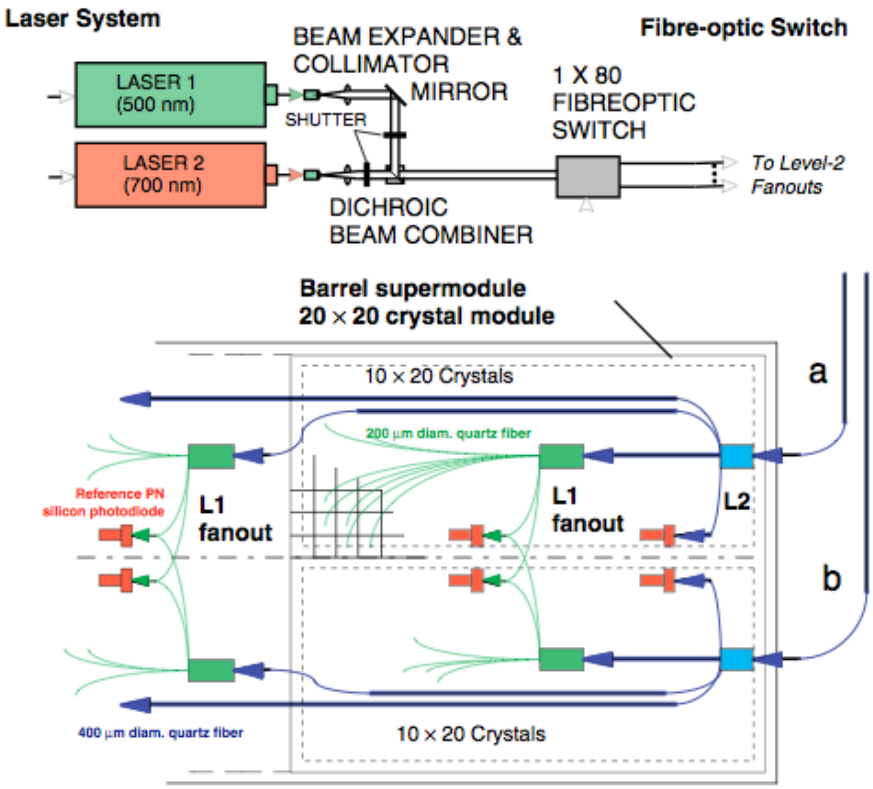

Figure 22: Schematic view if the Light Monitoring System.

Subdivisions are used to classify the geometry of the detector: in fact crystals are organized in 36 supermodules, 18 on each z-side of the CMS detector. Indeed for reasons of ease of construction and assembly, crystals have been grouped by pairs in ϕ and five in η, in the so-called flat-pack configuration (see Figure 23); this group of 10 crystals contained in an alveolar structure forms what is called a *submodule*.

The EB energy resolution depends on a noise, a stochastis and a constant terms.

The ECAL barrel energy (E) resolution for electrons has been measured in beam tests to be:

$$\frac{\sigma_E}{E} = \frac{2.8\%}{\sqrt{E(GeV)}} \oplus \frac{12\%}{E(GeV)} \oplus 0.3\%, \tag{7}$$

where the three contributions correspond to the stochastic, noise, and constant terms. This result was obtained reconstructing the showers in a matrix of 3×3 crystals where the electron impact point on the calorimeter was tightly localised in a region of 4 mm×4 mm to give maximum containment of the shower energy within the 3 × 3 crystal matrix. The noise term of 12 per cent at 1 GeV corresponds to a single-channel noise of about 40 MeV, giving 120 MeV in a matrix of 3×3 crystals. The constant term, which dominates the energy resolution for high-energy electron and photon showers, depends on the non-uniformity of the longitudinal light collection, energy leakage from

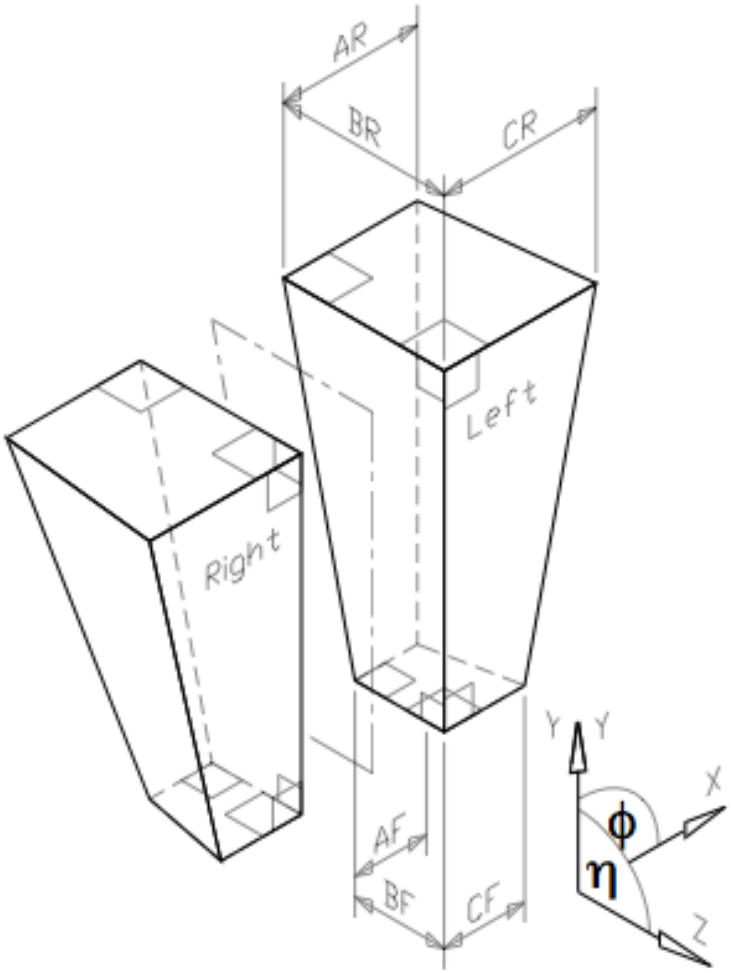

Figure 23: Flat-pack configuration.

the back of the calorimeter, single-channel response uniformity and stability.

4.1.3 *The endcap calorimeter*

The endcap part of the crystal calorimeter covers a pseudorapidity range from 1.48 to 3.0. The design of the endcaps provides precision energy measurement to $|\eta| = 2.6$.
Each Ecal Endcap is constructed from around 14000 crystals of Lead Tungstate which are arranged as 5x5 arrays in Carbon Fibre structures to form supercrystals. One important feature of the ECAL Endcaps is that all crystals are identical and mechanically there are only two types of full-sized supercrystals, although some partial supercrystals are also needed to give the required coverage. The supercrystals are arranged as in Figure 24 to form Dees and then two Dees form an

endcap: supercrystals in adjacent quadrants are rotated through 90° with respect to each other.

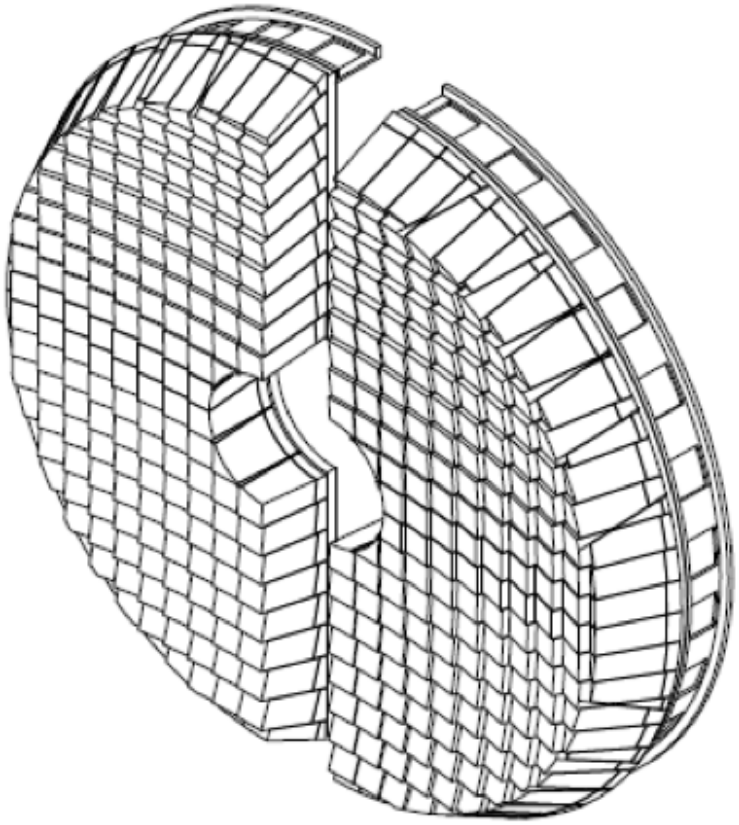

Figure 24: Dees view in Ecal Endcap.

The Figure 25 shows a schematic representation of the two halves of the ECAL, viewed from the interaction point, showing the location and numbering of the supermodules in the barrel and the dees in the endcap.

The main requirement for a numbering scheme for simulation is that navigating between adjacent crystals and supercrystals should be straightforward. Since the crystals are arranged, to a good approximation, on an x-y grid the natural system is to use an (x,y) numbering scheme and only the origin of the system and the direction of the axes need to be defined. The direction of the x and y axes are chosen to be the standard CMS axes but the indexing is arranged such that the integer x and y coordinates may be used directly to access array elements i.e. The indexing runs from 1-100 for the crystals and 1 to 20 for the supercrystals. The numbering of the supercrystals is illustrated in Figure 26 and the inset shows how to determine the crystal number in a given supercrystal.

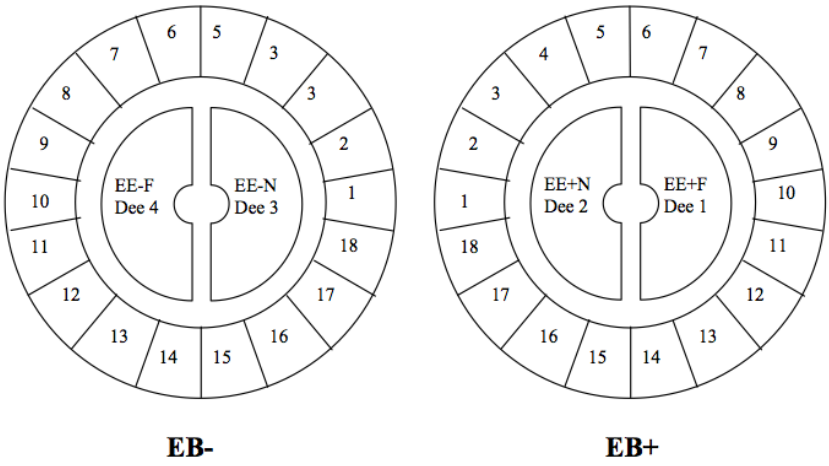

Figure 25: Ecal geometry

4.1.4 *The preshower detectors*

CMS utilizes a preshower detector in the endcap region (rapidity range $1.65 < \eta < 2.6$) mainly to provide $\gamma - \pi^0$ separation. The preshower detector contains two thin lead converters followed by silicon strip detector planes placed in front of the ECAL, as shown in Figure 27.

The measurement of the energy deposition in the $\simeq 2$ mm pitch silicon strips allows the determination of the impact position of the electromagnetic shower by a charge-weighted-average algorithm with very good accuracy ($\simeq 300$ μm at 50 GeV). The fine granularity of the detector enables the separation of single showers from overlaps of two close showers due to the photons from π^0 decays.

As shown in Figure 28 the active planes of silicon detectors are built from a large number of identical modules each of which contains an individual detector. A module contains an aluminum tile onto which a ceramic support is glued. A silicon detector, subdivided into 32 strips at 1.9 mm pitch, is then glued and bonded to the ceramic. The hybrid containing the analog front-end electronics is also glued and bonded to the ceramic. The modules are then assembled on long ladders which contain two columns of adjacent detectors.

The π^0 rejection algorithm using the preshower compares the highest signal (summed in 1, 2 or 3 adjacent strips) with the total signal in 21 adjacent strips centered on the highest-signal strip. The fraction of the two energies, F, is then used to select photons (and reject π^0 's).

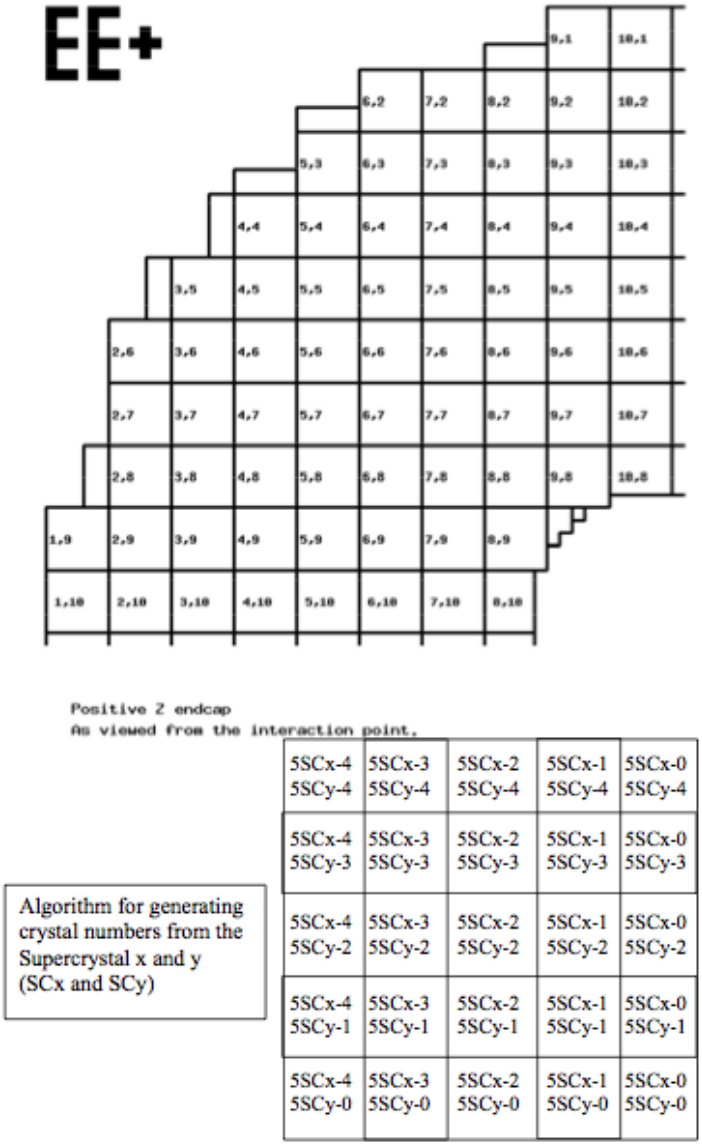

Figure 26: Crystal numbers in a given supercrystal.

4.2 READOUT ELECTRONICS

The scintillation light from the crystals must be captured by a photodetector, amplified and digitized. A schematic of the readout sequence is shown in the Figure 29.

The first element is the $PbWO_4$ crystal which converts energy into light. The light is converted into a photocurrent by the photodetector. The relatively low light yield of the crystal necessitates a preamplifier in order to convert the photocurrent into a voltage waveform. The signal is then acquired and digitized. The amplification, shaping and digitization of the signal are done through a dedicated system, con-

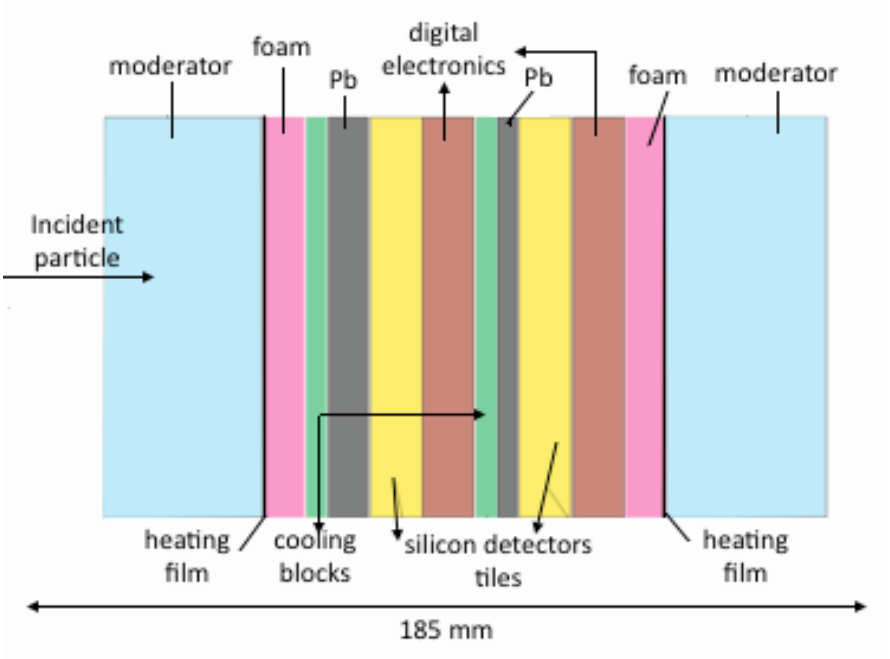

Figure 27: The preshower detector

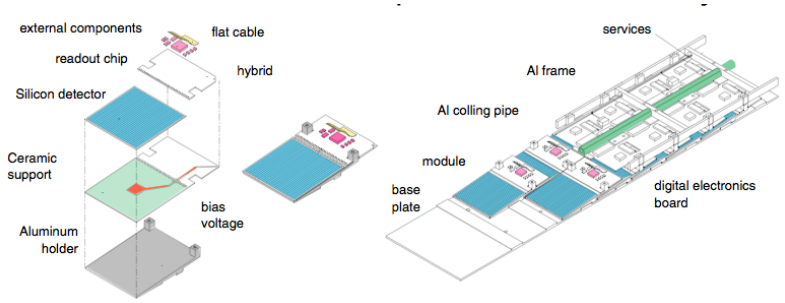

Figure 28: The preshower detector silicon strips

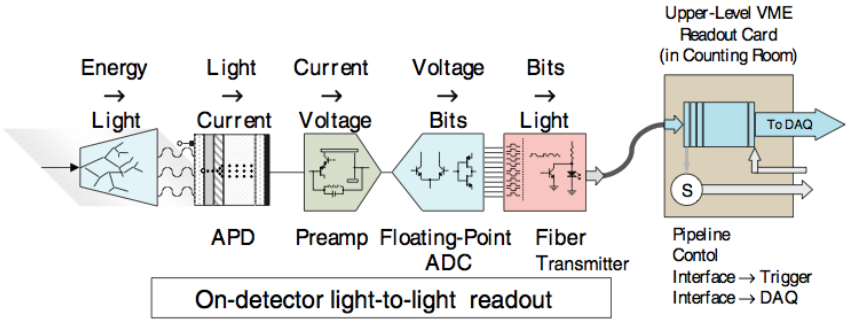

Figure 29: The ECAL readout chain.

sisting in the Very-Front-End cards (VME). The readout chain just described forms the so called *on-detector front-end electronics*, located

inside CMS; its resulting data are transported via optical fibers to the *off-detector electronics* and then to the Data Acquisition system (DAQ). The *off-detector electronics* is located outside the detector in the service underground cavern. More detatails about the single steps in the *on* and *off* readout follow.

4.2.1 *The Avalanche Photodiode (APD) and its noise contribution*

The APD follows immediately the crystal in the on-detector electronics.

The APD is the photodetector used in the readout electronics in EB. Its schematic representation is shown in Figure 30: photons convert in the p^{++}layer; photoelectrons drift towards the abrupt p-n junction where ionization starts and avalanche break-down occurs. The avalanche breakdown results in impact electron multiplication.

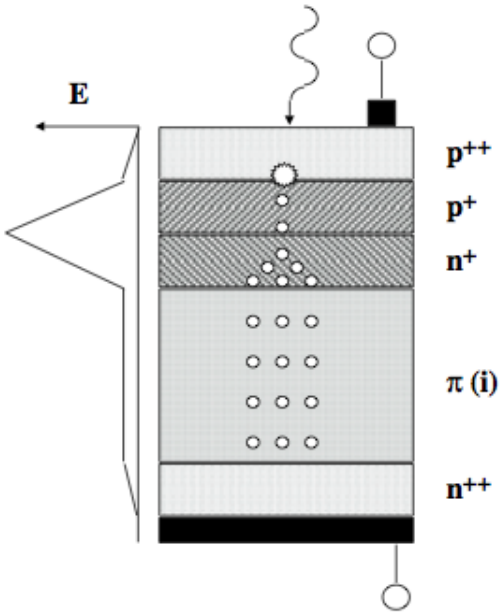

Figure 30: Schematic view of the APD.

The APD is directly connected to the crystal, as shown in Figure 31.

Studying the electrical properties of the APD the main sources of noise can be found.

Some parameters of the APD influence the entity of the signal in terms of the noise. From the electrical design point of view, the APD is characterized by:

- *electrical device parameters*: the terminal capacitance (C) and the series resistance (R_S);
- *operational parameters*: they consist in the value of the electron gain (M) and in the surface, bulk and amplified bulk leakage currents, before and after irradiation.

If σ_M is the r.m.s. variation of the gain for a single photoelectron when the APD operates at a gain M, the variable F, called *excess noise*

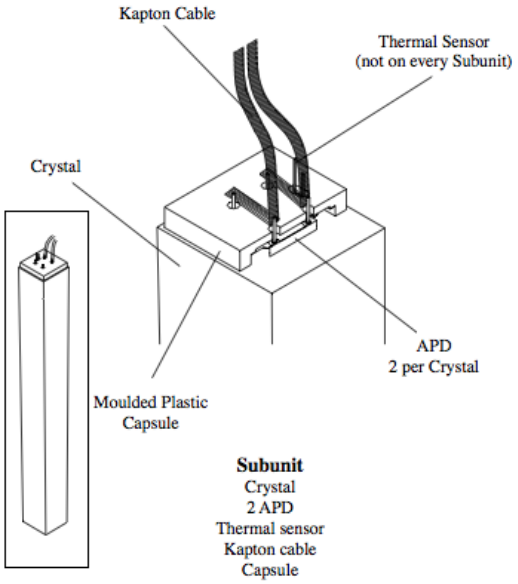

Figure 31: The crystal subunit: it consists of the crystal and the capsule assembly; the latter one present the APD and the thermal sensor for the crystal.

factor, can be defined as $F^2 = 1 + (\sigma_M^2/M^2)$: it modifies the photostatistics contribution to the overall resolution because it affects the number of electrons presented to the preamplifier as a function of the incident amount of light, and the gain. If the intrinsic detector resolution for a sum of n crystals is written as $a/\sqrt{e} \oplus c$, where a is the stocastic term and c is the constant term (including all calibration errors), the the effective stocastic term becomes $\sqrt{a^2 + \frac{F}{N_{pe}}}$, where N_{pe} is the number of photoelectrons per MeV; so including electronic noise the ECAL energy resolution in the barrel becomes:

The noise from the APD affects the ECAL energy resolution.

$$\frac{\sigma_E}{E} = \frac{a^2 + \frac{F}{N_{pe}}}{\sqrt{E}} \oplus c \oplus \frac{\alpha(C + C_0)}{ExMxN_{pe}} \oplus \frac{\beta\sqrt{I_s + M^2 F I_b}}{ExMxN_{pe}}, \tag{8}$$

where C is the APD capacitance and C_0, α and β are parameters that depend on the preamplifier, shaping, and manner of signal acquisition; I_s is the surface current, I_b the bulk one. For CMS M is be somewhere between 20 and 100.

The leakage current, typical of the silicon detectors, plays the main role in the ECAL noise.

As the equation above indicates, leakage current can play an important role in the noise. Leakage currents cause noise because the number of electrons arriving at the preamplifier per unit time has a (Gaussian) variation, thus the noise is proportional to $\sqrt{I}$. The leakage current receives contributions principally from the electrons that flow directly from the anode to the cathode, without undergoing any amplification and from the electrons generated at the photocathode, which undergo full avalanche multiplication.

4.2.2 *The Very-Front-End Electronics*

The signals from the photodetectors (Avalanche Photodiodes (APDs) in the barrel region and Vacuum Phototriodes (VPTs) in the end-cap regions) are amplified, shaped and digitized by the Very-Front-End cards (VFE). The readout electronics of ECAL contains about 16.000 VFE cards.
A VFE card, designed in 0.25 µm CMOS radiation hard technology, comprises five identical and independent read-out channels which process the signal from five crystals simultaneously, as shown in Figure 32 and Figure 33. Each channel has a Multi Gain Pre-Amplifier (MGPA) and a four channel ADC followed by LVDS to CMOS level-converters (LVDS RX) [9].

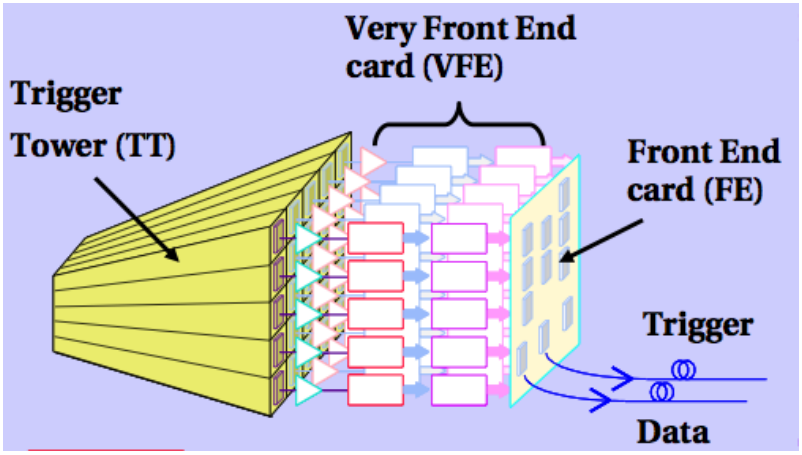

Figure 32: Overview on the VFE and the readout system.

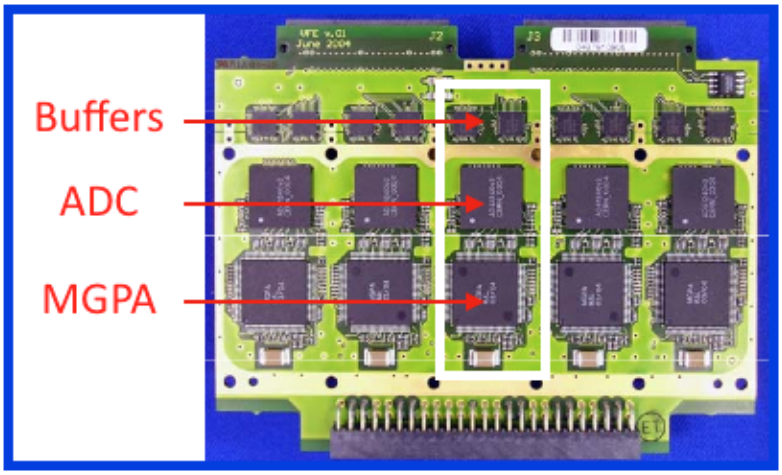

Figure 33: Very Front End card.

A schematic view of the operation of a VFE card is reported in Figure 34: the signals are pre-amplified and shaped and then amplified by three amplifiers with nominal gains of 1, 6, and 12, covering a dynamic range of 60 pC. The shaping is done by a CR-RC filter with a shaping time of 40 ns. The output pulse non-linearity of the MGPA is less than 1 %. Its noise, in the Barrel case, is about 8000 electrons for gain 6 and 12, and about 28000 electrons for gain 1. The MGPA contains three programmable 8-bit Digital To Analog Converters (DACs) to adjust the output signal levels to the ADC inputs.

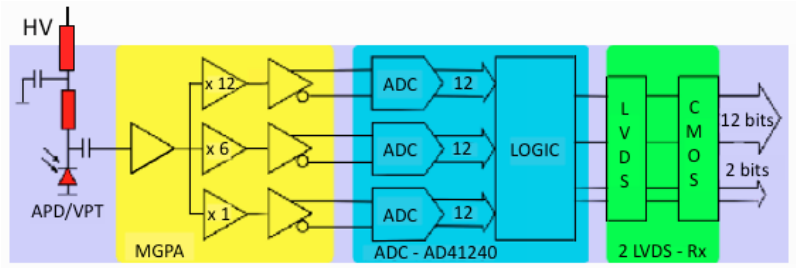

Figure 34: Schematic view of the Very Front End card.

The 3 analog output signals of the MGPA are digitized in parallel by the 40 MHz 12-bit ADC. Digital logic internal to the ADC determines whether a gain is saturated and then outputs the data from the highest non-saturated gain. A Detector Control Unit (DCU) measures the leakage currents of the five Avalanche Photo Diodes and the crystal temperature.

4.2.3 *Sampling of the pulse shape*

The analog signal from the preamplifier is converted into a digital signal trought the 40 MHz ADC. The pulse shape is formed with ten conseutive digitizations, as shown in Figure 35; in order to study the noise the first three samples (pedestal) are considered; indeed, they are multiplied with the ADCToGeV factor (in order to convert them from their ADC value to GeV), the Intercalibraton Constant and the Laser Correction factor. The latter one concerns the loss of the transparency in crystals due to the radiations. The analysis of the pedestal and the study of the noise is described in details in Chapter 5.

Figure 36 reports the evolution of the leakage current of the APDs, while Figure 37 shows the transparency loss in EB and EE.

4.2.4 *ECAL Off-Detector Electronics*

Located between the on-detector front-end electronics and the global data acquisition system (DAQ), the off-detector electronics of the CMS electromagnetic calorimeter (ECAL) is involved in both detec-

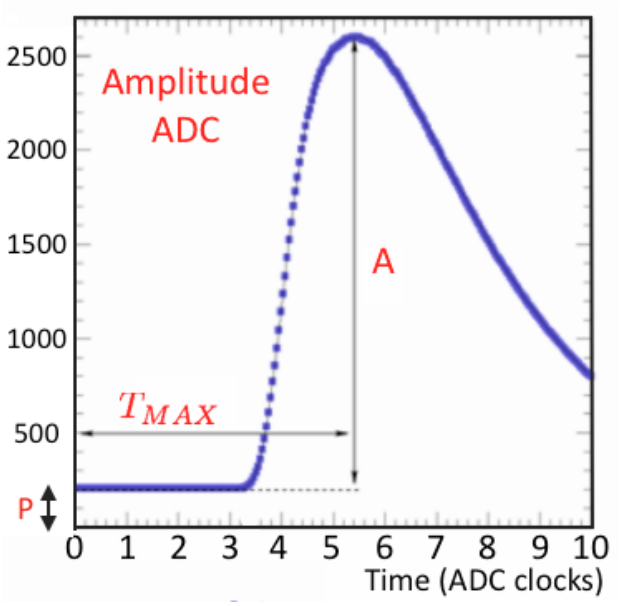

Figure 35: Pulse shape formed after ten consecutive digitizations of the ADC.

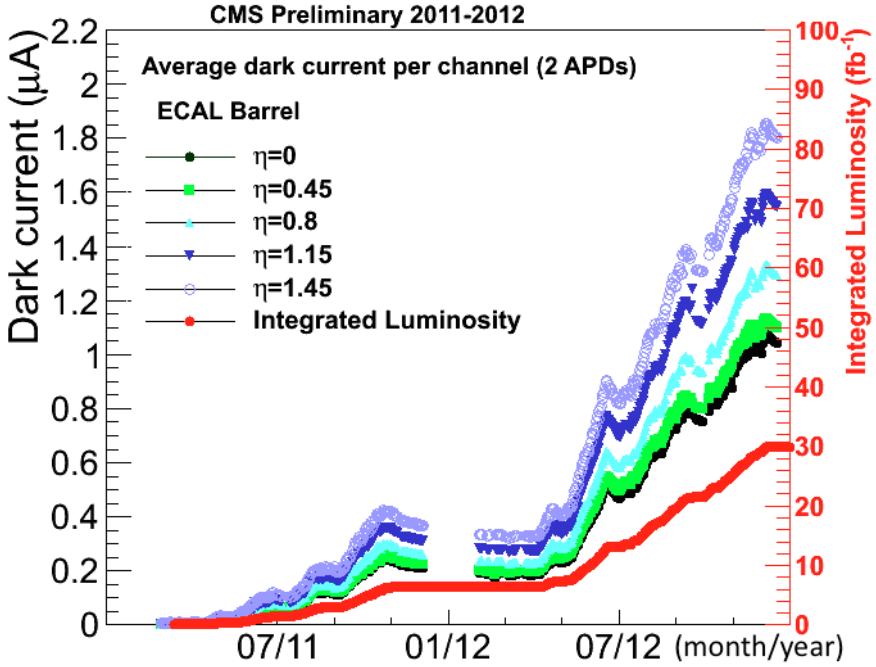

Figure 36: APD leakage current.

tor readout and trigger system. Working at 40 MHz, the trigger part, within 10 clock cycles, must receive and deserialise the data of the front-end electronics, classify them and send them to the readout part.

The information from the electromagnetic calorimeter is used by the

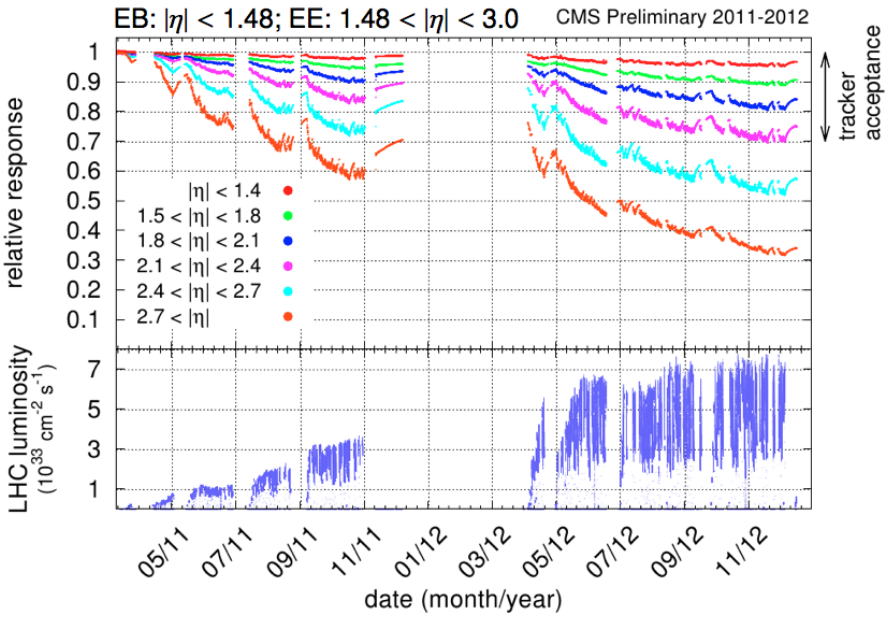

Figure 37: Response to laser light. An average is shown for each pseudorapidity range. The bottom plot shows the corresponding instantaneous luminosity.

level one trigger (LV1) together with the hadronic calorimeter and the muon subdetector information. The information used for the LV1 decision are called *trigger primitives*. A trigger primitive consists of the evaluated transverse energy deposited in a trigger tower and of a single bit qualifying the energy deposit expansion along η.
The general ECAL read-out architecture is represented in Figure 38. One Very Front-End card (VFE) reads five crystals and five of these cards are plugged into one Front-End card (FE). The clock is distributed to the front-ends through token rings controlled by the Clock and Control System cards (CCS). The FE cards compute trigger primitives and send them at 40 MHz to the Trigger Concentrator Cards (TCC) through dedicated serial links. The TCCs finalise the trigger primitive calculation after synchronisation and serialisation done by the Synchronisation and Link mezzanine Board (SLB), send them to the Level 1 trigger system.
The trigger is distributed to the front-end electronics, to the TCCs and to the Data Concentrator Cards (DCC) by the CCS cards. The DCCs provide access to the data via the VME bus. This access is used by the local DAQ and the laser-based ECAL calibration system.

4.3 CALIBRATION AND ANALYSIS

ECAL calibration is necessary to make the uniform the response from all channels and then provide for absolute energy measurements. The

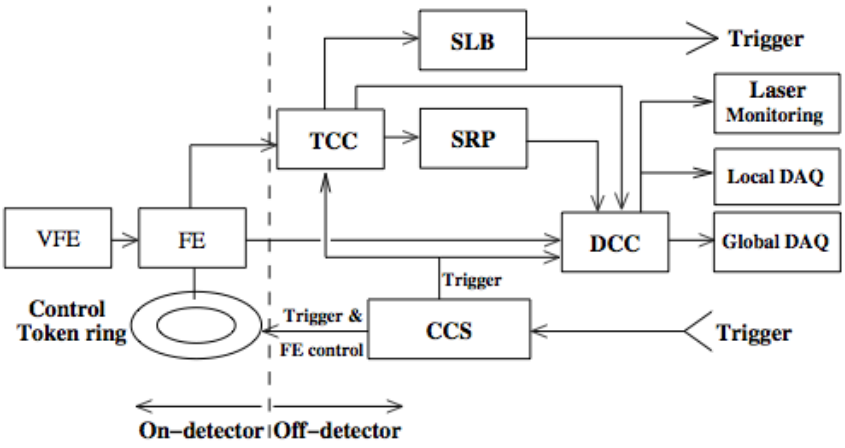

Figure 38: ECAL readout and trigger architecture.

The ECAL calibration is necessary to make uniform the response from all the channels. Geometrically speaking, there are two types os calibration: intercalibrations and absolute calibrations. From the operational point of view there are two levels of calibration: the pre-calibration procedure and the calibration done with collision data. The latter one can use three different methods, where the $\phi - \mathrm{symmetry}$ *method is included.*

ECAL channels are calibrated in two steps, by using *relative* and *absolute calibrations*. Relative calibrations, C_i, between one channel and another, are referred to as intercalibrations. Absolute calibrations are obtained by referring the intercalibrations to a mass scale by using Z-boson decays. The intercalibration constants in EB and EE are divided by their average value and so normalized to unity. A number of methods are used for intercalibration and are then combined to provide a weighted mean intercalibration constant for each channel. An initial set of calibrations, known as the *pre-calibration*, was obtained from laboratory measurements, beam tests, and from exposure to cosmic rays. The laboratory measurements included the crystal light yield and photodetector gain. Calibration with collision data involves the following methods:

- the ϕ-symmetry method is based on the expectation that, for a large sample of minimum bias events, the total deposited transverse energy should be the same in all crystals at the same pseudorapidity. In CMS this corresponds to crystals located in a particular η ring. The method provides a fast intercalibration of crystals located within the same ring;
- the π_0 and η calibrations use the invariant mass of photon pairs from these resonances to calibrate the channel response;
- calibrations with isolated electrons from W- and Z-boson decays are based on the comparison of the energy measured in ECAL to the track momentum measured in the silicon tracker.

The ϕ-symmetry method is used to intercalibrate channels at the same pseudorapidity. Isolated electrons are also exploited to derive the relative response of the various η rings. The precision of the intercalibrations has been validated using the pre-calibration data and

by a channel-by-channel comparison of the intercalibrations derived with each method.
The analysis described in Chapter 5 is strictly connected to the ϕ-symmetry method, which is now described.

4.3.0.1 *ECAL calibration with the ϕ-symmetry method*

The intercalibration in ϕ is taken from the ratio of the total transverse energy deposited in one crystal to the mean of the total transverse energy collected by all crystals at the same value of η. Events used for this calibration are acquired with a special minimum bias trigger. All single-crystal energy deposits above 150 MeV in EB, and above 650 MeV in EE are recorded, while the rest of the event is dropped to limit the usage of the trigger bandwidth. The data analysis is restricted to deposits with transverse energies between a lower and an upper threshold. The lower threshold is applied to remove the noise contribution and is derived by studying the noise spectrum in randomly triggered events. It is set to about six times the channel RMS noise (e.g. 250 MeV for channels in EB). The upper threshold is applied to minimize the fluctuations induced by rare deposits of very high E_T and is set to 1 GeV above the lower threshold, in both EB and EE. Because the transverse energy scalar sum is obtained from a truncated E_T distribution, a given fractional change in the E_T sum does not correspond to the same fractional change in the value of the intercalibration constant. This is accounted for with an empirical correction. Corrections are also applied to compensate for known azimuthal inhomogeneities of the CMS detector, related to the inter-module gaps in the ECAL and to the tracker support system.

Relationship between the estimation of the noise in ECAL and the determination of the thresholds for the $\phi-\mathrm{symmetry}$ method.

4.4 ECAL SOFTWARE IN CMSSW

DETID OBJECTS Each component of the CMS detector, ranging from one subdetector (HCAL, TK et cetera) to one of its component (e.g. a crystal of ECAL, a supercrystal in the ECAL barrel) is identified by a dedicated data type called a DetId object.

A DetId holds, among its data members, a 32-bit unsigned integer which uniquely identifies each part of CMS. Together with the 32-bit unsigned integer, the DetId has methods which provide different sets of coordinates pertaining to CMS sub-portion being considered, for instance the *iphi* or *ieta* of a given ECAL barrel crystal. The most significant bits identify the subdetectors of CMS, while the following bits refer to parts within the subdetectors, as shown in the Figure 39.

Structure and composition of the DetId object.

Within the electromagnetic calorimeter, the subdetectors are identified as follows: Ecal Barrel (EB), Ecal Endcap (EE), Preshower (ES), EcalTriggerPrimitives (the trigger data produced summing the transverse energy of the crystals in a trigger tower).

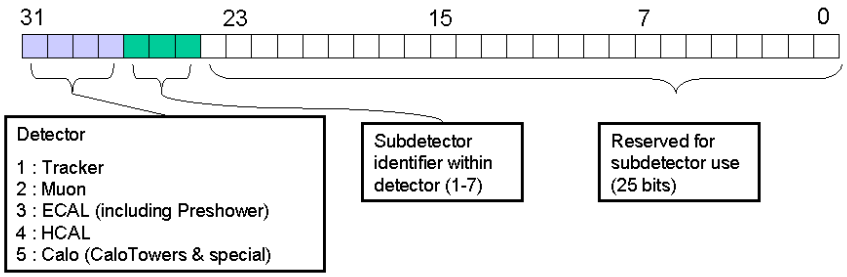

Figure 39: Distribution of the informations into the DetId type.

The DetIds of the calorimeters, ECAL and HCAL, have been designed to match the topology of the detector in a natural and useful way, using polar (*ieta/iphi*) or cartesian (x/y) coordinates as appropriate. The ecal barrel (EB) is an *eta/phi* grid with the ranges [-85,+85] for IETA (with no crystals at IETA = 0) and [0,360] in PHI. The ecal endcap is represented by an X/Y grid, where X and Y run from 1 to 100; many X/Y pairs don't map to any existing crystal since the centre of the endcap is void to admit the beampipe and since the endcap has a circular profile while the used coordinates naturally describe a square.

The ECAL barrel is divided in two parts along the CMS z direction (parallel to the beamline): the positive (EB+) and negative (EB-) part of the barrel. Both such halves are divided in 18 *phi* wedges covering 20 degrees, each wedge being named with an integer following the EB+ or EB- prefixes (EB+07, EB-11). Such wedges, referred to as supermodules, have been built all the same and represent one readout unit from the data acquisition point of view. Each of the two ECAL endcaps consist of two halves separated by a vertical sect, each half being referred to as one Dee. Each endcap is subdivided in 9 readout sectors.

Often ECAL channels are also identified using an index which is local to the readout unit. Commonly used, in the case of the Ecal Barrel (EB), is the crystal number *ic*, which ranges from 1 to 1700 inside each of the 36 supermodules of the barrel, together with an index which identifies the supermodule.

DATA TIERS WITHIN THE CALORIMETRY SOFTWARE The data read from the detector and Monte Carlo data are both stored in five layers within the ECAL software, each representing a different step in the heirarchy of the reconstruction. This is illustrated in the diagram in Figure 40, and explained in more detail below.

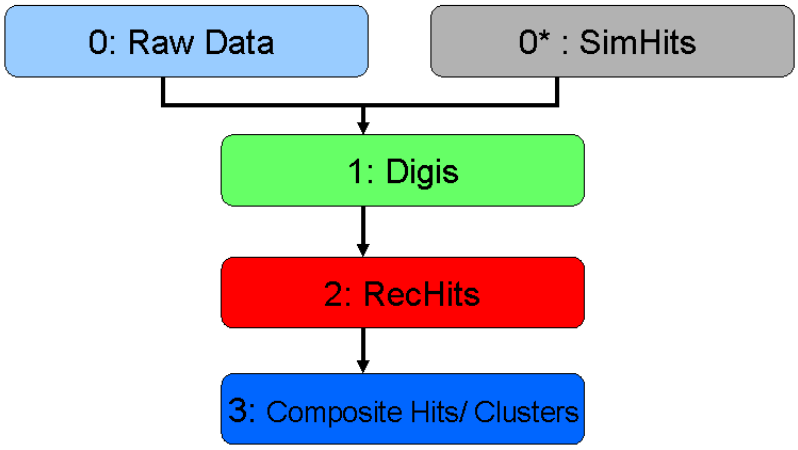

Figure 40: ECAL software layers heirarchy.

Data Layer 0 - The RAW data
All of the CMS detector components use the same class (FEDRawData) to hold the raw data which is read out from each FED (Front End Digitizer). Each subdetector in CMS has multiple FEDs: ECAL has 54, 9 in each endcap and 36 in the barrel. The raw data can be seen as an array of formatted 64-bit unsigned integers which are read from the detector front end electronics and saved to persistency by the data acquisition (DAQ) system. Looking directly at the hexadecimal codes of the raw data is useful to the experts when there are problems with the readout which violate the data format rules. For usage of most of the people, the raw data is parsed and converted into *digis* (Layer 1 objects) in the RawToDigi (or unpacking process).

Monte Carlo Layer 0 - Sim Hits (SimDataHit/CaloHit objects)
The simulation process begins with an event generator followed by the Geant-based simulation of the interactions between the particles and the detector. The output of the simulation is a set of simulated energy deposits (with deposit times) in detector channels. These energy deposits are stored in the event as *SimHits*. The SimHits are labelled by DetIds and are analogous to real data *RAW data*. SimHits are converted into *digis* in the electronics simulation or *digitization process*. In order to simulate the pileup at CMS, the digitization process can superimpose to the generated events SimHits from *minimum-bias* previously generated.

Layer 1 - Digis
Digis are the per-channel data from the detector. Each is labeled by a DetId. For the crystals in EB and EE, a digi is a set of ADC readings

Digis, the data from the single channels in ECAL, are used to reconstruct the pulse shape and then to study the energy deposits and the noise in the calorimeter. So they play an important role in the analysis in Chapter 5.

for a given event. In normal conditions, there are 10 time samples for each of the channels which are readout: 3 readings before the triggered bunch-crossing and 7 readings containing the maximum pulse. Each sample consists of an ADC word (12 bits) and to bits used to encode the gain (x12, x6 and x1 are the gains available). Digis show the pulse shape of the detector and are used to reconstruct the energy and time of the hit in the calorimeter.

Layer 2 - UncalibratedRecHit

UncalibratedRecHits are used to store the quantities reconstructed starting from the digis (each UncalibratedRecHit is identified by the same DetId as the digi it comes from). For ECAL the quantities are four: amplitude (the peak of the pulse shape), pedestal (the baseling), jitter (the time when the maximum of the pulse shape occurs) and χ_2. There are different algorithms to produce UncalibratedRecHit's which will be described in the following.

Layer 3 - RecHits

RecHits are obtained from UncalibratedRecHits by applying a global scale factor ADCtoGeV which turns the ADC counts into GeV and by applying the calibration constants.

Layer 4 - Composite Hits or Clusters

These are the first stage of higher level reconstructed objects which are built combining groups of detector objects identified as coming from the same physics object. These are the objects used in basic data analysis projects, examples being EcalClusters (built from a group of RecHits) or CaloTowers, which combines ECAL and HCAL RecHits.
.

5

STUDY OF THE NOISE IN ECAL

The method used here for the estimation of the noise in Ecal follows the principles on which the ϕ-simmetry calibration method is founded. The ϕ-simmetry calibration method, described in Chapter 4, is based on the expectation that the total deposited transverse energy (E_T) should be the same in all crystals at the same pseudorapidity, that is in all crystals located in a particular η ring. Following this basic concept idea, the analysis of the noise in Ecal was conducted in order to estimate the noise for all crystals in a particular η ring, covering all the rings both in Ecal Barrel and in Ecal Endcap. In other words the particular geometry of Ecal is the starting point for the determination of physics observables, here in particular of the noise.

5.1 DESCRIPTION OF THE METHOD

The strategy conceived for the estimation of the noise in ECAL starts from the analysis of the data type digis per ECAL channel and then proceeds following the η-granularity of the detector.

To reach these purposes an algorithm was implemented in order to analyze a set of data (dataset) of type *digi* for a certain number of events[1]. At each event a crystal is identified throught its *id*; then the parameters which describe its location, η and ϕ, are obtained: the *channel* of the crystal is defined with the couple (η, ϕ). The process goes ahead extracting from the channel *id* the first three samples of the pulse shape, which form the pedestal, and then obtaining the relative calibration and correction factors; these factors are, more precisely, the *laser correction factor* (L), the *intercalibration constant* (IC) and the *ADCToGeV* factor (A). The latter is necessary to convert the signal from ADC counts to GeV. At this point each sample (s) is multiplied by these factors and the following values are obtained:

$$s = sample \times A \times IC \times L. \tag{9}$$

Once all events are processed as described above, the distributions of the observable s for each channel both in Ecal Barrel and in Ecal Endcap are studied; an example is shown in Figure 41; these distributions are called *Sample Distributions*. Starting from them, the variable of interest now is the σ calculated from their fit with a gaussian Probability Density Function (PDF); in fact the σ represents and quantifies how the signal fluctuates in each channel: the size of this fluctuation corresponds to the noise.

After the gaussian fit of the *Sample Distributions*, the distributions of the σ (noise) for each η ring, called *Noise Distributions*, are created

1 The type *digi* is described in detail in Chapter 4, at pages 61-62.

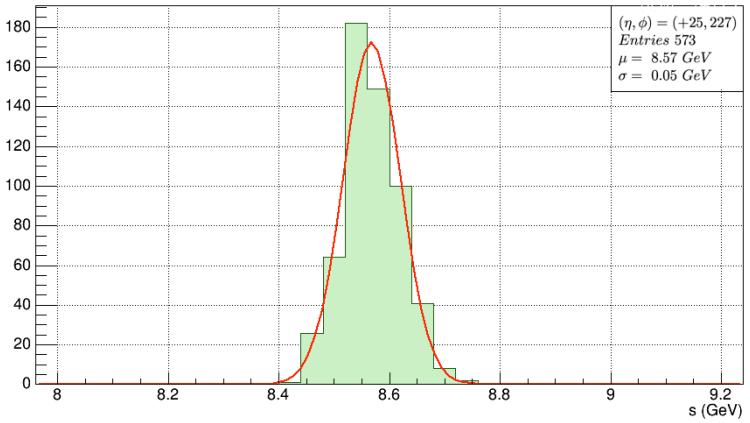

Figure 41: Sample Distribution for the channel (η, ϕ)=(+25,227) in Ecal Barrel (top) and for the channel (x,y)=(+23,90) in Ecal Endcap (bottom).

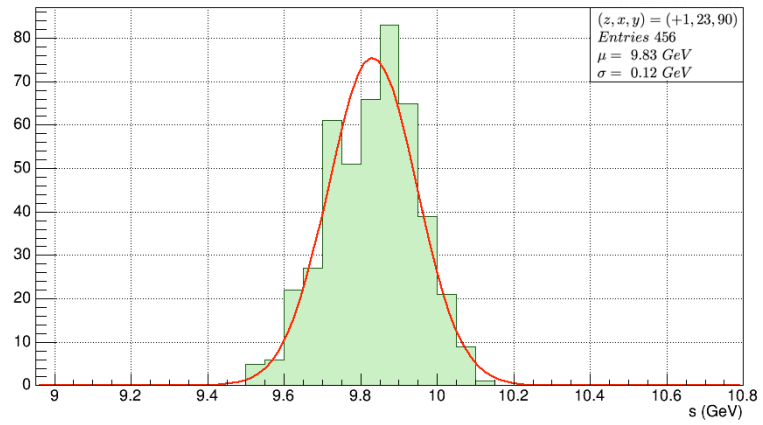

Figure 42: Sample Distribution for the channel (x,y)=(+23,90) in Ecal Encap.

and studied, in order to estimate a value of the noise which mediates the fluctuations of the signal in all crystals in the same ring. Examples of *Noise Distributions* are shown in Figure 43 and Figure 44. The value of the noise averaged on all crystals in each ring will be the mean of these distributions; the fluctuation of the noise will be the rms. Figure 45 shows an example of the trend of the noise in Ecal Barrel, obtained with the method just described, as a fluctuation in pseudorapidity.

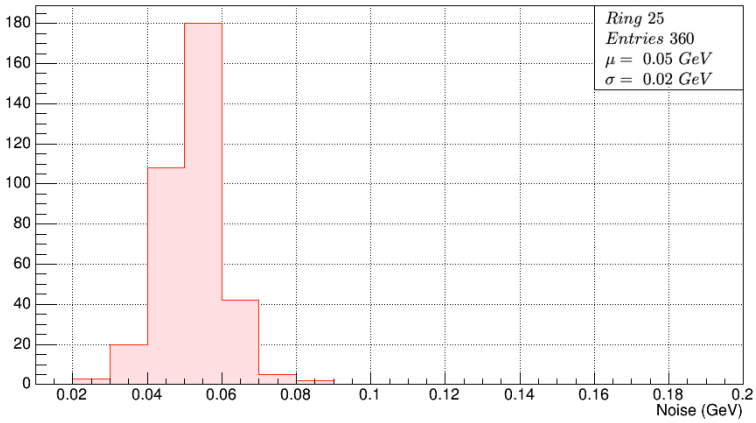

Figure 43: Noise Distribution for the ring 25 in Ecal Barrel.

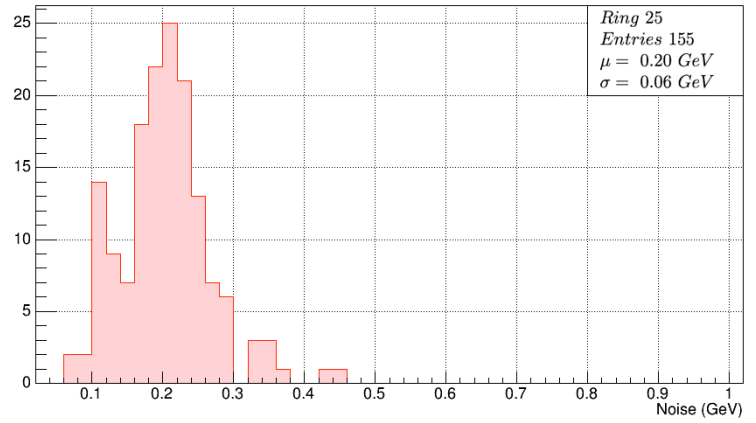

Figure 44: Noise Distribution for the endcap ring +25 in Ecal Endcap.

5.2 ESTIMATION OF THE NOISE

The results from the analysis of the noise in Ecal follow. The data are from the 2012 Run, divided into four periods which globally cover the entire year: Run A, Run B, Run C and RunD. Only the results in GeV for Run A and the comparison between all runs are shown. To view the single results for the other runs and also in ADC counts, see Appendix B.

Results from the analysis described above in both EB and EE.

5.2.1 *Results for Ecal Barrel*

OBSERVATIONS In Figure 46 the trend of the noise in EB+ is symmetric with the one in EB-. Some points express a value of the noise which is very far from the common trend of the noise in the other

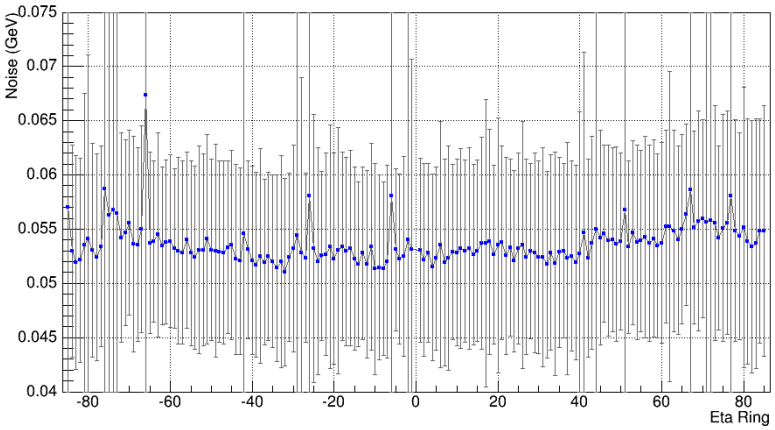

Figure 45: EB Noise in GeV, Run B.

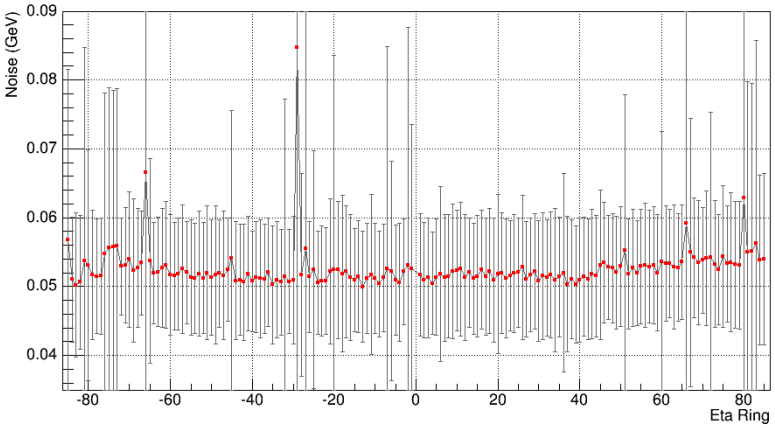

Figure 46: EB Noise in GeV, Run A.

channels. The ring number -29 can be considered as an example: since the relative noise is the average of the fluctuations from all crystals in this channel, a great value of the noise there is due to the presence of one or more crystals which are noisier than the others; in fact, as can be seen in Figure 47, there are crystals with noise between 3.0 and 3.5 GeV, so the average of the noise in the channel is shifted to an higher value than the mean of the other channels. In Figure 48 the trend of the noise for all runs in the entire Ecal Barrel is shown: it grows with the increase in pseudorapidity and during time. In fact the radiation, which gives a significant contribute to produce the noise, grows in regions with high pseudorapidity and increase with time: as it grows, the noise grows, too. The increase of the noise is also due to the enhancement of the leakage current in the APDs, whose trend is shown in Figure 36, and to the growing trend of the laser corrections in time;

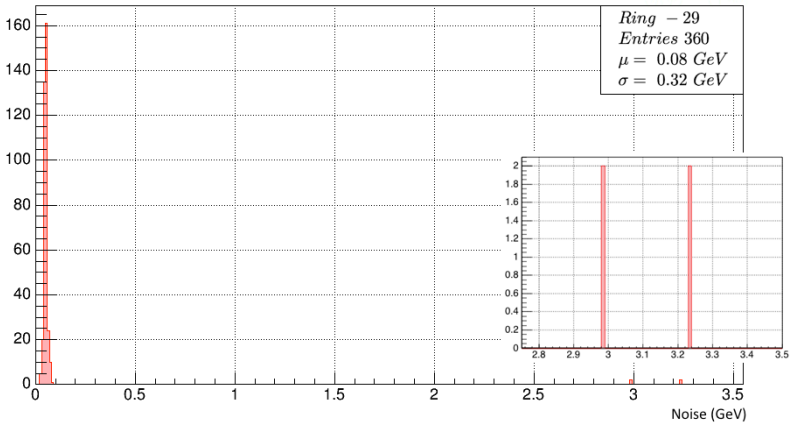

Figure 47: Noise crystals in η ring -29 in Ecal Barrel.

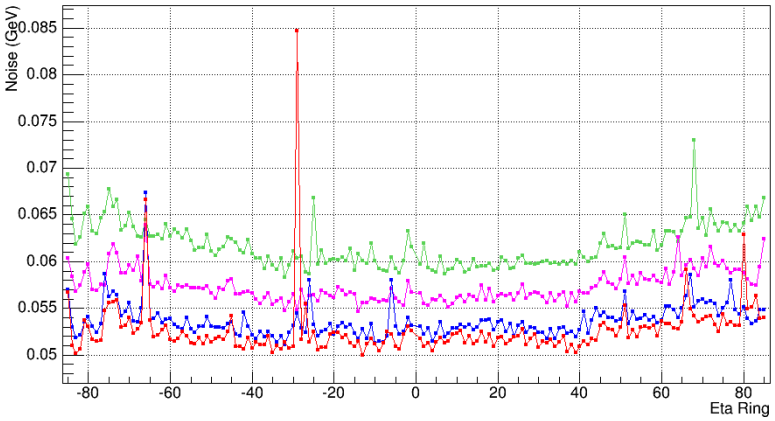

Figure 48: EB Noise in GeV. *Colors Legend:* red for Run A, blue for Run B, magenta for Run C, green for Run D.

in the matter of it Figure 37 shows the loss in transparency of crystals observed measuring their response to the laser light in time.

5.2.2 *Results for Ecal Endcap*

OBSERVATIONS In Figure 49 the trend of the noise in EE+ is symmetric with the one in EE-; each Ecal Endcap is organized in 39 rings, but only the first 30 are shown ($\eta < 2.4$): this is due to the fact that the rings at higher pseudorapidity contain few crystals and the statistical uncertainty on the noise increases dramatically. As observed for the Ecal Barrel, also in Ecal Endcap the trend of the noise increases with the pseudorapidty and during the time, as shown in Figure 50.

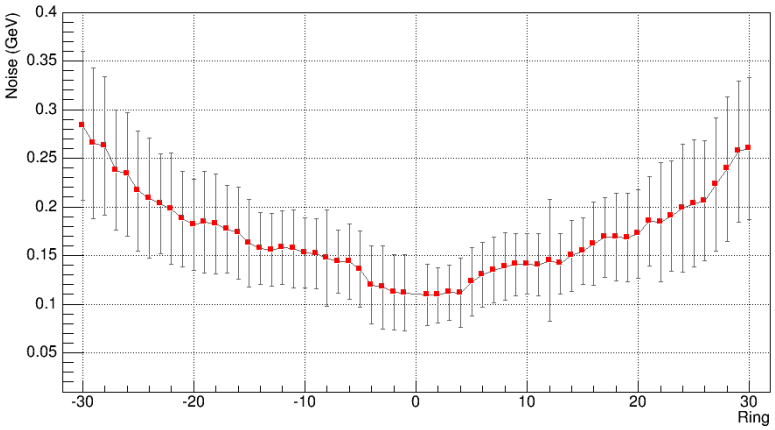

Figure 49: EE Noise in GeV, Run A.

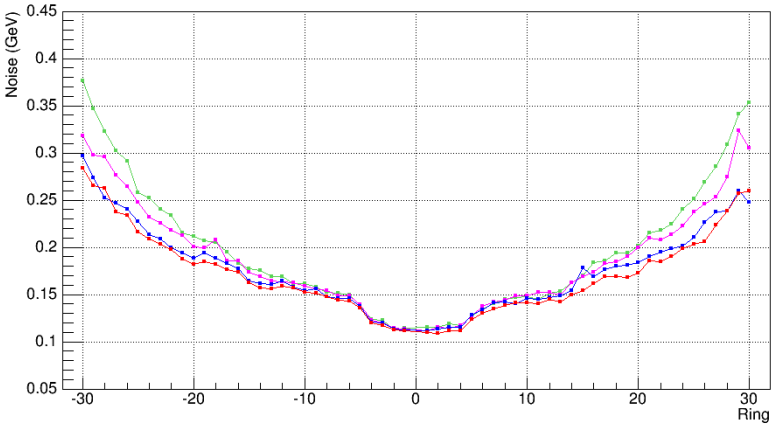

Figure 50: EE Noise in GeV. *Colors Legend:* red for Run A, blue for Run B, magenta for Run C, green for Run D.

In Ecal Endcap the loss in transparency of the crystals is bigger than in Ecal Barrel, as observed in Figure 37.

5.3 FUTURE PURPOSES

Future implications of the analysis for the estimation of the noise in ECAL: determination of the thresholds for the $\phi-$symmetry calibration method.

Considering the relationship between the noise and the ECAL energy thresholds (see Section 4.3.0.1), the study of the noise will be followed by the determination of the thresholds for the ϕ *symmetry* calibration method. In fact the latter one is conceived for a data analysis which is restricted to deposits with transverse energies between a lower and an upper threshold and the lower threshold is applied to remove the noise contributions.
The procedure which will be used for the determination of the thresh-

olds is similar to the method adopted for the estimation of the noise; in fact it starts considering the distributions of the first three samples of the pulse shape, from which pedestals are subtracted: these distributions are one for each channel. Then they are fitted with a Gaussian PDF and the moments of the distributions (μ and σ) are extracted: so the observable $t = \mu + 4\sigma$ can be created. After this procedure the distributions of a new variable called t (one for each ring) are created and then another Gaussian Fit is performed; the resulting μ and σ, called for clarity μ_t and σ_t are combined just like follows:

$$th = \mu_t + 3\sigma_t, \tag{10}$$

where th is the value of the thesholds for a given ring.

5.4 FIRST RESULTS FOR THE DETERMINATION OF THE THRESHOLDS

Following the strategy described above the first results for the determination of the thresholds are reported in Figure 51 for EB and in Figure 52 for EE; they can be compared with the values found in 2010 (see Figure 53).

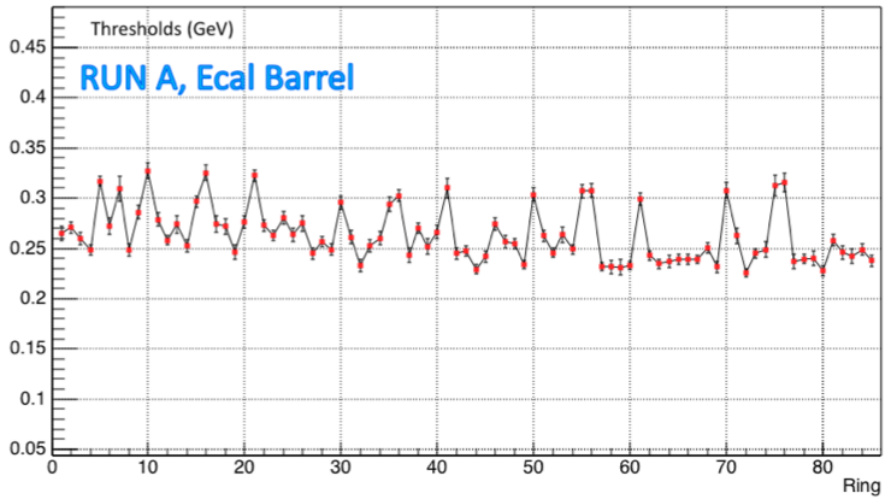

Figure 51: First results for the determination of the thresholds, EB, Run A.

Starting from 2015 the thresholds valid for Run D in 2012 will be used to take the first data; then using these data the thresholds will be redetermined.

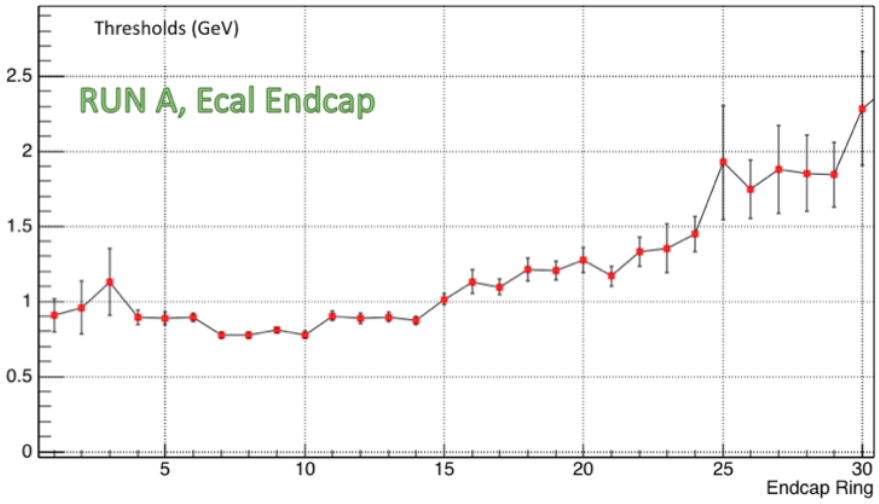

Figure 52: First results for the determination of the thresholds, EE, Run A.

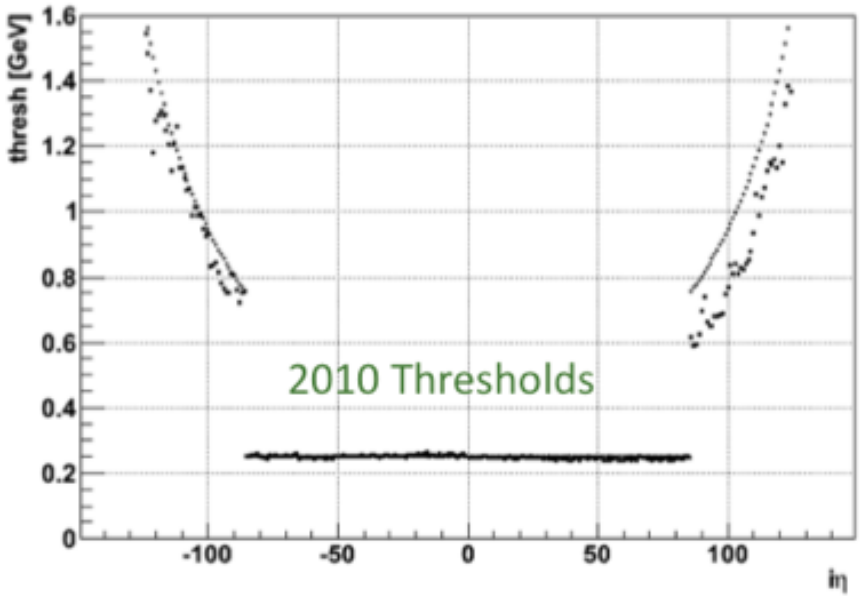

Figure 53: Thresholds in 2010 in EB.

Part IV

ANALYSIS OF THE $\Upsilon(nS)\gamma$ INVARIANT MASS SPECTRUM

The analysis of the invariant mass of the $\Upsilon(1S)\gamma$ and $\Upsilon(2S)\gamma$ spectra was conducted focusing the attenction to the $\chi_b(3P)$ state, discovered by the ATLAS experiment in 2011. The main purpose was the measurement of the mass of the $\chi_b(3P)$ using a simultaneous fit to the $\Upsilon(1S)\gamma$ and $\Upsilon(2S)\gamma$ channels: from this procedure rises that the measure can be done with a resolution which is better than the one obtained by the ATLAS and the LHCb experiments, which measured it first. To obtain the best S/B ratio the simultaneous fit is realized after the optimization of the single fits to the $\Upsilon(1S)$ and $\Upsilon(2S)$: this strategy allows the observation of an excess of invariant mass around 10.08 GeV, whose nature is still object of investigation.

6

QUARKONIUM THEORETICAL BACKGROUND

This part of the analysis is focused on the study of the invariant mass spectrum of the Y(kS) states, where k=1,2. These states are bottomonium states, that are bound states of $b\bar{b}$ quarks. Bottomonium states are included in the more general group of *quarkonium* states.
Quarkonium states are bound states ($q\bar{q}$) of heavy quarks; to be more precise, they are $c\bar{c}, b\bar{b}$ and $t\bar{t}$, where c refers to the charm flavour, b for bottom or beauty and t for top. These quarks are called *heavy* because their masses are much larger than $\Lambda_{QCD} \sim 200MeV$; under this value the predictions from perturbative QCD (pQCD) are not valid. Only $c\bar{c}$ (charmonium) and $b\bar{b}$ (bottomonium) states have been observed; in fact the top quark has a very short lifetime and decays before bound states are formed.

6.1 QUARKONIUM PRODUCTION

The inclusive production of a pair of charm or bottom quarks is an essentially perturbative process because the heavy quark mass m_Q is much larger than Λ_{QCD}, while the subsequent evolution of the pair into a quarkonium is nonperturbative. Different treatments of the nonperturbative transformation from a heavy quark pair to a bound quarkonium have led to various theoretical models for quarkonium production, most notably, the color singlet model (CSM), the color evaporation model (CEM) and the non-relativistic QCD (NRQCD) model. Among these models, the NRQCD treatment of heavy quarkonium production is both the most theoretically sound and phenomenologically successful.

6.1.1 *Electromagnetic production*

The electromagnetic production, in similarity with the Drell-Yan process, predicts that the production cross section of two annihilating quarks would be proportional to the square of the charge of the quarks. However the predictions of this theory are not compatible with the experimental results. As an example the following ratio between production cross sections

$$\frac{\sigma(\pi^- N \to q\bar{q}X)}{\sigma(\pi^+ N \to q\bar{q}X)} = \frac{Q(\bar{u})^2}{Q(\bar{d})^2} = \frac{(2/3)^2}{(1/3)^2} = 4 \tag{11}$$

is not observed.

Another aspect is important in understanding quarkonium production considering the $q\bar{q}$ annihilation (see Figure 54) into a gluon as the main production process: the consequent suppression factor would be about 5-10 in pp collisions with respect to the $p\bar{p}$ ones, but also in this case the theoretical predictions are not confirmed by the experiments, where a suppression is observed, but it is much smaller than the expected value (see Figure 55).
So the quarkonia production mechanism must involve processes with gluons in the initial state, such as the gluon fusion and the gluon fragmentation, whose Feynman diagrams are shown in Figure 56 and Figure 57.

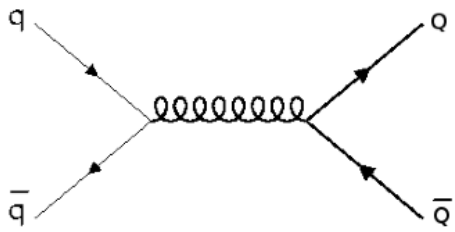

Figure 54: Feynman diagram showing the $q\bar{q}$ annihilation.

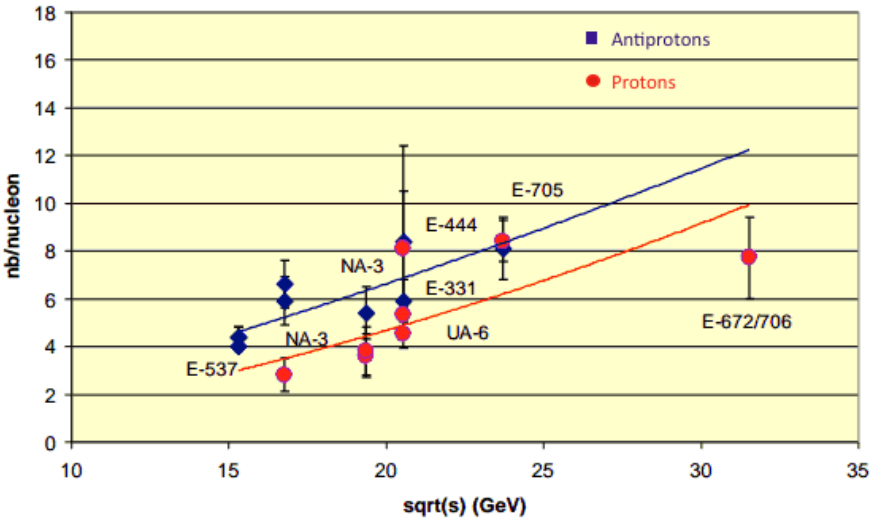

Figure 55: Suppression factor in $q\bar{q}$ annihilation.

6.1.2 *CEM, CMS, NRQCD*

As said above, the quarkonium production has a double nature: it involves both hard processes, which are characterized by high enegies and small values of α_s during the annihilation phase, and non per-

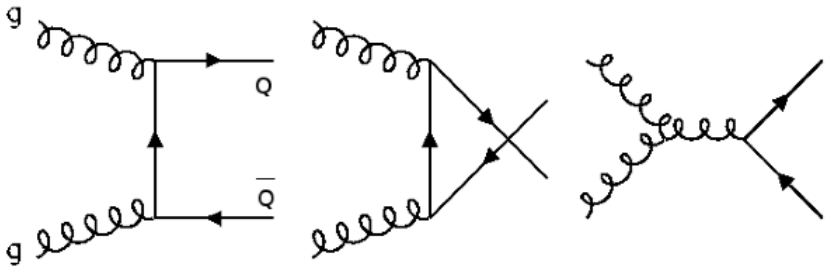

Figure 56: Feynman diagrams showing the gluon fusion.

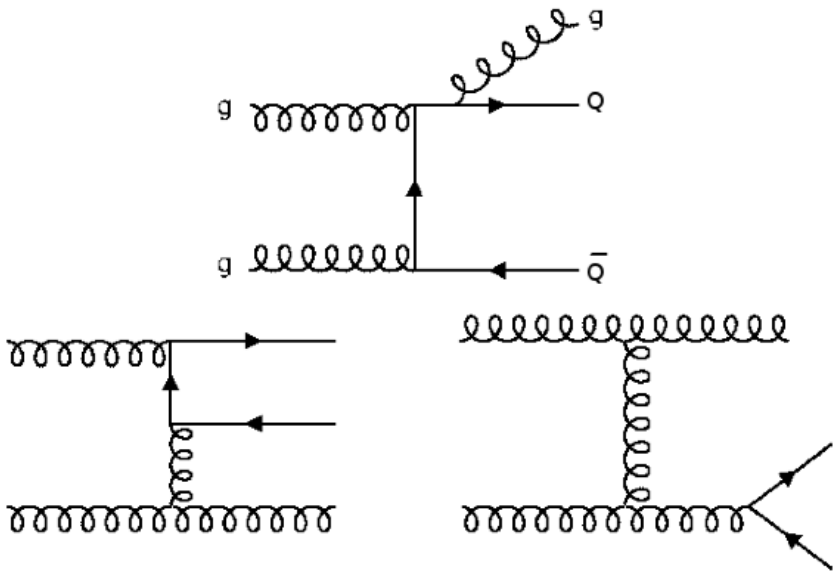

Figure 57: Feynman diagrams showing the gluon fragmentation.

turbative dynamics (v_Q/C small) during the hadronization phase. A $Q\bar{Q}$ state can be a color singlet or a color octet, and corresponds to the different possible combinations of angular momentum of the pair $Q\bar{Q}$. The quarkonium states measured in experiments are color singlets, so if the $Q\bar{Q}$ couple is produced in a color octet state, it must neutralize its color. There are different models which offer a description of these processes, grounding on the factorization method; they are the Color Evaporation Model (CEM), the Color Singlet Model (CSM) and the Non-relativistic QCD (NQCD)[8].

CEM In the Color Evaporation Model the cross section for the production of a quarkonium state H is some fraction F_H of the cross section for producing $Q\bar{Q}$ pairs with invariant mass below the $M\bar{M}$ threshold, where M is the lowest-mass meson containing the heavy quark Q. The cross section for producing $Q\bar{Q}$ pairs has an upper limit on the pair mass, but no constraints on the color or spin of the

final state. The $Q\bar{Q}$ pair is assumed to neutralize its color by interaction with the collision-induced color field, that is, by *color evaporation*. In some versions of the CEM the color-neutralization process is also assumed to randomize the spins of the Q and the $\bar{Q}$. The CEM parameter F_H is the probability that a $Q\bar{Q}$ pair with invariant mass less than $2\,m_M$, where m_M is the mass of the meson M, will bind to form the quarkonium state H. That probability is assumed to be 0 if the $Q\bar{Q}$ pair has invariant mass greater than $2\,m_M$. In the CEM, the production cross section for the quarkonium state H in the collisions of light hadrons, photons or leptons A and B is:

$$\sigma_{CEM}[AB \to H + X] = F_H \int_{4m^2}^{4m_M^2} dm^2_{Q\bar{Q}} \frac{d\sigma[AB \to H + X]}{dm^2_{Q\bar{Q}}}, \quad (12)$$

where $m_{Q\bar{Q}}$ is the invariant mass of the $Q\bar{Q}$ pair, m is the heavy-quark mass, and $\frac{d\sigma[AB\to H+X]}{dm^2_{Q\bar{Q}}}$ on the right side is the inclusive differential cross section for a $Q\bar{Q}$ pair to be produced in a collision of A and B. There is an implied sum over the colors and spins of the final-state $Q\bar{Q}$ pair. This is where the central model assumptions of color evaporation and spin randomization manifest themselves. If A and/or B are hadrons or photons, the cross section for $AB \to Q\bar{Q} + X$ can be expressed as a convolution of parton distributions for A and/or B and a parton cross section. At leading order in α_s, the parton process $ij \to Q\bar{Q}$ creates a $Q\bar{Q}$ pair with zero transverse momentum p_T, and the differential cross section d/dp_T^2 is proportional to $\delta(p_T^2)$. At next-to-leading order in α_s (NLO), there are parton processes $ij \to Q\bar{Q} + k$ that create a $Q\bar{Q}$ pair with nonzero p_T . The complete NLO differential cross section is a distribution that includes singular terms proportional to $\delta(p_T^2)$ and $1/(p_T^2)$, but whose integral over p_T is well behaved. Some kind of smearing over p_T is necessary to obtain a smooth p_T distribution that can be compared with experiment. The physical origin of the smearing is multiple gluon emission from the initial and final state partons.

CSM The Colour Singlet Model (CSM) was firstly proposed shortly after the discovery of the J/ψ. The main concept of the CSM is that, in order to produce a quarkonium, the $Q\bar{Q}$ pair must be generated with the quarkonium quantum numbers; in particular the pair has to be produced in a colour-singlet state. The CSM was succesfull in predicting quarkonium production rates at relatively low energy. At leading order (LO) it underestimates the J/ψ and the $\psi(2S)$ production cross section, as was seen at Tevatron (see Figure 58), by a factor 50.

However, recently, it has been found that at higher energies next-to-leading-order (NLO) and next-to-next-leading-order (NNLO) calculations in α_s rise very large corrections to CSM. It is therefore unclear if the perturbation expansions in α_s converges.

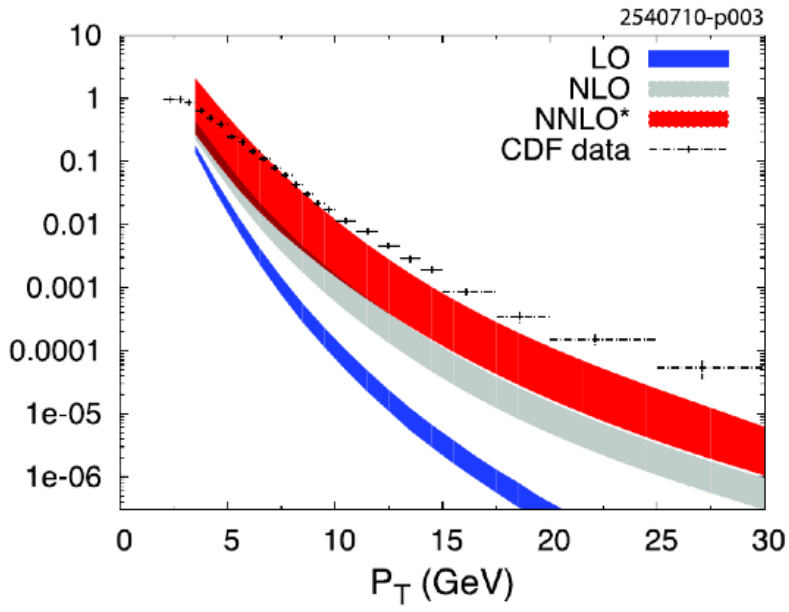

Figure 58: Comparison between CSM prediction for the $\psi(2S)$ cross section at LO, NLO and NNLO accuracy as a function of $p_T(\psi(2S))$ at Tevatron at $\sqrt{s} = 1.96 TeV$.

NRQCD The NRQCD factorization approach incorporates aspects of both the CSM and CEM and can be regarded as a unification of these two models within a consistent theoretical framework. It can be summarized by the NRQCD factorization formula, which separates short-distance, perturbative effects involving momenta of order m_Q from long-distance, nonperturbative effects.
The NRQCD factorization formula for the inclusive cross section for production of a specific heavy-quarkonium state H is

$$\sigma[AB \to H + X] = \sum_n c_n^{AB}(\Lambda) < O_n^H(\Lambda) > . \tag{13}$$

Here, A and B are light hadrons, photons or leptons and Λ is the ultraviolet cutoff of the effective theory. The c_n^{AB} are short-distance coefficients that can be calculated in perturbation theory by matching amplitudes in NRQCD with those in full QCD. The matrix elements $< O_n^H >$ are vacuum-expectation values of four-fermion operators in NRQCD, evaluated in the rest frame of the quarkonium. These matrix elements contain all of the nonperturbative physics of the evolution of a $Q\bar{Q}$ pair into a quarkonium state. The operators have the form

$$O_n^H = \chi^\dagger \kappa_n^H(\Lambda) \psi^\dagger \kappa_n' \chi, \tag{14}$$

where ψ is the two-component (Pauli) spinor that annihilates a heavy quark, χ is the two-component spinor that creates a heavy antiquark, and P^H is a projector onto states that in the asymptotic future contain

the quarkonium H plus light partons X whose energies and momenta lie below the cutoff Λ of the effective field theory:

$$P^H(\Lambda) = \sum_X |H + X, t \to \infty >< H + X, , t \to \infty|. \tag{15}$$

The factors κ_n and κ'_n are direct products of a color matrix and a spin matrix. The matrix elements fall into a hierarchy according to their scaling with the velocity v of the heavy quark (or antiquark) in the quarkonium rest frame. $v^2 \approx 0.3$ for charmonium, and $v^2 \approx 0.1$ for bottomonium. In practice, the summation over these matrix elements is usually truncated at a low order in v. The NRQCD factorization formalism has enjoyed a good deal of phenomenological success in describing inclusive quarkonium production at hadron, $e-p$, and e^+e^- colliders and in fixed-target experiments.

6.2 QUARKONIUM SPECTROSCOPY

According to some important aspects of the NRQCD, the quarkonium states can be considered as non relativistic state; in fact while the light quarks in a meson move at relativistic speeds, since the mass of the bound state is much larger than the mass of the quark, the charm and the beauty quarks in charmonium and bottomonium have a velocity sufficiently small to consider with good approximation that the relativistic effects don't affect their bound states. As mentioned above, the velocity is estimated to be 0.3 and 0.1 times the speed of light for charmonium and bottomonium, respectively.
The fact that charm and beauty quarks move in quarkonium with non relativistic speed allows to assume that they move into a static potential, much like the non relativistic-model for the hydrogen atom. The potential, called Cornell Potential, can be describe as

$$V(r) = -\frac{4}{3}\frac{\alpha_s}{r} + kr, \tag{16}$$

where r is the distance between the two quarks, $4/3$ is the color factor, k is a parameter related to the confinement; α_s is the strong running coupling constant, defined as following:

$$\alpha_s(\vec{p}^2) = \frac{48\pi^2}{33 - N_f}\frac{1}{\ln(\vec{p}^2/\Lambda^2)},\ \vec{p}^2 >> \Lambda^2, \tag{17}$$

where N_f is the number of the fermions and Λ is the QCD scale parameter. The latter represents the energy scale at which a certain physics phenomenon is studied and the value of α_s varies with this scale, as shown in Figure 59.

The first term in the Cornell Potential is Coulomb-like, accounting for the gluon-exchange between the two quarks; the second is a confining term parameterizing the non-perturbative effects.

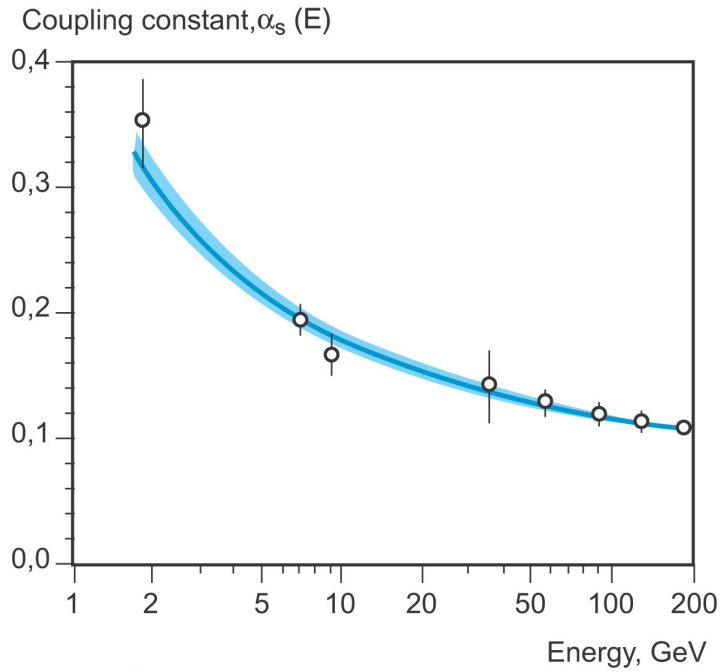

Figure 59: The running coupling constant, α_s, as a function of the energy scale E.

The hamiltonian for a non relativistic quarkonium state can be written in analogy with the hydrogen atom. For the latter, assuming V(x,y,z) the potential between the electron and the nucleus, the hamiltoniam can be written as

$$H = \frac{p^2}{2\mu} + V(x,y,z), \tag{18}$$

where the kinetic term contains the reduced mass, $\mu = \frac{m_e M}{m_e + M}$, with M the mass of the nucleus. Solving the Schrodinger equation with his Hamiltonian the energy spectrum of the hydrogen atom can be calculated.
For a $Q\bar{Q}$ bound state the potential can be written in this way, using the Cornell Potential as the potential term:

$$H = \frac{p^2}{2\mu} - \frac{4}{3}\frac{\alpha_s}{r} + kr, \tag{19}$$

where $\mu = m_Q/2$ is the reduced mass of the two quarks.

Quarkonium states can be classified, as the energy levels in spectrum of the hydrogen atom, using the following quantum numbers:

- n, the radial quantum number;
- L, the eigenvalue of the radial angular momentum;
- S, the eigenvalue of the spin;
- J, the eigenvalue of the total angular momentum.

6.3 BOTTOMONIUM: Υ(KS) AND $\chi_{bj}(nP)$ STATES

The spectrum of the Bottomonium ($b\bar{b}$ bound states), shown in Figure 60, classifies in a schematic way the $b\bar{b}$ states on the basis of their spectroscopical properties.

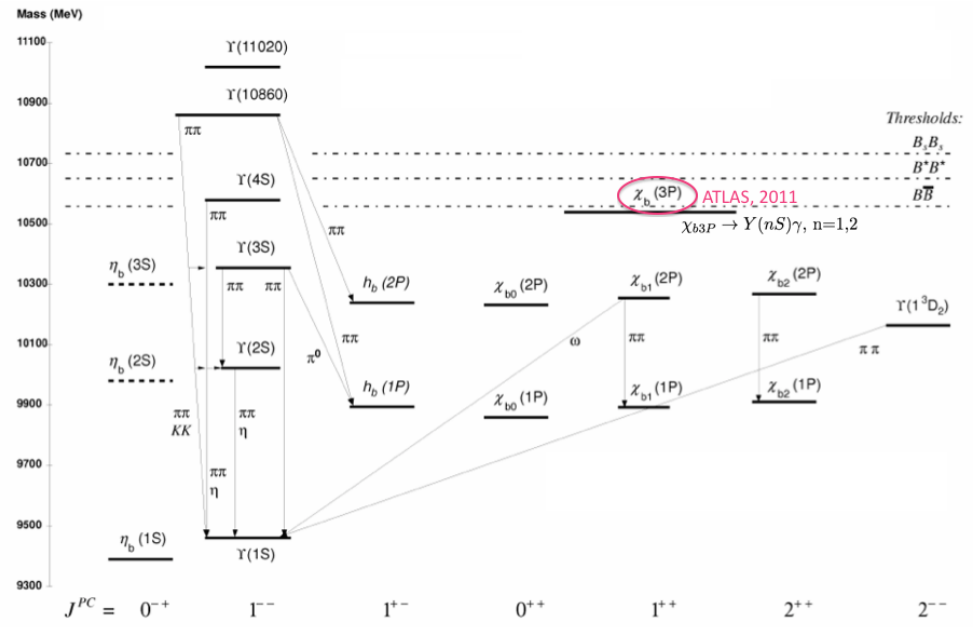

Figure 60: The Bottomonium Spectrum.

Υ(1S), Υ(2S) states and the $\chi_b(3P)$ in the bottomonium spectrum: quantum numbers and properties.

Particular attenction goes to the Υ(1S) and Υ(2S) states and to the $\chi_b(3P)$: in fact the analysis described hereafter studies the spectrum of the invariant mass of the Υ(1S) and Υ(2S) in order to measure the mass of the $\chi_b(3P)$ with precision. The Υ(1S) and Υ(2S) are the first and second radial excitation after the ground state, respectively; the $\chi_b(nP)$ states are the n-radial excitations in P-wave, where n = 1,2,3; each $\chi_b(nP)$ is a triplet of states, as the composition of their angular momentum demonstrates:

$$(S = 1) \otimes (L = 1) = (J = 0) \oplus (J = 1) \oplus (J = 2). \tag{20}$$

Low Branching Ratios of the χ_{b0} states.

For the purposes of this analysis the χ_{b0} states are not considered beacause of their low branching ratios to Υ(1S)γ (and also to Υ(2S)γ for the second radial excitations) with respect to the other spin states, so that their contribution is negligible. The quantum numbers of these χ_b states are reported in Figure 61, while the Figure 62 shows masses, branching ratios and Q-values for the χ_b states from the DPG.

6.4 THE $\chi_b(3P)$ RECONSTRUCTION AND DISCOVERY

For the reconstruction of the $\chi_b(nP)$ states their radiative decays into Υ(1S) and Υ(2S) are used; in particular for the $\chi_b(3P)$ are consid-

Resonance	I^G	J^{PC}
$\Upsilon(1S)$	0^-	1^{--}
$\chi_{b0}(nP)$	0^+	0^{++}
$\chi_{b1}(nP)$	0^+	1^{++}
$\chi_{b2}(nP)$	0^+	2^{++}

Figure 61: χ_b states quantum numbers.

Particle	Mass [MeV]	$BR(\chi_b \to \Upsilon(1S)+\gamma)$	$\Delta m(\chi_b, \Upsilon)$ [MeV]
$\chi_{b0}(1P)$	$9859.44 \pm 0.42 \pm 0.31$	$(1.76 \pm 0.35)\%$	399.1
$\chi_{b1}(1P)$	$9892.78 \pm 0.26 \pm 0.31$	$(33.9 \pm 2.2)\%$	432.5
$\chi_{b2}(1P)$	$9912.21 \pm 0.26 \pm 0.31$	$(19.1 \pm 1.2)\%$	451.9
$\chi_{b0}(2P)$	$10232.5 \pm 0.4 \pm 0.5$	$(9 \pm 6) \cdot 10^{-3}\%$	772.5
$\chi_{b1}(2P)$	$10255.46 \pm 0.22 \pm 0.5$	$(9.2 \pm 0.8)\%$	795.2
$\chi_{b2}(2P)$	$10268.65 \pm 0.22 \pm 0.5$	$(7.0 \pm 0.7)\%$	808.4
$\chi_b(3P)$	$10539 \pm 4 \pm 8$	Unknown	899

Figure 62: Masses, branching ratios and Q-values for the χ_b states (DPG).

ered the decays $\chi_b(3P) \to \Upsilon(1S)\gamma$ and $\chi_b(3P) \to \Upsilon(2S)\gamma$, where $\Upsilon(1S), \Upsilon(2S) \to \mu^+\mu^-$; the photon is reconstructed through conversions into e^+e^- pairs or by calorimetric measurements.
With these techniques the ATLAS experiment observed a new structure centered at a mass of:

$$10.530 \pm 0.005(stat.) \pm 0.009(syst.)\ GeV; \tag{21}$$

so it announced the discovery of a new particle, the $\chi_b(3P)$, at LHC in 21^{st} December 2011 [3].
The mass distributions of the χ_b candidates from unconverted and converted photons by the ATLAS experiment are shown in Figure 63 and Figure 64, respectively.

The most recent contribution to the determination of the mass of the $\chi_b(3P)$ belongs to the LHCb experiment, which presented the following value the 4^{th} September 2014 [7]:

$$m_{\chi_{b1}(3P)} = 10512.1 \pm 2.1(exp) \pm 0.9(syst)\ MeV/c^2. \tag{22}$$

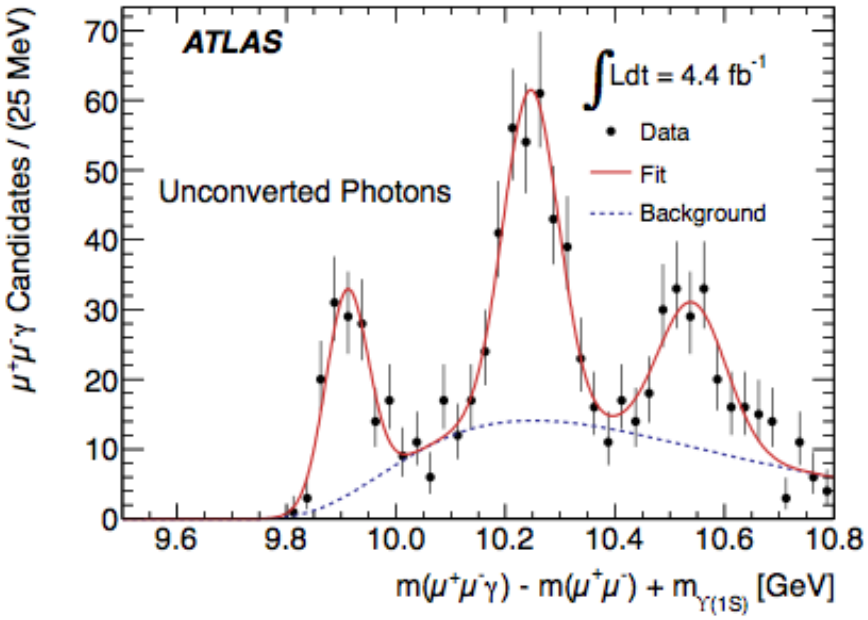

Figure 63: The mass distribution of $\chi_b \rightarrow \Upsilon(1S)\gamma$ candidates for unconverted photons reconstructed from energy deposits in the ATLAS electromagnetic calorimeter.

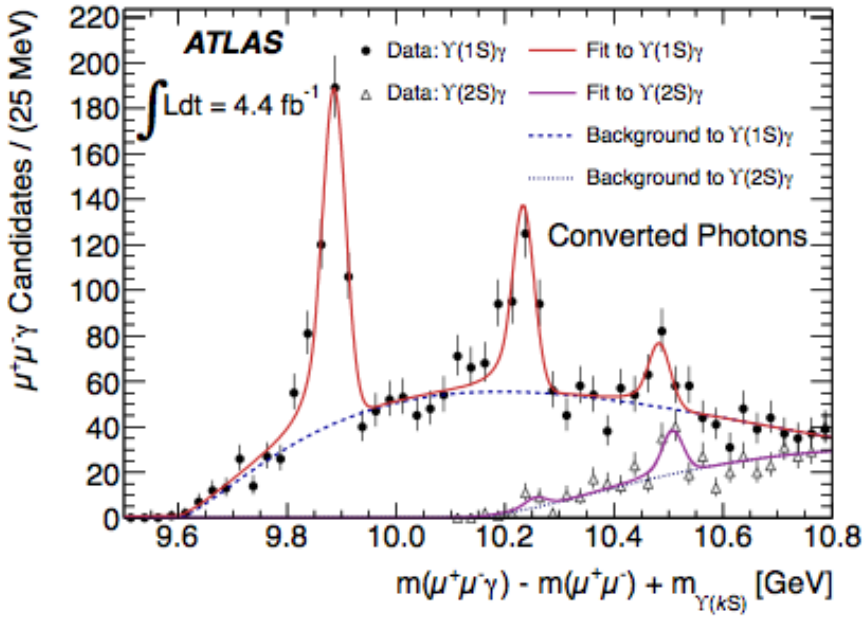

Figure 64: The mass distribution of $\chi_b \rightarrow \Upsilon(nS)\gamma$ (n=1,2) candidates for formed using photons which have converted and been reconstructed in the ATLAS Inner Detector. Data are shown before the correction for the energy loss from the photon conversion electrons due to bremsstrahlung and other processes.

7

THE EXPERIMENTAL METHOD

The $\chi_b(nP)$ states (n=1,2,3) are reconstructed through the decay chain $\chi_b(nP) \to \Upsilon(kS)\gamma$ (n=1,2,3 and k=1,2), where $\Upsilon(kS) \to \mu^+\mu^-$. In the matter of such a decay two things are mainly needed: the detection of the photon in the radiative decays $\chi_b(nP) \to \Upsilon(kS)\gamma$ and the reconstruction of the $\Upsilon(kS)$ states.

7.1 EVENT RECONSTRUCTION AND SELECTION

The data taken into account for this analysis are from the 2012 data; they were collected using a High Level Trigger (HLT) path specifically designed for the Y selection. This trigger asks for the following requirements:

- p_T of the Y candidate has a minimum value of 7 GeV;
- the two muons (dimuon) produced from the decay of the Y candidate must have opposite charge;
- the trajectories of the two muons are fitted with a common vertex constraint and the events are considered for the selection if the χ^2 probability of the fit is larger than 0.5 %;
- if the dimuon mass belongs to the window [8.5-11.5] GeV the relative events are stored.

7.1.1 *Y(kS) selection and muon reconstruction*

The selection Y(kS), with k=1,2, stars from the muon reconstruction; this is developed by the CMS Muon Physics Object Group (POG) which has the charge to develop, validate, maintain and study the performance and the tools to identify and reconstruct muons using all relevant informations from the CMS detector, both for the offline analysis and for the online HLT event selection.

7.1.1.1 *Muon Reconstruction*

The reconstructed muons are classified into three different types or objects.

In the CMS muon reconstruction process, muons can be defined as three different objects: *standalone muons*, *tracker muons* and *global muons*. Standalone muons are reconstructed only from the

signal of the muon system, that is the Drift Tubes (DT), the Cathode Strip Chambers (CSC) and the Resistive Plate Chambers (RPC); tracker muons are reconstructed only from the tracker signal and Global Muons are built as a combined fit of *silicon and muon chamber hits*, coming from different track segments found in the tracker and muon systems.

The muon reconstruction procedure starts with the identification of the standalone muons; then, for each of them, an algorithm created by the CMS POG group searches for the global muon object.

The muon reconstruction chain starts with the *local reconstruction*. First, hits in Drift Tubes (DT), Cathode Strips Chamber (CSC) and Resistive Plate Chambers (RPC) are reconstructed from digitized electronics signals. Hits within each DT and CSC chamber are then matched to form *segments*. In the offline reconstruction, the segments reconstructed in the muon chambers are used to generate *seeds* consisting of position and direction vectors and an estimate of the muon transverse momentum. These initial estimates are used as seeds for the track fits in the muon system, which are performed using segments and hits from DTs, CSCs and RPCs and are based on the Kalman Filter technique. The result of this fit is known as *standalone muons* as no information as been used from the inner tracking system.
For each standalone muon track, a search for tracks matching it among those reconstructed in the inner tracking system (called *tracker tracks* or *inner tracks* or *silicon tracks*) is performed, and the best matching tracker track is selected. For each *tracker track - standalone muon* pair, the track fit using all hits in both tracks is performed, again based on the Kalman Filter technique. The result is known as *global muon*.
An overview on the muon reconstruction process is shown in Figure 65, where the paths for the muon local reconstruction, the standalone muons and the global muons can be observed. The *tracker muons* and the *calo muons* are specified there, too.

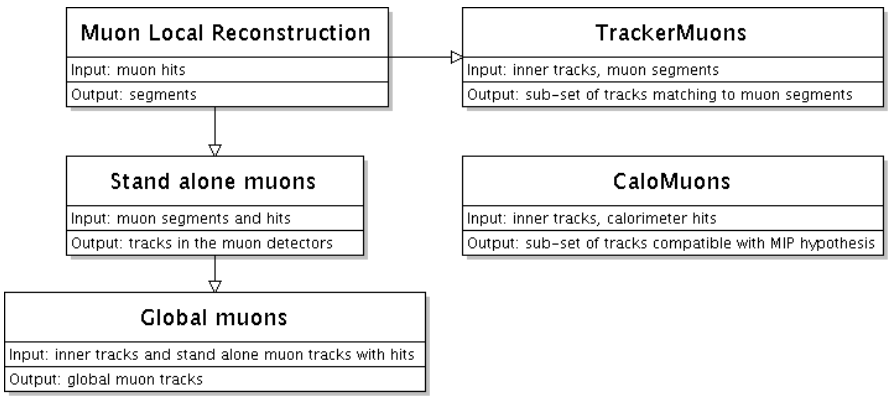

Figure 65: Overview on the muon reconstruction.

The algorithm for the tracker muons represents an approach complementary to the global-muon reconstruction and consists in considering all tracker tracks to be potential muon candidates and in checking this hypothesis by looking for compatible signatures in the calorimeters and in the muon system. Tracker tracks identified as muons by this method are referred to as *Tracker Muons*. This algorithm is particularly useful for the identification of low-p_T muons (with p_T of the order of several GeV), which may not leave enough hits in the muon stations for a standalone muon to be reconstructed.
An approach similar to Tracker Muons is followed to define the *RPC Muons*: in this case a match is sought between the extrapolated inner track and hits on the RPC muon detectors.
Calorimeter-based muons, called *Calo Muons*, represent a subset of all tracker tracks reconstructed in the event, which includes tracks with energy depositions in the calorimeters compatible with those of a minimum-ionizing particle. The fake rate of these muon candidates is high and they should not be used when muon purity is essential. A typical used case for Calo Muons is the reconstruction of the J/ψ decaying to low-momentum muons that have little or no information in the muon system, thus improving signal to background ratio compared with the inner tracks.
The momentum measurement of muons and, more generally, of all charged tracks in the CMS detector is affected by systematic uncertainties due to incomplete knowledge of the magnetic field and of the material budget, to subdetectors misalignment and to biases in the algorithms which fit the track trajectory. Studies performed with Cosmic Ray muons and collision data show a very precise control of all these possible biases.

7.1.1.2 *Muon Selection*

For the analysis either the Global or Tracker muons are used, with some constraints: muon identification is achieved requiring the tracker track to be matched with at least one muon segment, in any station, both in x and y coordinates. To ensure an accurate p_T measurement and suppress as possible decays in flight the number of tracker layers with at least one hit must be grater than five, at least one being in the pixel detector. The single muon tracks are required to have $p_T > 3.3$ GeV for $|\eta| < 1.3$ and $p < 2.9$ GeV for $1.3 < |\eta| < 2.2$; the χ^2 probability of a fit where the two muon tracks are constrained to a common vertex is more than 1%. Events are rejected if the distance in the plane transverse to the beam line between the dimuon vertex and the interaction point is larger than 100 μm, to reject muon pairs

which have an invariant mass in the mass region but which are not dimuons from Υ decays.

7.1.2 *Photon Reconstruction*

The main difficulty reconstructing the radiative decays $\chi_b(nP) \rightarrow \Upsilon(kS)\gamma$, where n=1,2,3 and k=1,2), is the detection of the photon. The difference between the masses of the χ_{b1} and χ_{b2} is small, 19.4 MeV. In the center of mass of the χ_b states the photon decaying from the $\chi_{b1}(1P)$ has 432 MeV and the photon decaying from $\chi_{b1}(2P)$ has 795 MeV; indeed the E_T of the detected photon in the laboratory mostly lies between 500 MeV and 2 GeV.
The CMS subdetector designed to detect photons is the Electromagnetic Calorimeter (ECAL), but it has a poor resolution for low energy photons ($\simeq$ 50 MeV)) for the requirements of the analysis.
A valid alternative to ECAL is a new strategy for the photon detection which uses the CMS silicon tracker: it consists in searching for photons which, through pair-production, converted in the beam-pipe or the inner layers of CMS silicon tracker and reconstruct the tracks left by the electron-positron pair inside the tracker. With this procedure a very accurate resolution of the photon is obtained: it allows to distinguish the primary vertex the photon comes from: this is an important feature in the cases with multiple p-p collisions (pileup events); indeed allows the two states χ_{b1} and χ_{b2} to be resolved with good separation.

7.1.2.1 *Photons conversions*

Photon conversions are characterized by an electron-positron pair originating from the conversion vertex. The invariant mass must be compatible with zero and the two tracks are therefore parallel at production vertex and open only in the transverse plane because of the magnetic field generated by the solenoidal superconducting magnet. Since the photons have low energies, the electron-positron pair originating from the conversionn vertex is soft and most of them are either fully stopped before they reach the electromagnetic calorimeter or they are bent in a spiral (helix in 3D) within the tracker, thus such conversions can be only reconstructed within the tracker detector.

7.1.3 χ_b *reconstruction*

For each selected event the Y candidates and the converted photons are paired to reconstruct the χ_b candidates; the mass of the χ_b candidate is obtained from the Q-value, $Q = m_{\mu\mu\gamma} - m_{\mu\mu}$, in addition to the mass of the Y candidated; for the latter one the PDG value is used. The use of the Q-value, which must be less than 2 GeV, has the advantage that the event by event uncertainty on the dimuon invariant mass due to the finite momentum resolution cancels out. The Q-value of the χ_b, indeed, doesn't depend on the estimation of the di-muon invariant mass: its accuracy depends on the resolution of the gamma momentum measurement.

7.1.3.1 *Kinematical Fit and Signal Model*

The fit to Y(1S) and Y(2S) is performed modeling the χ_b shapes with a Crystal Ball function; it is a probability density function frequently used to empirically modeled processes where radiative losses are involved; it is composed of a gaussian core, described by two parameters, μ and σ, and an exponential tail. The Double Sided Crystal Ball has an exponential tail on both sides; its formal description is the following one:

$$f(x) = \begin{cases} (n_1/|\alpha_1|)^{n_1} e^{-\alpha_1^2/2} \left(\frac{n_1}{\alpha_1} - \alpha_1 - \frac{m-m_0}{\sigma} \right)^{-n_1}, & \frac{m-m_0}{\sigma} \leqslant -\alpha_1 \\ e^{-\frac{(m-m_0)^2}{2\sigma}}, & -\alpha_1 < \frac{m-m_0}{\sigma} < \alpha_2 \\ (n_2/|\alpha_2|)^{n_2} e^{-\alpha_2^2/2} \left(\frac{n_2}{\alpha_2} - \alpha_2 - \frac{m-m_0}{\sigma} \right)^{-n_2}, & \frac{m-m_0}{\sigma} \geqslant -\alpha_2 \end{cases} \tag{23}$$

It has six parameters, $\alpha_1, n_1, \alpha_2, n_2, \sigma$ and m_0, where α_1 and α_2 are the transition points of respectively the first and the second exponential functions, n_1 and n_2 are the exponential bases of the two functions, σ and m_0 are respectively the variance and the mean of the gaussian core.
The probability density function used for the combinatorial background is defined as:

$$F_{bkg} = (m - m_0)^{\lambda} \times e^{(m-m_0)\nu}, \tag{24}$$

where m is the $\mu\mu\gamma$ invariant mass obtained after the kinematical fit and m_0, λ and ν are free parameters. The final likelihood function is:

$$P(m) = N_{sig}[f_1 \times F_1(m) + (1 - f_1) \times F_2(m)] + N_{bkg} \times F_{bkg}(m), \tag{25}$$

where N_{sig} is the total number of the χ_{b1} and χ_{b2} candidates, f_1 and f_2 are respectively the fraction of he χ_{b1} and the χ_{b2}, F_1 and F_2 are the Double Sided Crystal Ball Functions.

7.1.4 *Parameters for the $\chi_b(3P)$ shape*

The lineshape of the $\chi_b(3P)$, which is expected to be a narrow resonance, is dominated by the detector response. A parametrization of the latter is needed. The parameters for the Crystal Ball functions, in particular α and σ, used to fit the $\chi_b(3P)$ signal are obtained through Monte Carlo simulations, which are performed using a PYTHIA6 particle gun.
A particle gun simulator generates a single particle and its decays per event; the decay products are then processed into a full simulation of the CMS detector producing an output similar of that of real data. To simulate che radiative decays of the $\chi_b(3P)$ two Monte Carlo were used: one for the $\Upsilon(1S)\gamma$ channel and the other one for the $\Upsilon(2S)\gamma$ channel. For the decay in $\Upsilon(1S)\gamma$, as an example, PYTHIA's particle gun was configurated to use PDG's masses and to force the χ_b states to decay in $\Upsilon(1S)\gamma$, where $\Upsilon(1S)$ were forced to decay in $\mu^+\mu^-$; the relevant code used for the PYTHIA configuration is reported:

```
'MSEL=61                        ! Quarkonia',
'MDME(1035,1)=1                 ! Upsilon -> mumu turned ON',
'MDME(1034,1)=0                 ! Upsilon -> ALL THE REST',
'MDME(1036,1)=0                 ! Upsilon -> ALL THE REST',
'MDME(1037,1)=0                 ! Upsilon -> ALL THE REST',
'MDME(1038,1)=0                 ! Upsilon -> ALL THE REST',
'MDME(1039,1)=0                 ! Upsilon -> ALL THE REST',
'MDME(1040,1)=0                 ! Upsilon -> ALL THE REST',
'MDME(1041,1)=0                 ! Upsilon -> ALL THE REST',
'MDME(1042,1)=0                 ! Upsilon -> ALL THE REST',
'BRAT(1565)=1.0              ! chi_1b->Upsilon gamma',
'BRAT(1566)=0.0              ! chi_1b->g g',
'BRAT(1043)=1.0              ! chi_2b->Upsilon gamma',
'BRAT(1044)=0.0              ! chi_2b->g g',
'PMAS(294,1)=10.511             ! Mass of chi_b1(3P) ',
'PMAS(148,1)=10.523             ! Mass of chi_b2(3P) ',
```

where the two last lines concern the masses of the $\chi_b(3P)$ states with $J = 1$ and $J = 2$ respectively.

The simulation creates samples for the $\chi_{bj}(3P)$ states, where j=1,2. The fitting procedure of this sample is conducted fixing the parameters n_1 and n_2 to 2.5 GeV; the other parameters, α_1, α_2, σ and μ are left free. The results from these fits are shown in Figure 66, Figure 67, Figure 68 and Figure 69.

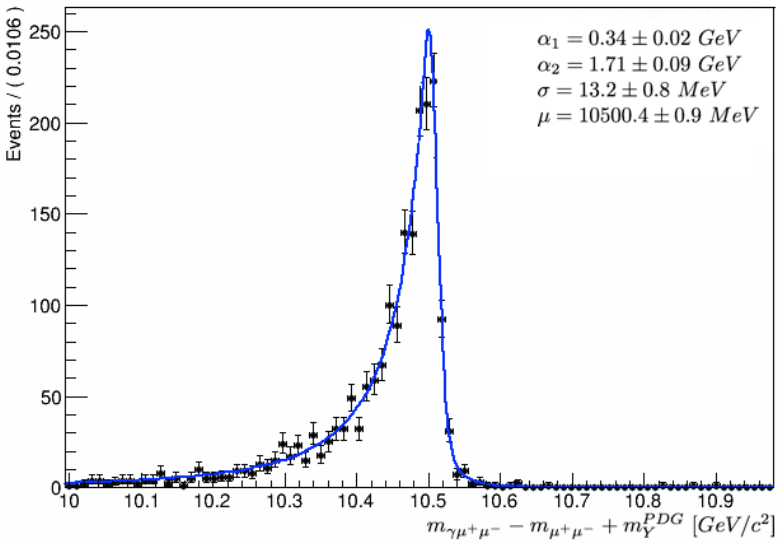

Figure 66: Fit of the MC samples of $\chi_{b1}(3P)$ in the Υ(1S) channel.

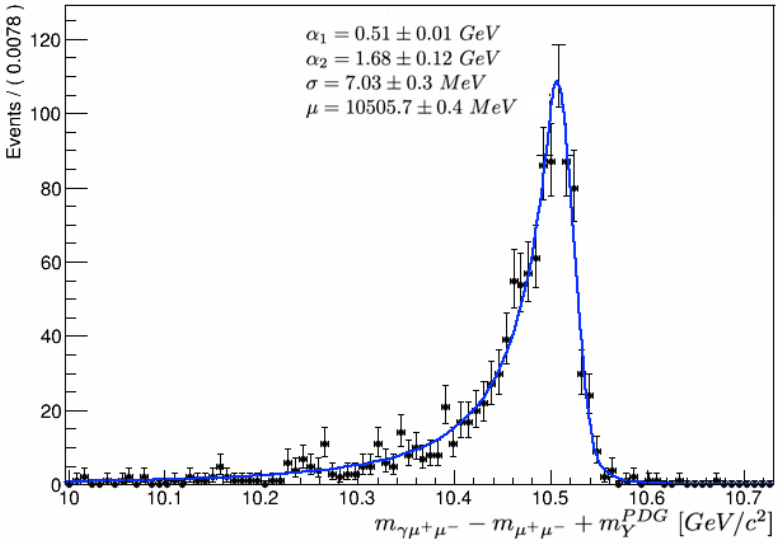

Figure 67: Fit of the MC samples of $\chi_{b2}(3P)$ in the Υ(1S) channel.

OBSERVATIONS The mass resolution improves for the $\Upsilon(2S)\gamma$ channel with respect to the $\Upsilon(1S)\gamma$ channel; in facts the photon from the first decay is softer and its energy can be measured with a better precision. For this reason the strategy for the measurement of the mass of the $\chi_b(3P)$, whose results are presented in Chapter 9, consists in a simultaneous fit to Υ(1S) and Υ(2S) states.

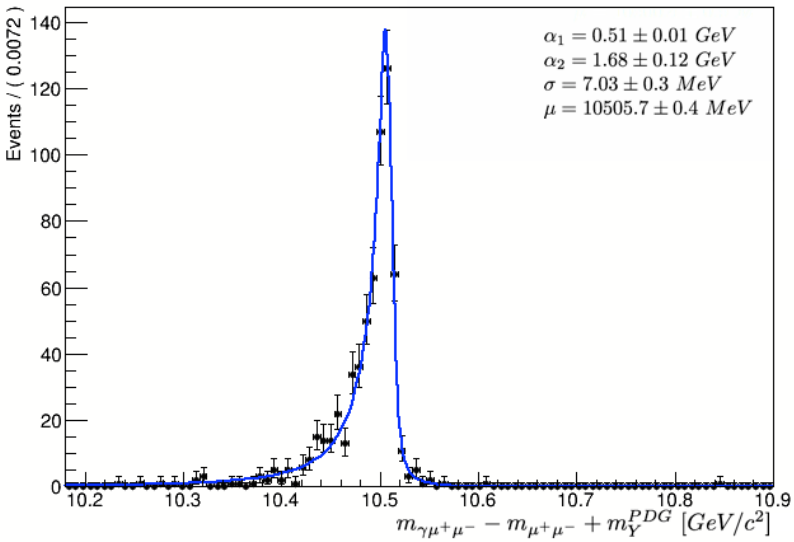

Figure 68: Fit of the MC samples of $\chi_{b1}(3P)$ in the Υ(2S) channel.

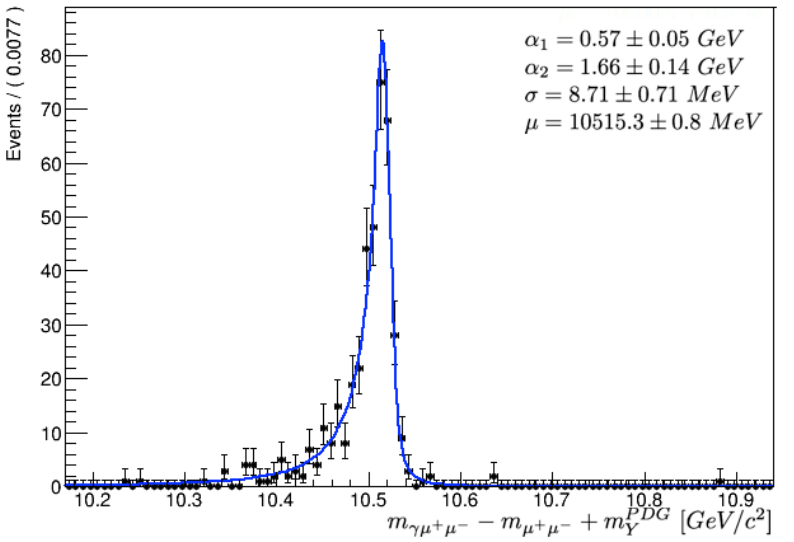

Figure 69: Fit of the MC samples of $\chi_{b2}(3P)$ in the Υ(2S) channel.

8

OBSERVATION OF AN EXCESS OF INVARIANT MASS AROUND 10.08 GEV

Since the goal of this analysis is the determination of the mass of the $\chi_b(3P)$ through the study of the $\Upsilon(1S)\gamma$ and $\Upsilon(2S)\gamma$ invariant mass spectra, the strategy of firstly optimize the fit to these spectra is adopted. In particular this procedure starts with searching for the cuts to the fit of the $\chi_b(2P)$ that maximize the ratio R, defined as:

$$R = \frac{S}{\sqrt{S+B}}, \tag{26}$$

where S and B represent the signals and the background events of the $\chi_b(2P)$, respectively. In this way the $\chi_b(3P)$ signal is optimized; in fact the $\chi_b(3P)$ radiative decays are expected to be similar to the $\chi_b(2P)$ radiative decays and so the adopted selection for this latter state can be considered optimal for the $\chi_b(3P)$ as well.
The cuts are applied to the following variables:

- $\sigma_{\Upsilon(1S)}$, the experimental resolution of the $\Upsilon(1S)$;
- $p_{T\gamma}$, the transverse momentum of the reconstructed photon;
- $|\eta_\gamma|$, the pseudorapidity of the reconstructed photon;
- $|\eta_{\mu\mu}|$, the rapidity of the dimuon produced in the decay $\Upsilon(1S) \to \mu^+\mu^-$;
- $|d_z|$, the projection of the direction of the photon along the axis, parallel to the beam axis, where the vertex of the $\Upsilon(1S)$ lies.

From the analysis of about seven thousand combinations of cuts, the one which maximizes the ratio R is the following:

$$\sigma_{\Upsilon(1S)<2.25\,GeV},\ p_{T\gamma}>1\,GeV,\ |\eta_\gamma|<1,\ |\eta_{\mu\mu}|<1.25,\ |d_z|<0.75. \tag{27}$$

The distribution of these variables and the relative applied cuts are shown in Appendix C. In Figure 70 is shown the fit obtained with this cuts combination.

OSERVATIONS In Figure 70 α and β are the parameters of the PDF used for the background (see Chapter 7 for more details) and N_{bkg} represents the number of background events;

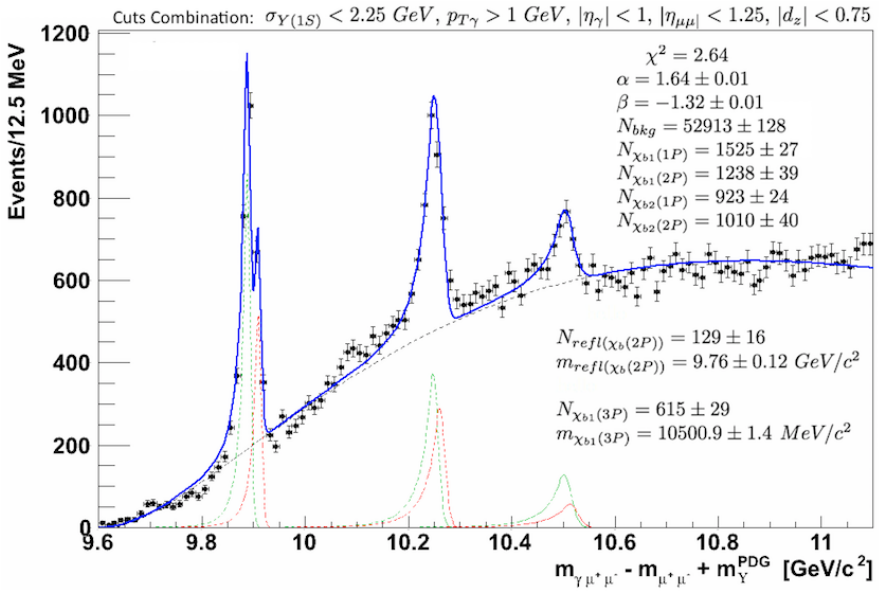

Figure 70: Y(1S) spectrum with the best cuts combination: R=21.31

the parameters $N_{\chi_{bJ}(nP)}$, with J=1,2 and n=1,2,3 express the number of signals from the relative χ_b states; $N_{refl(\chi_b(2P))}$ and $m_{refl(\chi_b(2P))}$ concern the misreconstructed Y(1S) state, that is the invariant mass of $Y(1S)\gamma_1$, obtained from the decay chain $Y(3S) \to^1 \chi_{b2}(2P)\gamma_1$, where $\chi_{b2}(2P) \to^2 Y(2S)\gamma_2$ and $Y(2S) \to^3 Y(1S)\pi^0\pi^0$, where the pions are not reconstructed. $m_{\chi_{b1}(3P)}$ is the mass of the $\chi_{b1}(3P)$ state.

Searching the cuts combinations which maximize the ratio R interesting spectrum are observed: they present an excess around 10.08 GeV.

An interesting observation is the presence of what seems an excess around a value of 10.08 GeV, so it was object of investigation. The first step about it was the research of this excess in the fits with other cuts combinations, starting from the ones obtained with combinations which allow a large value of R. The following plots report some examples.

8.1 EXAMPLES OF OBSERVATIONS OF THE EXCESS IN THE Y(1S) SPECTRUM

In order to understand if the observed excess is a statistical fluctuation, a study of its behaviour when changing the cuts is needed. Results and considerations about this study are reported through the following examples of $Y(1S)\gamma$ spectra with different cuts combinations.

Examples about the observed excess.

OBSERVATIONS In Figure 72 the values of $p_{T\gamma}$ and $|\eta_{\mu\mu}|$ are the same as in the Figure 70, but the excess is suppresed; $\sigma_{Y(S)}$ is a little different, while $|\eta_\gamma|$ went from 1.0 to 0.85, as in the ex-

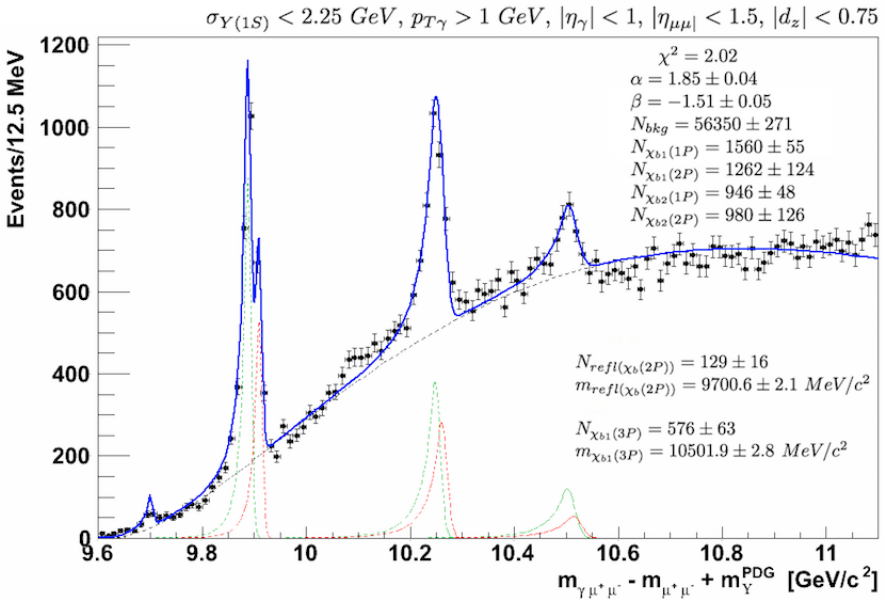

Figure 71: Υ(1S) spectrum: example with cuts combinations (R=20.92).

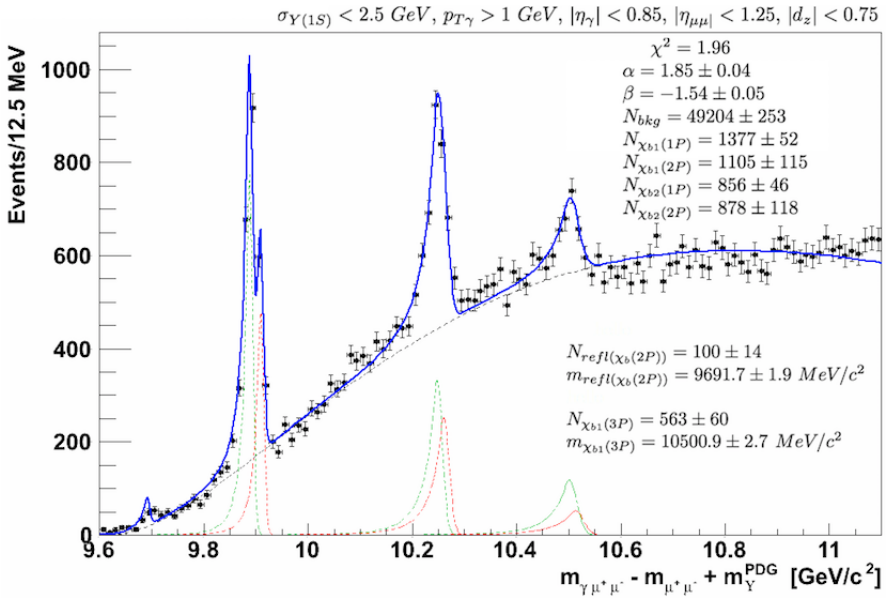

Figure 72: Υ(1S) spectrum: example with cuts combinations (R=19.79).

ample in Figure 73, where also d_z changes. In Figure 74 the cuts are the same as in Figure 73, except for the value of the variable $p_{T\gamma}$. With the cuts combinations in Figure 70, Figure 71 and Figure 75 the excess around 10.08 GeV is clearly visible. A summary of these examples is shown schematically in Figure 76.

Strategy: search for the observed excess in simulated decay chains.

From this table one can deduce that apparently there isn't a particular variable or a couple of variables which influences the comparison of the excess significantly. The hypothesis that this

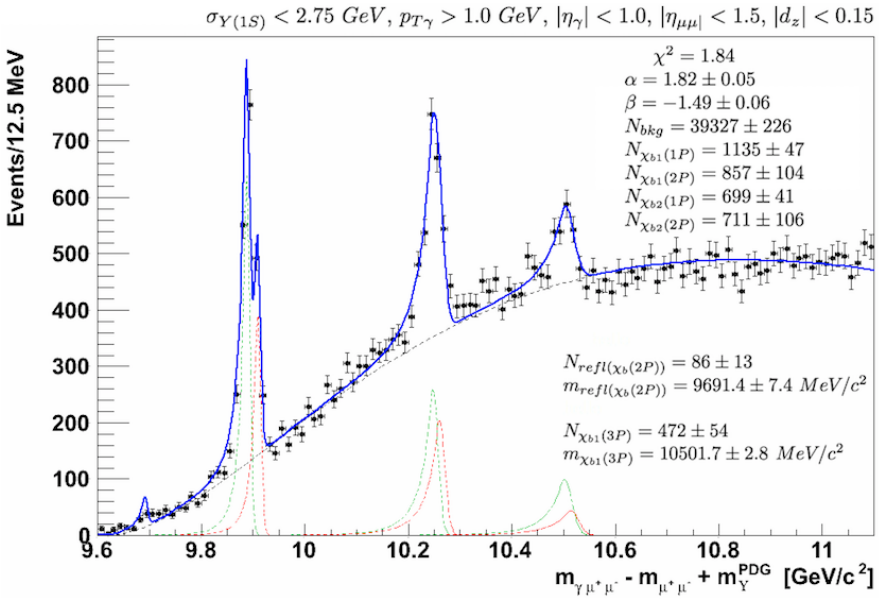

Figure 73: Y(1S) spectrum: example with cuts combinations (R=17.6).

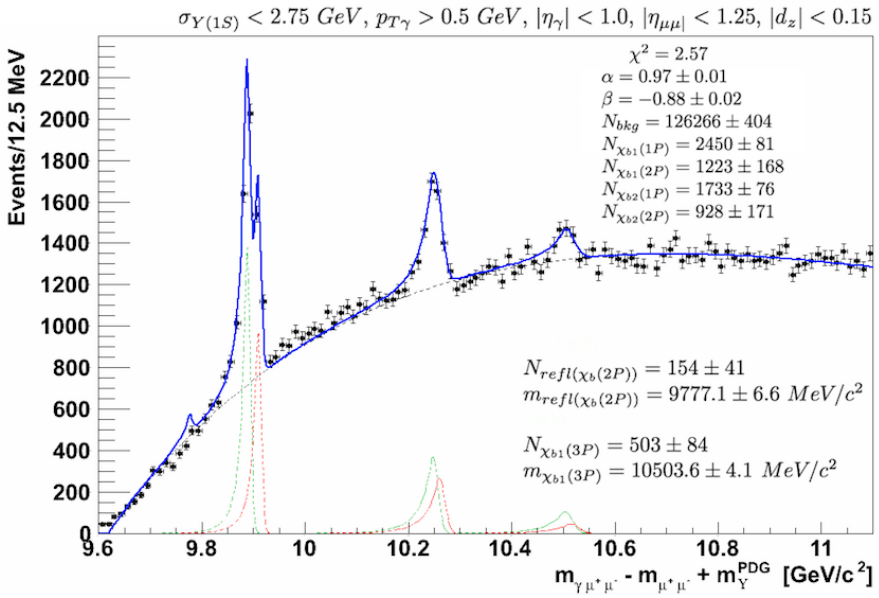

Figure 74: Y(1S) spectrum: example with cuts combinations (R=13.73).

excess can be due to misreconstructed radiative transitions was proposed; an example of these misreconstructions can be the $\Upsilon(1S)\gamma_1$ reconstruction from the decay chain $\Upsilon(3S) \to^1 \chi_{b2}(1P)\gamma_1$, where $\chi_{b2}(1P) \to^2 \Upsilon(1S)\gamma_2$.
So the next step is describing the reasearch for the excess simulating the decay chains of the χ_b states.

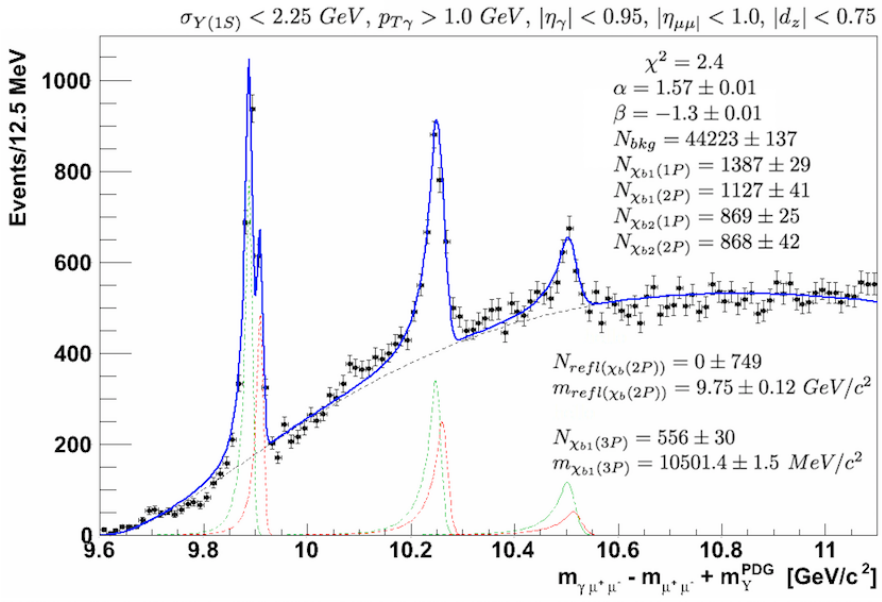

Figure 75: Υ(1S) spectrum: example with cuts combinations (R=20.39).

$\sigma_{\Upsilon(1S)}$	< 2.25	< 2.25	< 2.5	< 2.75	< 2.75	< 2.25
$p_{t\gamma}$	> 1	> 1	> 1	> 1	> 0.5	> 1
$\lvert\eta_\gamma\rvert$	< 1	< 1	< 0.85	< 1	< 1	< 0.95
$\lvert\eta_{\mu\mu}\rvert$	< 1.25	< 1.5	< 1.25	< 1.5	< 1.25	< 1
dz	< 0.75	< 0.75	< 0.75	< 0.15	< 0.15	< 0.75
Excess 10.08 MeV	✓	✓	✗	✗	✗	✓

Figure 76: Summary of the examples concerning the observation of the excess in the Υ(1S) spectrum.

8.2 DECAY CHAINS INVESTIGATION

In Table 3 are reported the just mentioned decay chains which are suspected to be the origin of the excess around 10.08 GeV; they were simulated using the Root class *TGenPhaseSpace*. The height of the excess will depend on the Branching Ratio (BR) of these chains, also reported in Table 3.
From these decay chains we expect that the $\Upsilon\gamma$ spectrum could show features around 9.9 GeV, 9.25 GeV, 9.75 GeV, due either to a sequential radiative decays where one of the photons is lost and the wrong photon is associated to the Υ, or to a $\Upsilon\pi\pi$ decay where the pions are not reconstructed.
The found expected peaks are highlighted in Figure 77, which represents a first attempt to fit the observed excess. The result of this research is that the observed new excess doesn't find its origin in any of these decay processes.

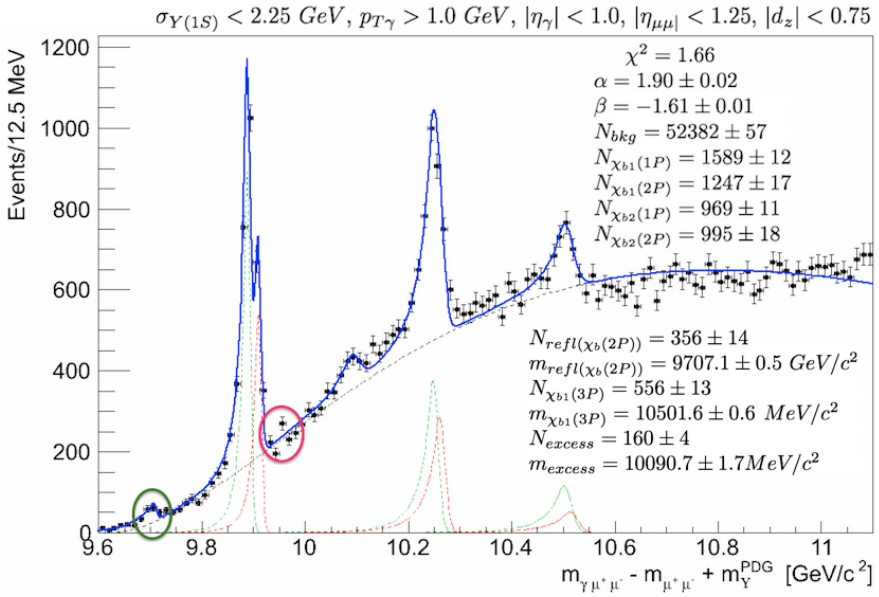

Figure 77: First attempt to fit the Y(1S) spectrum with the excess included.

In Figure 77 the variables N_{excess} and m_{excess} are the number of events from the excess and its mass, repesctively. The coloured circled peaks concerns the misreconstructions, whose simulation is reported in Table 3. The cuts combination used for this fit and for the next fits is the one which maximizes the ratio R, that is the combination reported in Figure 70.
A new fit of the invariant mass spectrum of the Y(1S) is shown in Figure 78: the background is interpolated with a polinomial function, modeled such as a RooChebychev with five parameters. Considering the numbers of signals of the excess and the

DECAY CHAINS	EXP. PEAK (GEV)	BR DECAYS
1. $\Upsilon(3S) \to^1 \chi_{b2}(1P)\gamma_1$,	$\Upsilon(1S)\gamma_1 = 9.91$	$^1(9.9 \pm 1.3)10^{-3}$
where $\chi_{b2}(1P) \to^2 \Upsilon(1S)\gamma_2$		$^2 19.1 \pm 1.2$
2. $\Upsilon(3S) \to^1 \chi_{b1}(1P)\gamma_1$,	$\Upsilon(1S)\gamma_1 = 9.92$	$^1(9 \pm 5)10^{-4}$
where $\chi_{b1}(1P) \to^2 \Upsilon(1S)\gamma_2$		$^2 33.9 \pm 2.2$
3. $\Upsilon(3S) \to^1 \chi_{b0}(1P)\gamma_1$,	$\Upsilon(1S)\gamma_1 = 9.96$	$^1(2.7 \pm 0.4)10^{-3}$
where $\chi_{b0}(1P) \to^2 \Upsilon(1S)\gamma_2$		$^2 1.76 \pm 0.35$
4. $\Upsilon(3S) \to^1 \chi_{b2}(2P)\gamma_1$,	$\Upsilon(1S)\gamma_2 = 10.27$	$^1 13.1 \pm 1.6$
where $\chi_{b2}(2P) \to^2 \Upsilon(1S)\gamma_2$		$^2 7.0 \pm 0.7$
5. $\Upsilon(3S) \to^1 \chi_{b1}(2P)\gamma_1$,	$\Upsilon(1S)\gamma_2 = 10.26$	$^1 5.9 \pm 0.6$
where $\chi_{b1}(2P) \to^2 \Upsilon(1S)\gamma_2$		$^2 9.2 \pm 0.8$
6. $\Upsilon(3S) \to^1 \chi_{b0}(2P)\gamma_1$,	$\Upsilon(1S)\gamma_2 = 10.23$	$^1 12.6 \pm 1.2$
where $\chi_{b0}(2P) \to^2 \Upsilon(1S)\gamma_2$		$^2 (9 \pm 6)\text{x}10^{-3}$
7. $\Upsilon(3S) \to^1 \chi_{b2}(2P)\gamma_1$,	$\Upsilon(1S)\gamma_2 = 9.71$	$^1 13.1 \pm 1.6$
where $\chi_{b2}(2P) \to^2 \Upsilon(2S)\gamma_2$,		$^2 10.6 \pm 2.6$
and $\Upsilon(2S) \to^3 \Upsilon(1S)\pi^+\pi^-$		$^3 17.9 \pm 0.3$
8. $\Upsilon(3S) \to^1 \chi_{b2}(2P)\gamma_1$,	$\Upsilon(1S)\gamma_2 = 9.71$	$^1 13.1 \pm 1.6$
where $\chi_{b2}(2P) \to^2 \Upsilon(2S)\gamma_2$,		$^2 10.6 \pm 2.6$
and $\Upsilon(2S) \to^3 \Upsilon(1S)\pi^0\pi^0$		$^3 8.6 \pm 0.4$
9. $\Upsilon(3S) \to^1 \chi_{b2}(2P)\gamma_1$,	$\Upsilon(1S)\gamma_2 = 9.71$	$^1 13.1 \pm 1.6$
where $\chi_{b2}(2P) \to^2 \Upsilon(2S)\gamma_2$		$^2 10.6 \pm 2.6$
and $\Upsilon(2S) \to^3 \Upsilon(1S)\pi^0$		$^3 < 1.8 \pm 10^{-4}$

Table 3: Simulated decay chains to search for the excess in the Υ(1S) spectrum.

relative background a first estimation of its significance can be founded:

$$(S/B)\sqrt{events} = 3.7\ \sigma. \tag{28}$$

8.3 Υ(2S) SPECTRUM

The same procedure on the cuts combinations was done for the Υ(2S) spectrum. The cuts combination that maximizes the ratio R is:

$$\sigma_{\Upsilon(1S)<2.5GeV,\ p_{T\gamma}>0.75GeV,\ |\eta_\gamma|<0.95,\ |\eta_{\mu\mu}|<1.0,\ |d_z|<0.496.} \tag{29}$$

The fit obtained using this combination is reported in Figure 79.

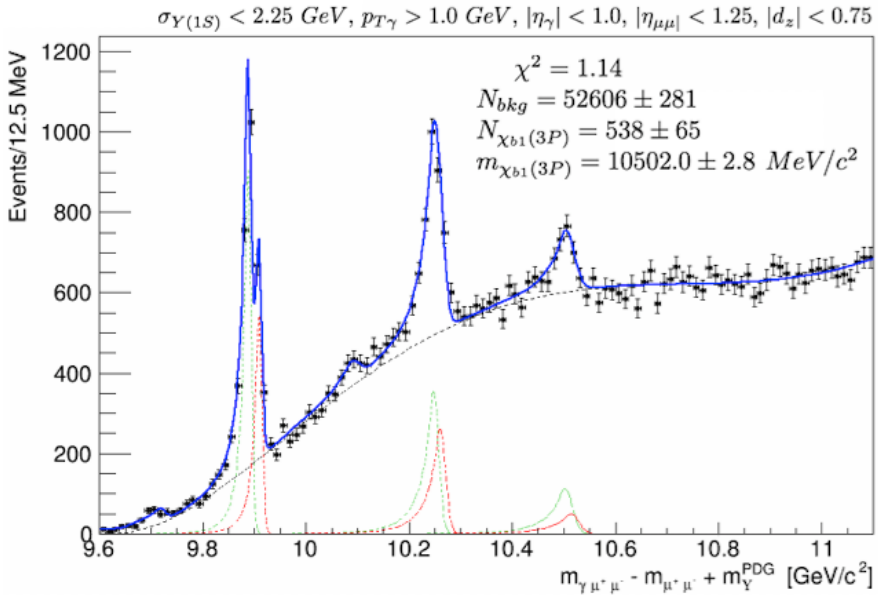

Figure 78: New fit to the Υ(1S) spectrum with the excess included.

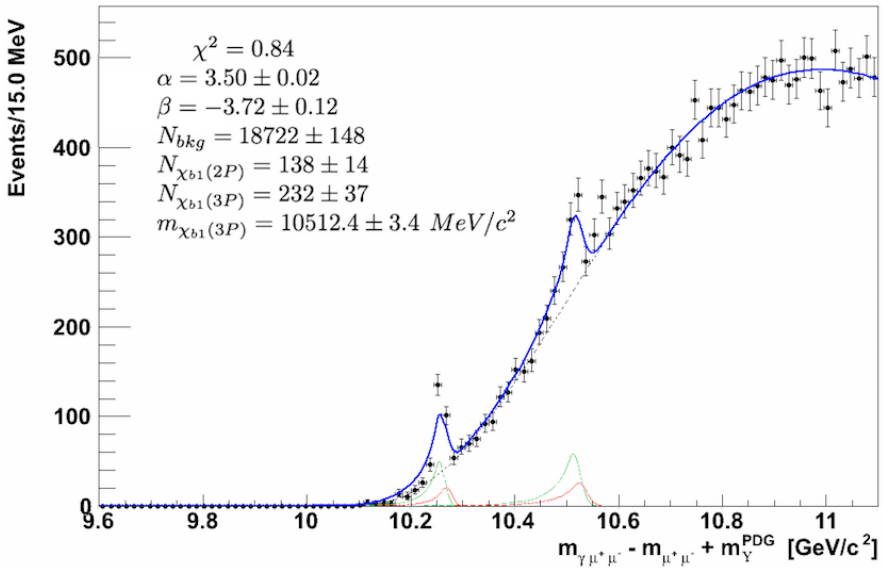

Figure 79: Fit to the Υ(2S) spectrum obtained using the best cuts combination (R=6.17).

To increase the sensitivity in order to view most clearly as possible the presence of the excess observed in the Υ(1S) spectrum also in the Υ(2S) spectrum, the fit of the latter one is made without the cut on the $p_{T\gamma}$. In the matter of this strategy the Figure 80 shows the result, with particular attention to the region of interest, around 10.08 GeV.

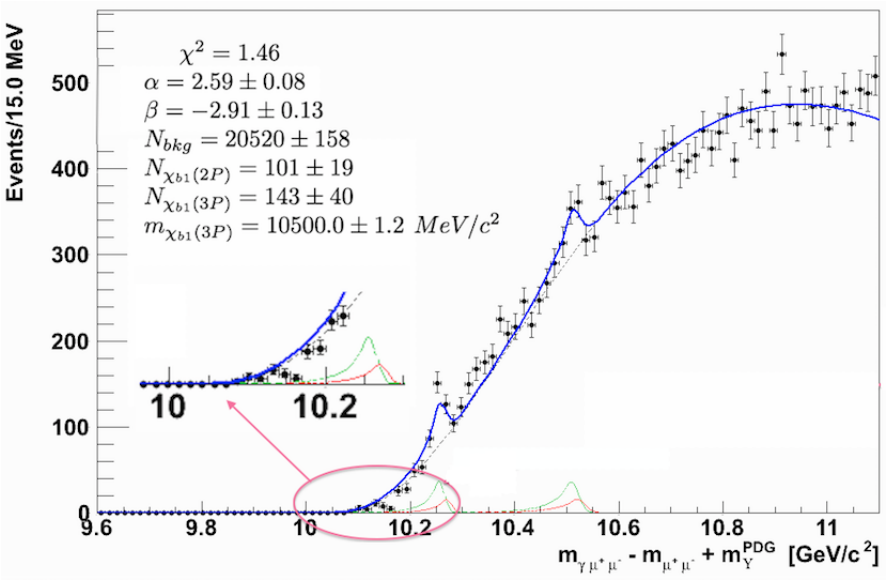

Figure 80: Fit to the Υ(2S) spectrum obtained without the cut on the $p_{T\gamma}$.

This fit cannot say lot about the excess because it doesn't provide for a clear division between the background and possible signals. Indeed in that region a peak corresponding to the invariant mass of $\Upsilon(2S)\gamma_1$ is espected, considering the decay chain $\Upsilon(3S) \rightarrow \chi_{b2}(2P)\gamma_1$, where $\chi_{b2}(2P) \rightarrow \Upsilon(2S)\gamma_2$ and $\Upsilon(2S)\gamma_1 = 10.11$ GeV.

OBSERVATIONS While the excess is still object of investigation, the study of the best cuts combinations for the Υ(1S) and Υ(2S) spectrum was functional to the optimization of the fits and so allows to perform with great precision the simultaneous fit to Υ(1S) and Υ2S) in order to estimate the mass of the $\chi_b(3P)$, as described in the next chapter.

9

DETERMINATION OF THE MASS OF THE $\chi_b(3P)$

The least chapters described the studies of the $\Upsilon(1S)\gamma$ and $\Upsilon(2S)\gamma$ invariant mass spectra and of the signal response expected for the $\chi_b(3P)$ radiative decays. Since in the $\Upsilon(2S)\gamma$ channel the mass resolution is better, as demonstrated with a Monte Carlo simulation whose details are reported in Chapter 7, the most precise measurement of the mass of the $\chi_b(3P)$ is expected to be obtained in this channel. However the statistical uncertainty is smaller in the $\Upsilon(1S)\gamma$ channel. A simultaneous fit to Y(1S) and Y(2S) can exploit the benefits of the superior resolution in the $\Upsilon(2S)\gamma$ channel combined with the smaller statistical uncertainty in the$\Upsilon(1S)\gamma$ channel. The result of the simultaneous fit is reported in Figure 81.

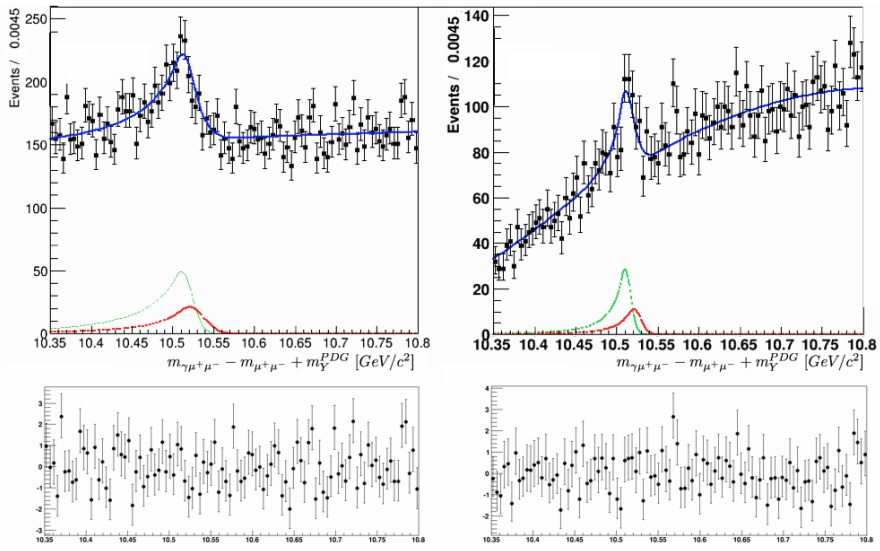

Figure 81: Simultaneous fit to the Y(1S) (on the left) and Y(2S) (on the right) spectrum. $\chi^2 = 0.97$. Pulls distributions on the bottom.

From the simultaneous fit the mass of the $\chi_b(3P)$ ris:

$$m_{\chi_b(3P)} = 10510.3 \pm 1.5\ MeV/c^2(stat.). \tag{30}$$

On this value a correction called Photon Energy Scale must be applied.

THE PHOTON ENERGY SCALE The invariant mass of the Y(1S) is obtained summing the mass of the Y(1S) from the PDG to the *Q-value*, firstly introduced in Chapter 7. It is defined as:

$$Q = m_{\gamma\mu^+\mu^-} - m_{\mu^+\mu^-}. \tag{31}$$

The Q-value doesn't depend on the estimation of the dimuon invariant mass, but its accuracy and precision depend on the calibration and resolution of the converted photon momentum measurement. A fraction of the energy of the photon is lost because the electron and the positron deriving from the photon conversion in the tracker lose energy which can't be recovered; indeed their trajectories are influenced by brehmsstrahlung and multiple scattering inside the CMS tracker material and curved because of the syncrotron radiation due to the strong magnetic field.
One method to estimate the PES is then to evaluate the Q-value of reconstructed Monte Carlo signals used and divide that Q-value by the *real* Q-value of the same states as read from PDG.
The PES can also be evaluated measuring the Q-value of four different states, χ_{c1}, χ_{c2}, $\chi_b(1P)$ and $\chi_b(2P)$, and then dividing it by the corresponding Q-value obtained from PDG tables.
The PES was evaluated in another analysis conduced in the CMS Torino Group; once its value (f_{PES}) is obtained the mass of the $\chi_b(3P)$ can be calculated with the following formula:

$$M_{\chi_b(3P)} = Q_{\chi_b(3P)}/f_{PES} + M^{PDG}_{Y(1S)}. \tag{32}$$

The fit obtained appliyng the PES correction is shown in Figure 82. The measured value of the mass of the $\chi_b(3P)$ with the PES correction is:

$$m_{\chi_b(3P)} = 10518.7 \pm 1.6\ MeV/c^2(stat.). \tag{33}$$

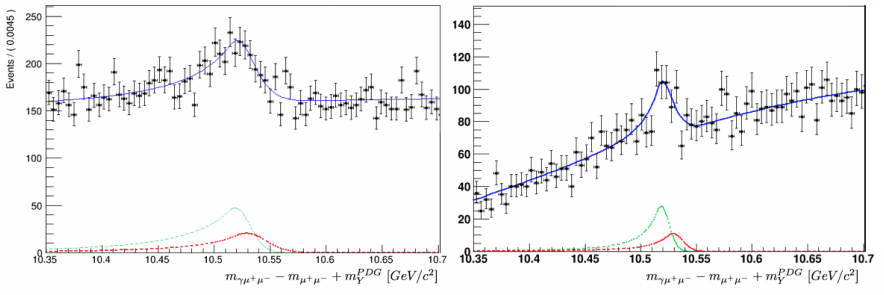

Figure 82: Simultaneous fit to the Y(1S) (on the left) and Y(2S) (on the right) spectrum with PES correction. $\chi^2 = 0.97$.

10

CONCLUSIONS

The presented double analysis was a test of the performance of the CMS detector and also offers an experimental way to confirm and eventually extend the actual knownledge concerning the bottomonium spectrum.
In particular the noise in ECAL and the first results for thresholds for the $\phi - symmetry$ calibration method were provided.
Through the study of the bottomonium spectrum a new and precise measurement of the mass of the $\chi_b(3P)$ was obtained. Indeed a new excess of invariant mass around 10.08 GeV was observed: it still be object of investigation.

Part V

APPENDIX

A

THE CMS DETECTOR

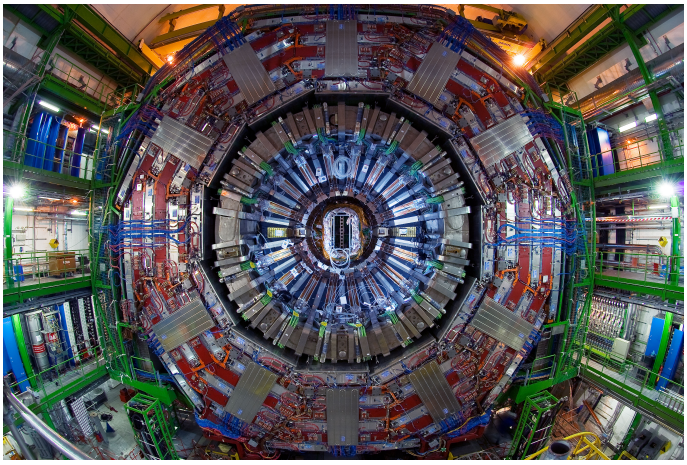

Figure 83: A view of CMS detector.

Figure 84: One of the CMS Tracker End Caps.

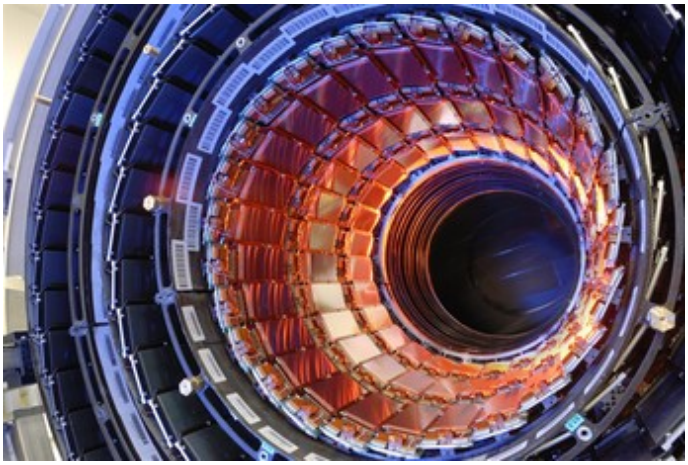

Figure 85: Part of the CMS Tracker Inner Barrel.

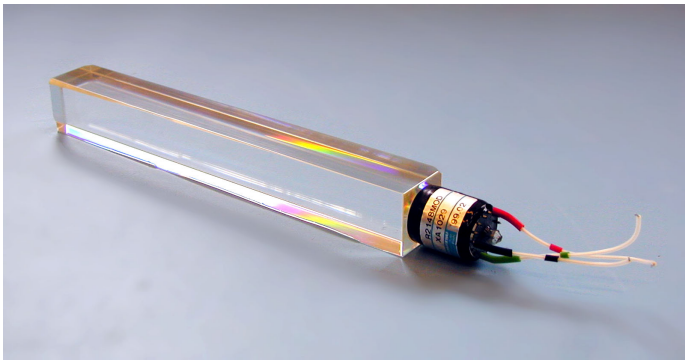

Figure 86: A Crystal of CMS ECAL; its direct connection to the VPT can be observed.

B

CMS ECAL NOISE COMPLETE ANALYSIS

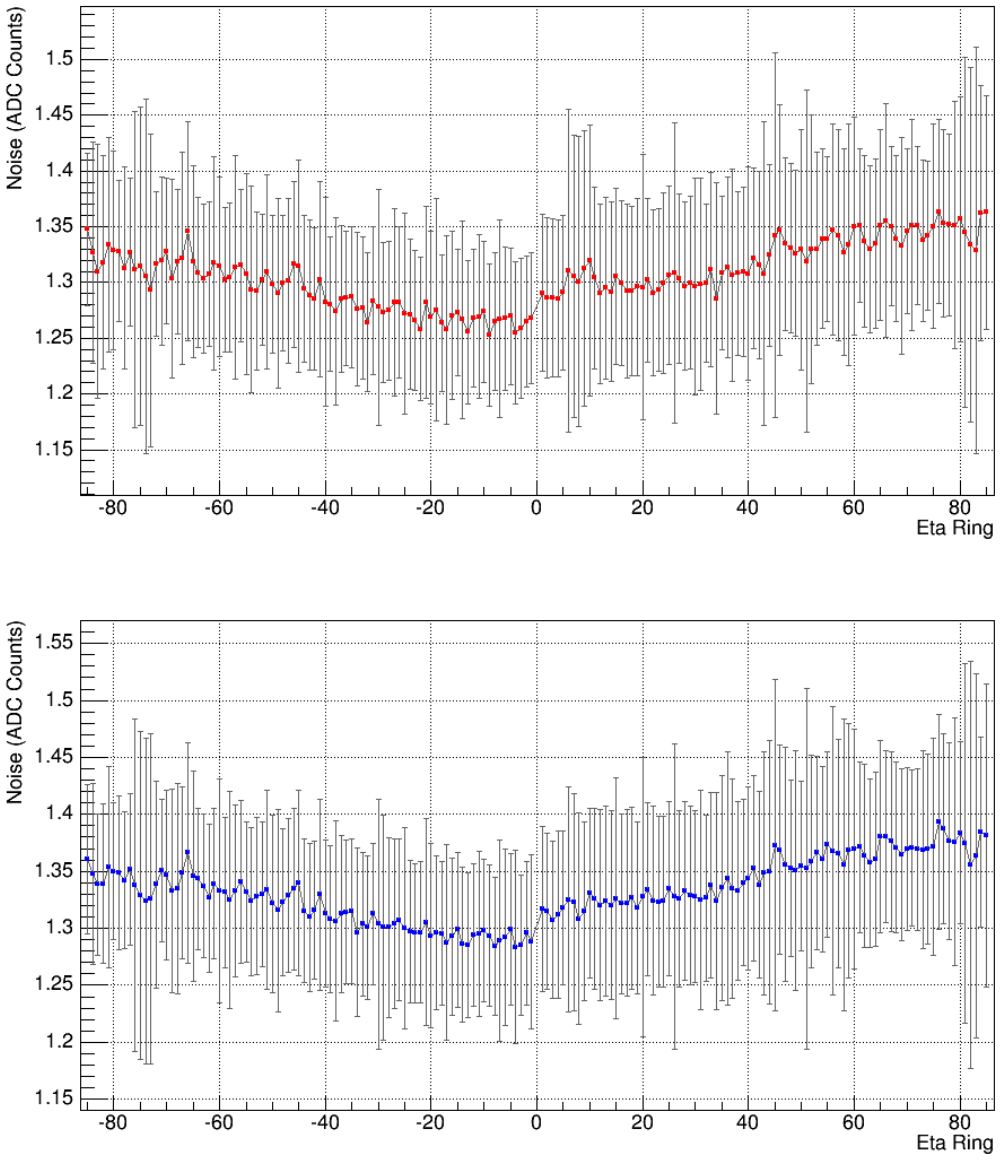

Figure 87: EB Noise in ADC Counts, Run A (top) and Run B (bottom).

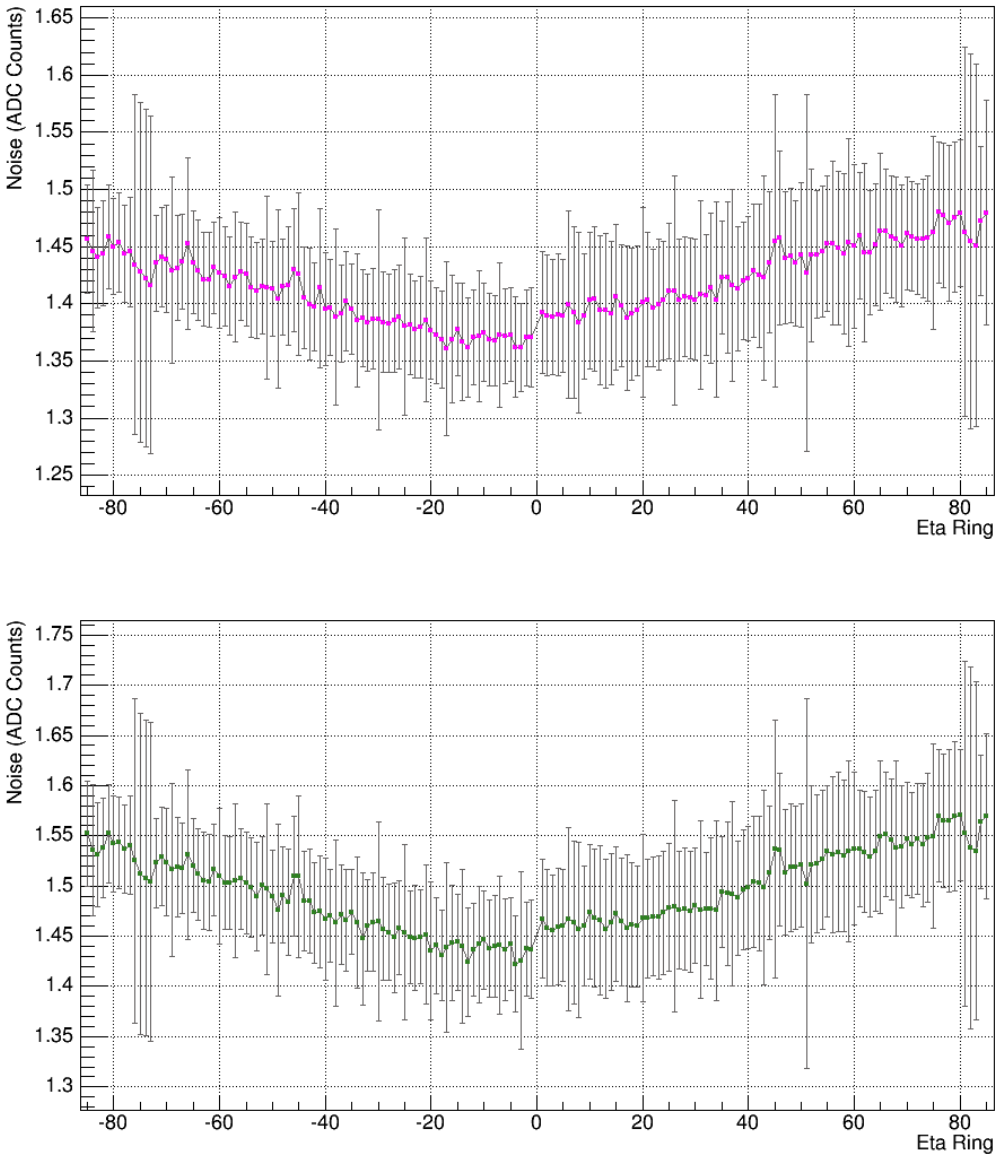

Figure 88: EB Noise in ADC Counts, Run C (top) and Run D (bottom).

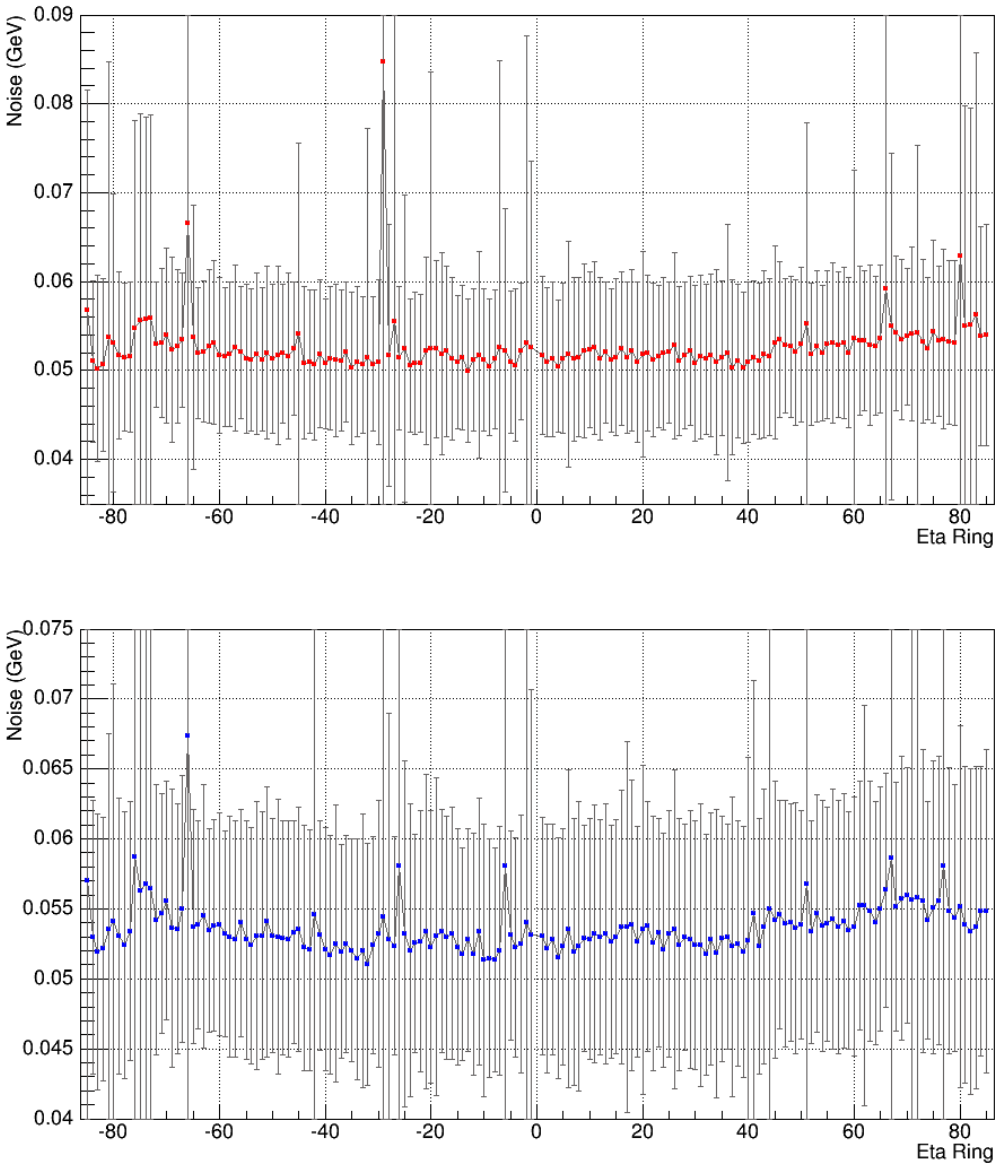

Figure 89: EB Noise in GeV, Run A (top), Run B (bottom).

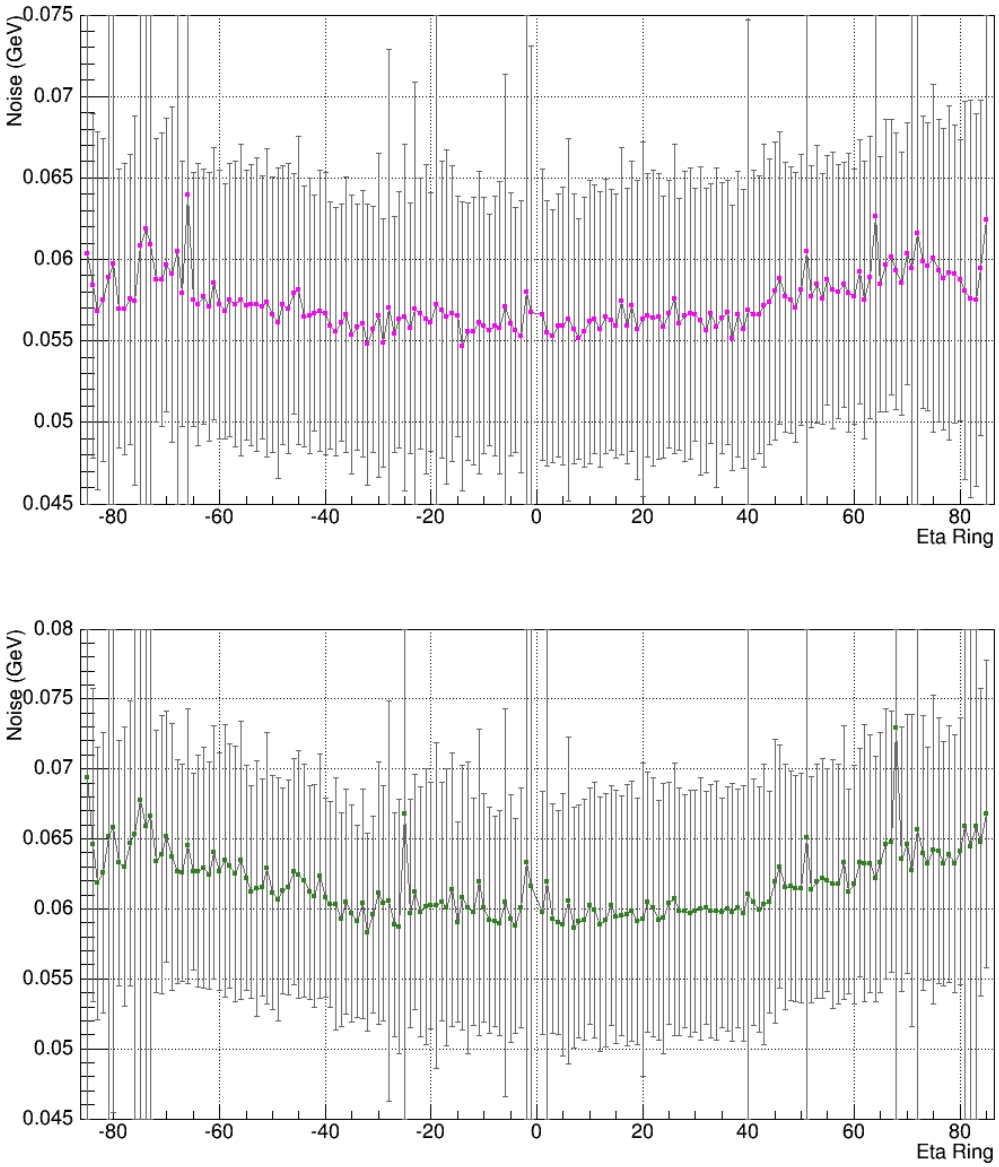

Figure 90: EB Noise in GeV, Run C (top), Run D (bottom).

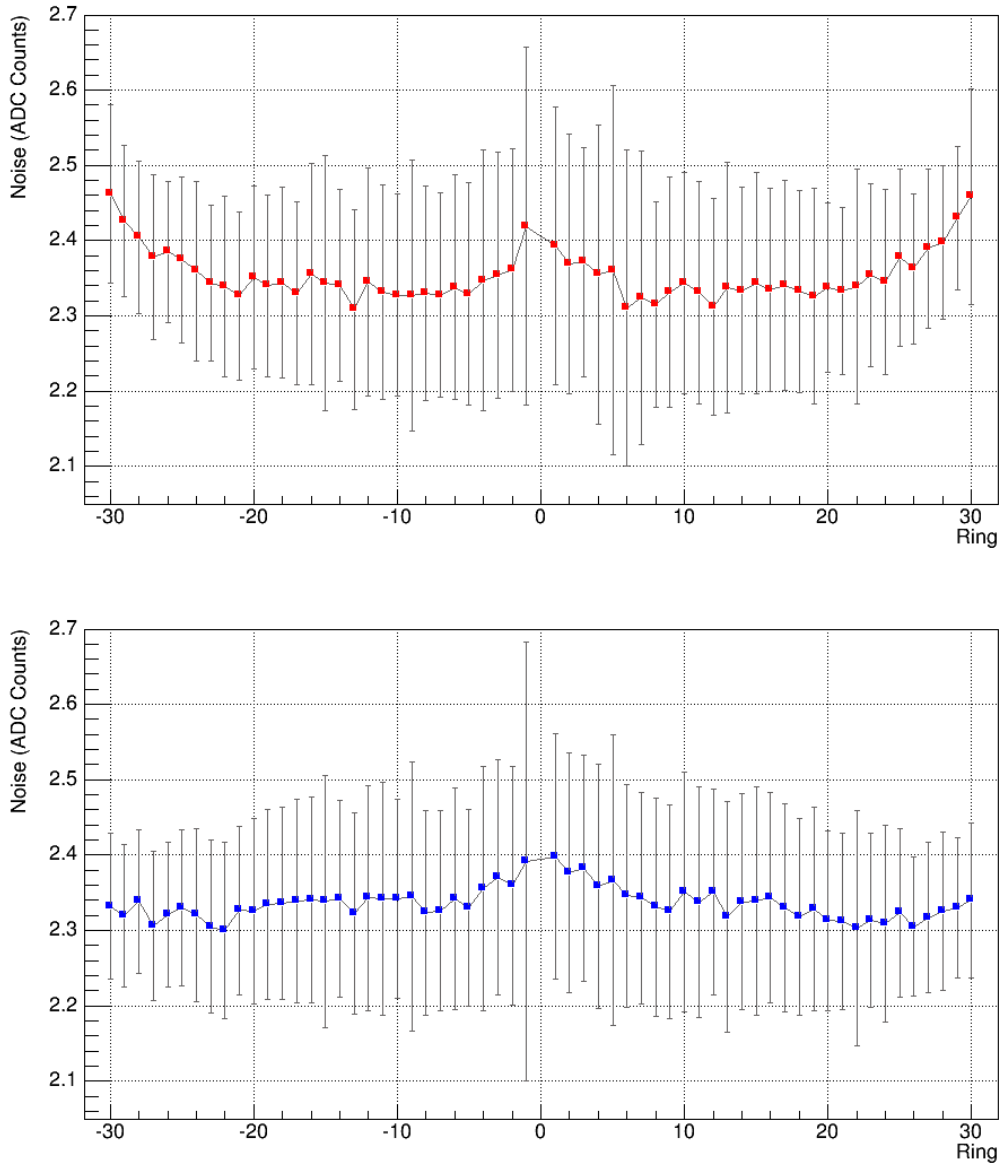

Figure 91: EE Noise in ADC Counts, Run A (top), Run B (bottom).

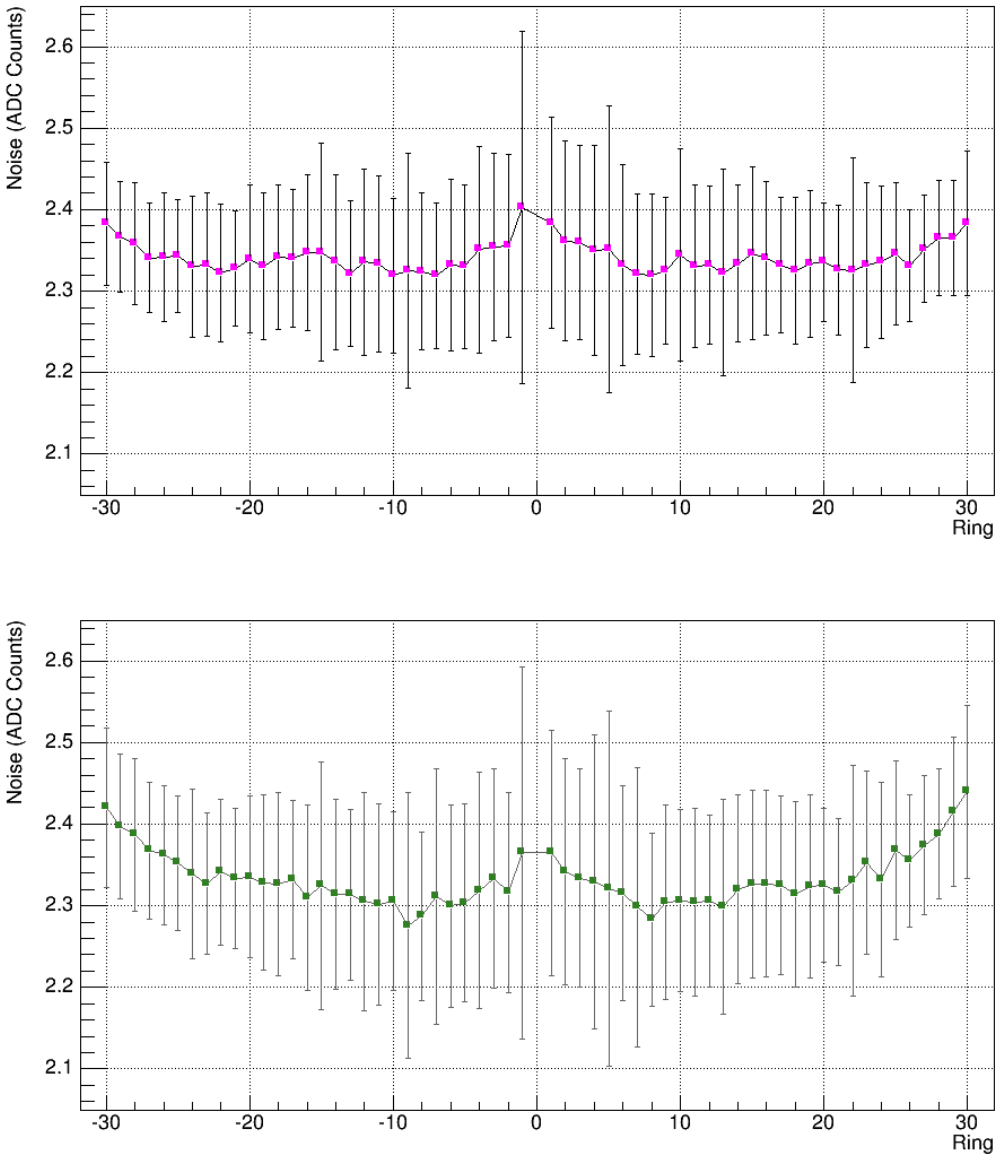

Figure 92: EE Noise in ADC Counts, Run C (top), Run D (bottom).

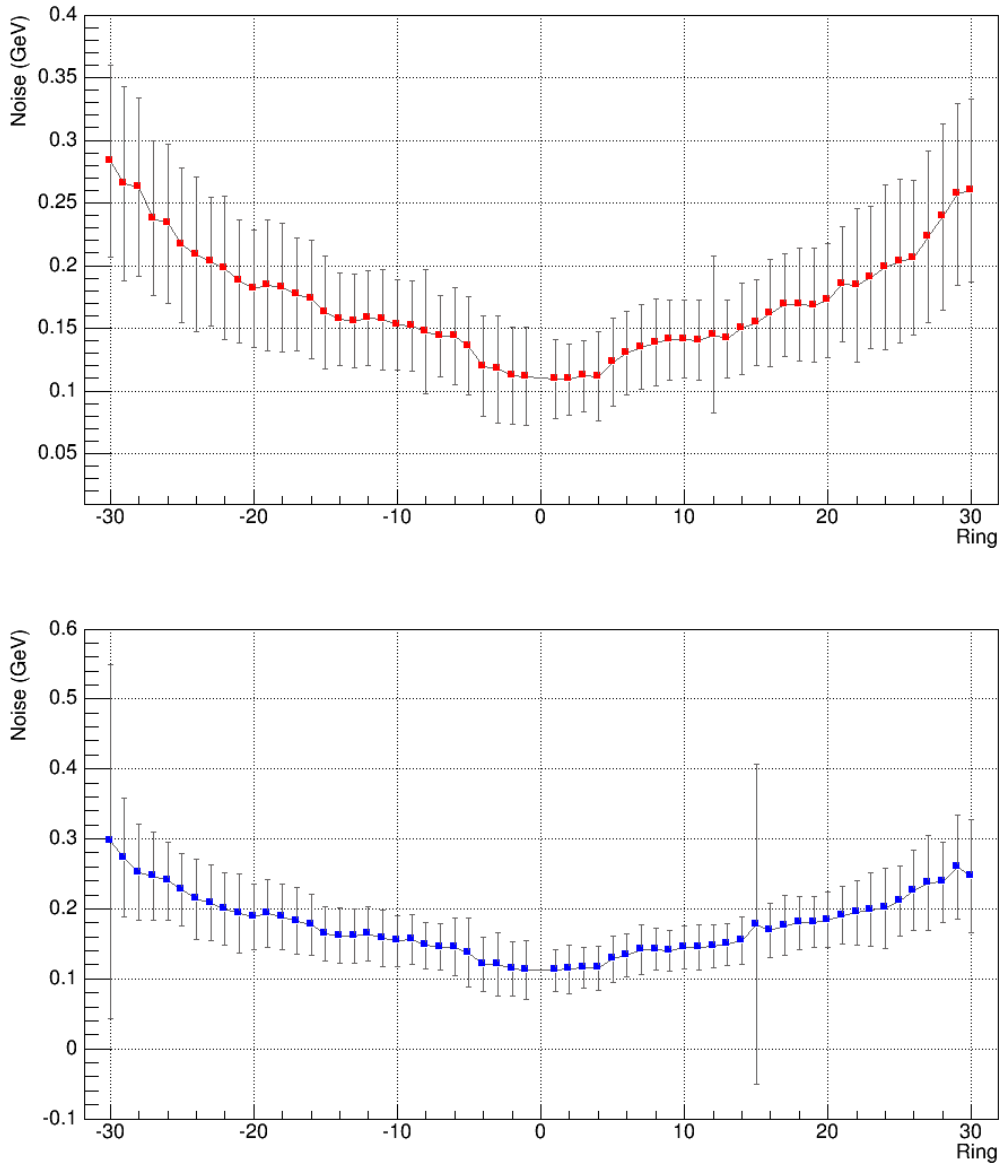

Figure 93: EE Noise in GeV, Run A (top), Run B (bottom).

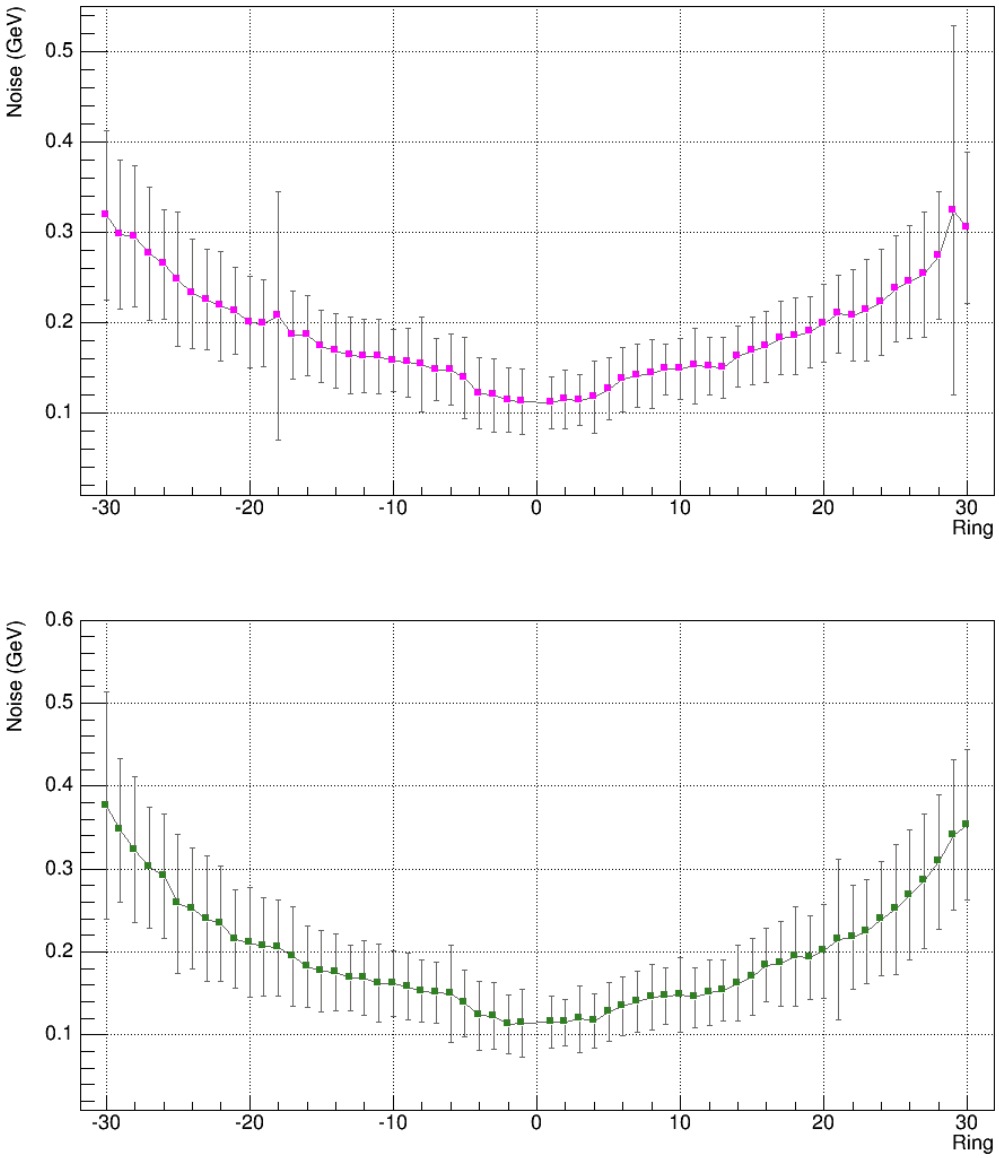

Figure 94: EE Noise in GeV, Run C (top), Run D (bottom).

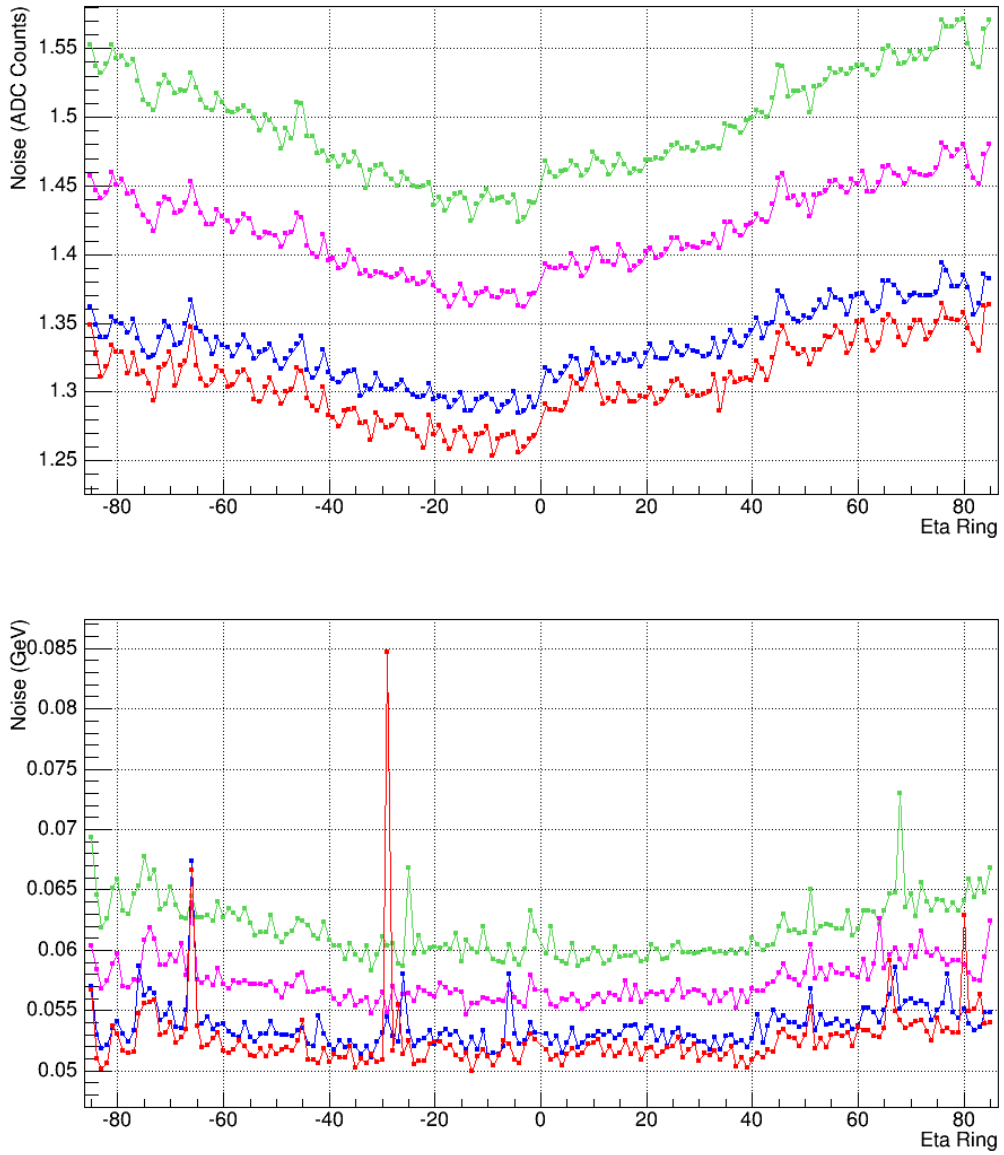

Figure 95: EB Noise in ADC Counts (top) and in GeV (bottom). *Colors Legend:* red for Run A, blue for Run B, magenta for Run C, green for Run D.

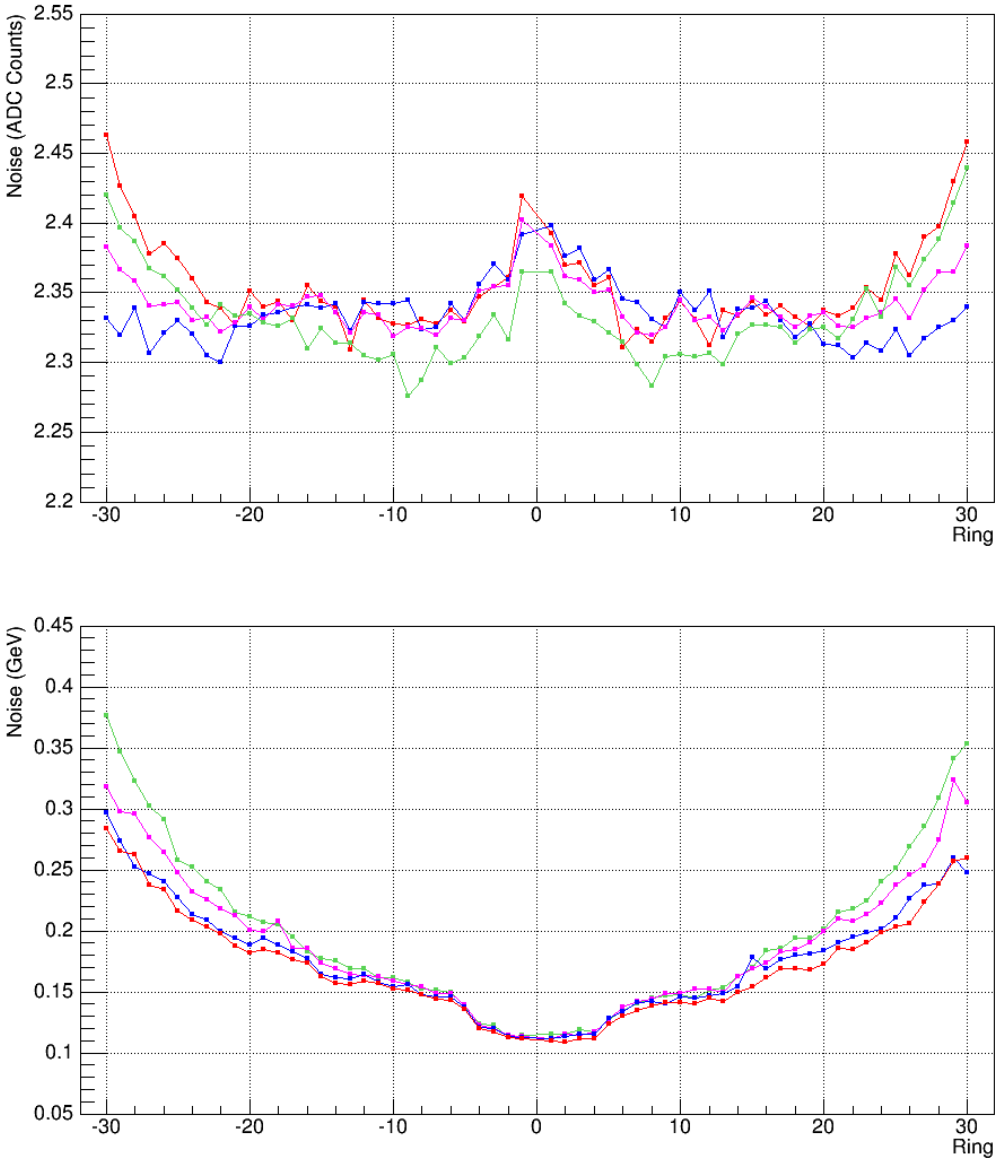

Figure 96: EE Noise in ADC Counts (top) and in GeV (bottom). *Colors Legend:* red for Run A, blue for Run B, magenta for Run C, green for Run D.

C

ANALYSIS OF THE SPECTRUM $\Upsilon(nS) + \gamma$

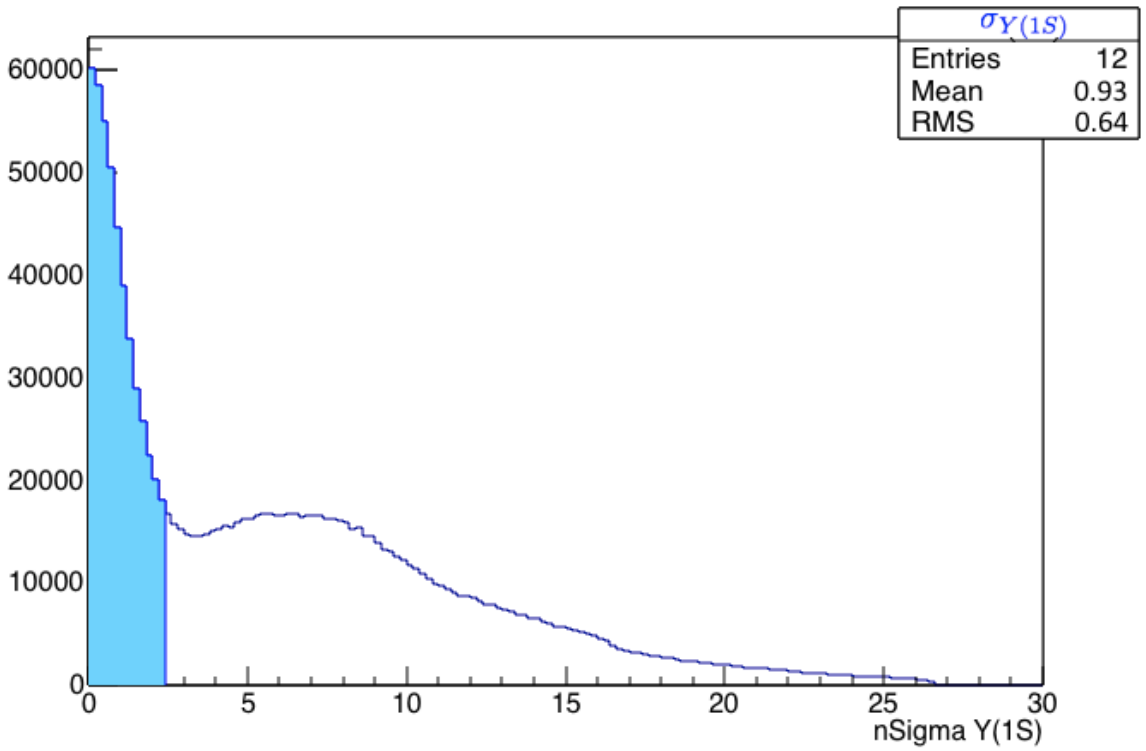

Figure 97: $\sigma_{\Upsilon(1S)}$ distribution: it is the experimental resolution of the Y(1S).

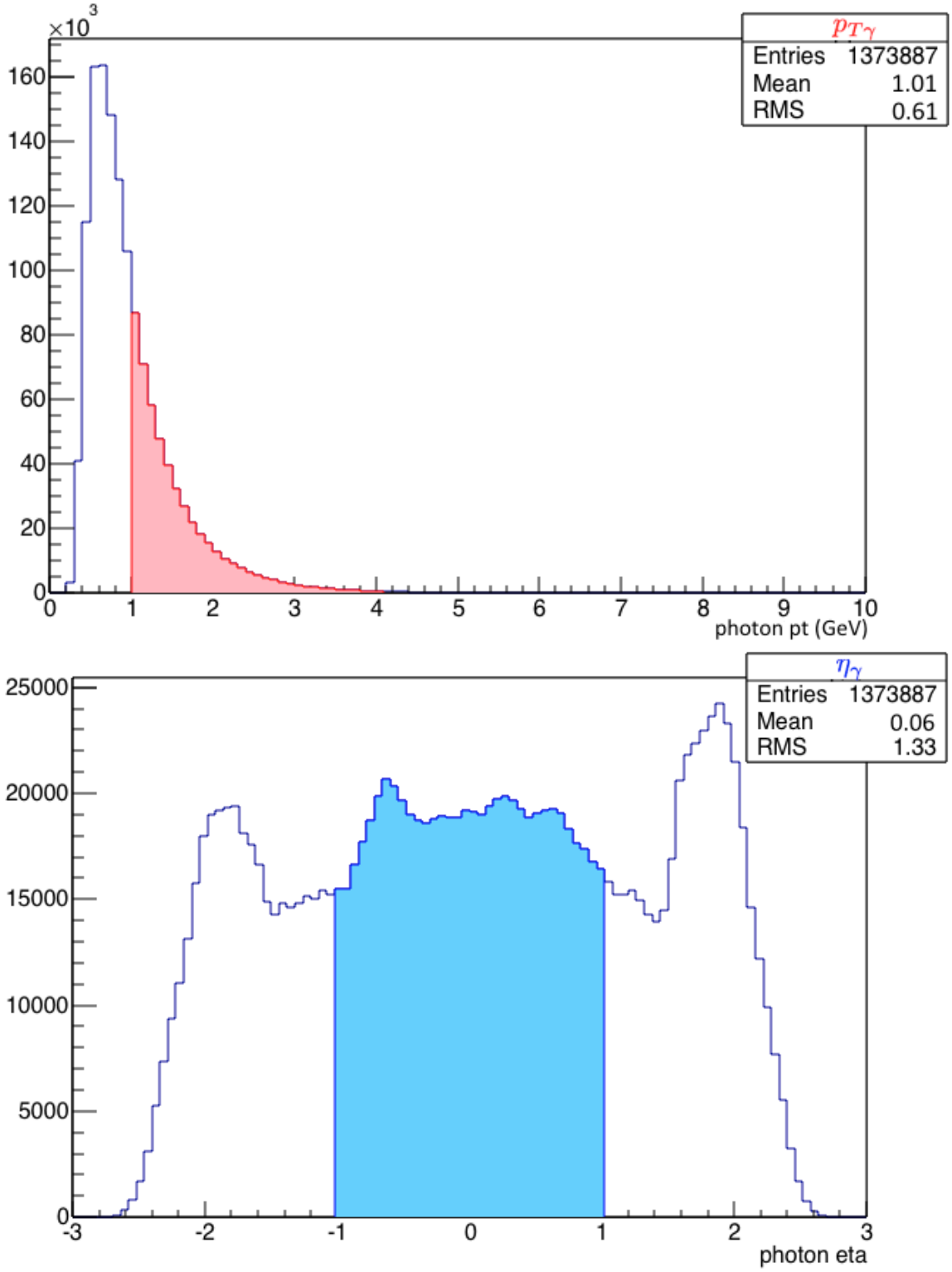

Figure 98: $p_{T\gamma}$ (top) and $|\eta_\gamma|$ (bottom) distributions. $p_{T\gamma}$ is the transverse momentum of the reconstructed photon, while $|\eta_\gamma|$ is the pseudorapidity of the reconstructed photon.

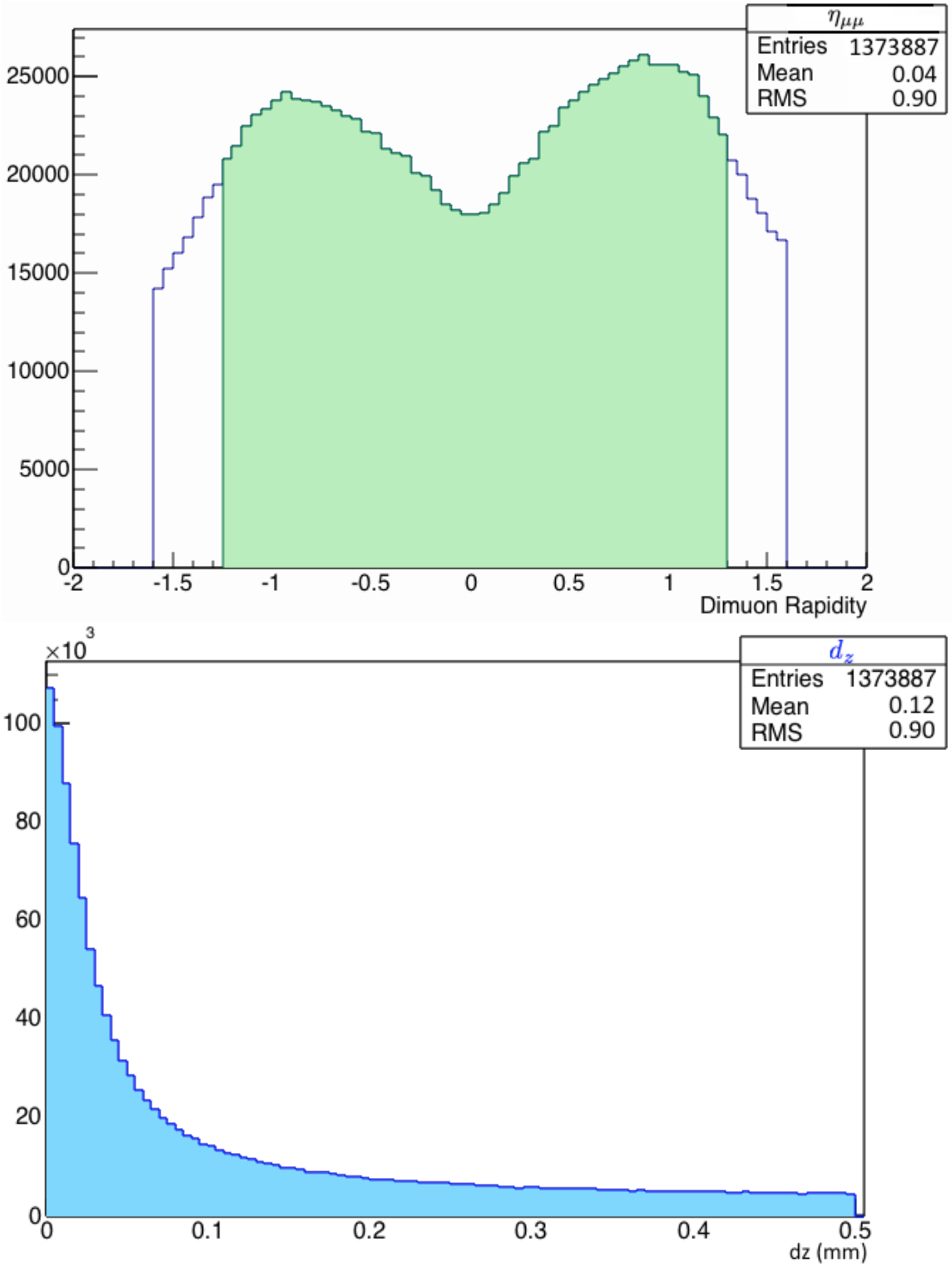

Figure 99: $|\eta_{\mu\mu}|$ (top) and $|d_z|$ (bottom) distributions. $|\eta_{\mu\mu}|$ is the rapidity of the dimuon produced in the decay $\Upsilon(1S) \to \mu^+\mu^-$
and $|d_z|$ is the projection of the direction of the photon along the axis, parallel to the beam axis, where the vertex of the $\Upsilon(1S)$ lies.

BIBLIOGRAPHY

[1] *LHC Design Report*. Report - 548 p., CERN. Geneva, 2004.

[2] *ATLAS Technical Design Report, Volume I*. The ATLAS Collaboration, CERN. Geneva, 25 May 1999.

[3] The ATLAS Collaboration. Observation of a new particle chib state in radiative transitions to Upsilon(1s) and Upsilon(2s) at ATLAS. *Phys. Rev. Lett. 108 (2012) 152001*, 21 Dec 2011.

[4] The ATLAS Collaboration. Observation of a new particle in the search for the Standard Model Higgs boson with the ATLAS detector at the LHC. *Phys.Lett. B716 (2012) 1-29*, 31 Aug 2012.

[5] The CMS Collaboration. Observation of a new boson at a mass of 125 Gev with the CMS experiment at the LHC. *Phys. Lett. B 716 (2012) 30*, 28 Jan 2013.

[6] The CMS Collaboration. CMS Luminosity, Public Results. *Available at link:* `https://twiki.cern.ch/twiki/bin/view/CMSPublic/LumiPublicResults`, Topic revision: 24 Jan 2014.

[7] The LHCb Collaboration. Measement of the chib(3p) mass and of the relative rate of chib1(1p) and chib2(2p) production. *LHCb-PAPER-2014-040*, 4 Sept 2014.

[8] Jungil Lee (Korea U.) Geoffrey T. Bodwin (Argonne), Eric Braaten (Ohio-State). Comparison of the color-evaporation model and the NRQCD factorization approach in charmonium production. *Phys.Rev. D72 (2005) 014004*, 3 Apr 2005.

[9] M. Obertino J. Blaha, N. Cartiglia. Calibration and performance test of the Very-Front-End electronics for the CMS electromagnetic calorimeter. *Author manuscript*, 2006.

DECLARATION

Torino, 8th October 2014

Federica Tarsitano